

DEVELOPMENT, CHARACTERIZATION AND DYNAMIC ANALYSIS OF METAL MATRIX COMPOSITE ROTOR

THESIS

submitted to

DELHI TECHNOLOGICAL UNIVERSITY

For the award of the degree of

DOCTOR OF PHILOSOPHY

IN

MECHANICAL ENGINEERING

By

ANUJ SHARMA

(2K16/Ph.D/ME/05)

Under the supervision of

Prof. Vikas Rastogi

(Department of Mechanical
Engineering, DTU)

Prof. Atul Kumar Agrawal

(Department of Mechanical
Engineering, DTU)



DEPARTMENT OF MECHANICAL ENGINEERING

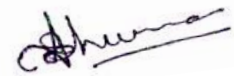
DELHI TECHNOLOGICAL UNIVERSITY

(Formerly Delhi College of Engineering)

Main Bawana Road, Shahabad Daultpur, Delhi - 110042, India

DECLARATION

I certify that the work which is being presented in this thesis entitled "**Development, Characterization and Dynamic Analysis of Metal Matrix Composite Rotor**" in the partial fulfilment of the requirement for the award of the degree of Doctorate in Philosophy submitted in the Department of Mechanical Engineering at Delhi Technological University, is an authentic record of my own work carried out during a period from August 2016 to May 2021, under the supervision of **Prof. Vikas Rastogi** and **Prof. Atul Kumar Agrawal**, Department of Mechanical Engineering, Delhi Technological University, Delhi. The matter presented in this thesis has not been submitted to any other University/Institute for the award of any degree or diploma.



(ANUJ SHARMA)

Roll No: 2K16/Ph.D/ME/05

Department of Mechanical Engineering

Delhi Technological University, Delhi

Date: 21-06-2021

Place: New Delhi

CERTIFICATE

This is to certify that the thesis entitled "**Development, Characterization and Dynamic Analysis of Metal Matrix Composite Rotor**" submitted to the Delhi Technological University, Delhi -110042, is the fulfilment of the requirements for the award of the degree of Doctorate in Philosophy in Mechanical Engineering embodies the original research work carried out by **Mr. ANUJ SHARMA**, Enrollment No: 2K16/Ph.D/ME/05 under our supervision. This work has not been submitted in part or full for any other degree or diploma of this or any other University.



21-06-2021

PROF. VIKAS RASTOGI

Department of Mechanical Engineering
Delhi Technological University, Delhi.



PROF. ATUL KUMAR AGRAWAL

Department of Mechanical Engineering
Delhi Technological University, Delhi.

*Dedicated to the
almighty and my family*

ACKNOWLEDGEMENT

I am greatly indebted to my supervisors **Prof. Vikas Rastogi** and **Prof. Atul Kumar Agrawal**, Department of Mechanical Engineering, Delhi Technological University, Delhi, for their invaluable guidance, constant inspiration, numerous suggestions and continued support throughout this research work. I am profoundly grateful to them with reverence for helping me with the necessary information and equipment & materials.

I would like to express my sincere gratitude to **Prof. R.S. Mishra**, Chairman, DRC, Mechanical Engineering Department, **Prof. S.K. Garg**, Head, Mechanical Engineering Department, **Prof. Vipin**, Former Head, Mechanical Engineering Department, Delhi Technological University, for their valuable help, motivation and extending all the necessary processing and experimental facilities during my research work. I am very thankful to **Prof. Mohammed Suhaib**, **Dr. Ajit Kumar Jha**, **Dr. R.S. Walia** and **Dr. Mukhtiar Singh** for being members of my SRC committee.

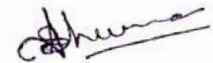
I would like to thank my fellow lab mates Dr. Ashish Gupta, Dr. Nagendra Maurya, Yamika, Abdul, Aakash, Saatvik, Mehak, Pooja, Dr. Anuj Jain, for helping and encouraging me throughout my research. A special thanks to my friend Deepak who enlightened me with a different approach to tackling the process of publication when I was exhausted and stuck.

I would like to thank Mr. Narendra Bisht for helping me during lab engagements, Mr. Tek Chand to assist me in optical microscopy, Yashwant for helping me during thesis writing. I would also like to show my gratitude towards Mr. Suraj, Abhishek, and Dhimant to support me during the thesis writing process.

I am greatly indebted to my parents for their love and blessings to see me scaling greater heights of life. Without their motivation and encouragement, the pursuit of this PhD work would have never been possible.

With immense pleasure and delight, I would like to thank my wife Satyamvada for giving me mental and moral support in the highs and lows of this PhD journey. I appreciate my lovely daughter Pravakshya Sharma for showering her love and affection during my PhD work.

Date: 21-06-2021

A handwritten signature in black ink, appearing to read 'Anuj Sharma', with a horizontal line underneath.

(Anuj Sharma)

ABSTRACT

Industrial development is one of the pioneer enablers of the economic and social prosperity of any nation. High efficiency, low cost and reliable system are the most critical factors that are focussed by industries. New developments in this direction are observed in the past few decades. Researchers thrive for new inventions and technologies by which high-quality output can be attained with effective and robust systems. Materials play an essential role in achieving high efficiency by providing an outcome-based response to any process. With the advent of composite materials, industries have started focusing on using lighter weight materials with the same mechanical properties. Metal matrix composites have the edge over the parent metals for rotor applications as it has a higher specific modulus and specific modulus is the critical material factor for vibration responses. Aluminium /alumina MMCs have shown prominent growth in the composite material market because of their compatibility with the rotor systems. Several types of research are available for the development of aluminium based metal matrix composites for industrial applications.

The main focus of this research is to propose a method of development of metal matrix composite for specific rotary applications. This work focuses on the development, characterization and dynamic analysis of the metal matrix rotor. The rotors are developed through a cost-effective, flexible, and readily available method called the stir casting process.

The physical properties of the composites depend primarily on the homogeneity and the fraction of reinforcement in the matrix. The uniformity and the concentration have been enhanced by optimizing process parameters in various researches. However, these

researches are based on the qualitative analysis (visual observation) of the microstructure of composites. These qualitative methods do not assist in providing numerical and objective-oriented results. Therefore, these methods lack a objective judgment that is crucial for comparing the dispersion of reinforcements consistently. Therefore, quantitative measurement of dispersion is essential for optimizing the process parameters in order to attain better results.

There are several techniques for the quantitative measurement of particle dispersion in the matrix. The mean free path has been calculated by dividing micrograph images into multiple grid lines and was utilized for quantifying particle dispersions. The quantitative distribution index and area fraction may be beneficial in optimizing the process parameters and providing more authentic and reliable results than the qualitative analysis. There are various methods used for parametric optimization having multivariant parameters. Box-Behnken designs (BBD) are rotatable or nearly rotatable second-order designs based on three-level incomplete factorial designs. BBD is one of the main types of response surface design, the other being central composite design. The BBD design requires a smaller number of runs as compared to the central composite design. The Box-Behnken design operates within the range of parameters and does not generate experimentation points beyond the range of parameters like the central composite design. BBD is suitable for designs where the range of operations are constrained by manufacturing conditions. In this work, a novel technique has been adopted where newly developed quantitatively assessed responses are used for process optimization instead of conventional qualitative analysis and thus, it provides a profound methodology for optimization of process parameters.

A novel characterization approach has been adopted in this work, which determines the effect of reinforcements on the dynamic properties and residual stress of the Al 6061/Al₂O₃ shafts. Long and slender shafts were fabricated through a stir casting process. Grain structure has been obtained through optical microscopy, and morphological evaluation of the composites was performed through Scanning Electron Microscopy (SEM). In addition to that, an X-ray diffraction pattern (XRD) were analyzed, and residual stress was calculated by X-ray residual stress measurement system μ -X360 Ver. 2. 3. 0. 1. Tensile strength and microhardness were also determined in this analysis for various compositions of the composite material.

For composite materials, the system response changes abruptly with a change in the properties of the material. Therefore, attaining significant knowledge about the effect of material composition on material properties is crucial. The researchers are looking for new computational methods which can predict these alterations so that the effort in experimental testing can be reduced. In this direction, this paper presents a robust and novel methodology of validating the estimation of the composite's effective properties through a multi-scale approach by a set of standardized experimentation. These effective properties are estimated through the mean-field homogenization technique, whose parameters are driven from the image analysis of Scanning Electron Microscopy (SEM) images. The predicted results are validated with the results obtained by the experimentation as per ASTM E1876 standard.

This research work has adopted a novel approach of providing a dedicated methodology for determining the calibrated internal damping factor for bond graph dynamic analysis, which has been used in various literature for transient and stable

responses. The investigation has been performed on long and slender shafts of the metal matrix composites. An insight into the change in dynamic response with the difference in the composition of composite shafts is provided in this work.

Many valuable insights and findings were obtained in this work related to the development and response of different compositions of metal matrix composite shafts. The optimization of the stir casting parameters using a quantitative distribution index and area fraction resulted in uniformly distributed composite shafts. The mechanical properties such as tensile strength, microhardness, specific modulus increased with the addition of reinforcement in the composite up to a particular limit. Above that limit, the agglomeration and porosity become prominent factors and further depletes the properties of a composite. The natural frequency of the composite shaft increased, and the amplitude of vibration was reduced for the composites with a high volume fraction of reinforcements. The values of Young's modulus of different compositions determined through computation were congruent with the experimental results. The dynamic response was simulated using bond graph analysis, and it was observed that the amplitude of orbits was also reduced for the composites with a high volume fraction of reinforcements.

TABLE OF CONTENT

Topics	Page No.
Declaration	i
Certificate	ii
Acknowledgement	iv-v
Abstract	vi-ix
Table of Contents	x-xv
List of Figure	xvi-xx
List of Table	xxi-xxiii
Nomenclature	xxiv-xxv
Chapter 1: Introduction	1
1.1 Motivation	1
1.2 Composite materials	2
1.3 Classification of composites	3
1.3.1 Classification based on Reinforcement	4
1.3.1.1 Fibre-reinforced composite	4
1.3.1.2 Particle-reinforced composite	6
1.3.1.3 Structural composite	7
1.3.2 Classification based on matrix	8
1.3.2.1 Metal Matrix Composites (MMC)	8
1.3.2.2 Ceramic Matrix Composites (CMC)	9

1.4	Primary processing of composites	9
1.4.1	Solid-state processing	10
1.4.1.1	Powder blending	10
1.4.1.2	Diffusion Bonding	11
1.4.1.3	Physical vapour deposition	11
1.4.2	Liquid-state processing	13
1.4.2.1	Stir Casting	13
1.4.2.2	Infiltration process	13
1.4.2.3	Spray deposition	14
1.4.2.4	In-situ processing	15
1.5	Properties of composites	16
1.5.1	Flexural strength	16
1.5.2	Wear Resistance	16
1.5.3	Impact Strength	17
1.5.4	Corrosion resistance	17
1.5.5	Lightweight	17
1.5.6	Damping	18
1.5.7	Temperature resistance	18
1.6	Application of composites	18
1.6.1	Transportation	19
1.6.1.1	Braking and Clutch System	19
1.6.1.2	Driveshaft	19
1.6.1.3	Engine Body	19

1.6.1.4	Automotive body parts	20
1.6.2	Aerospace	20
1.6.2.1	Aircraft brakes	20
1.6.2.2	Aircraft Structure	20
1.6.2.3	Gas turbine	20
1.6.2.4	Aircraft seats and fabric	21
1.6.3	Defence	21
1.6.4	Biomedical	21
1.7	Metal matrix composites for rotor applications	22
1.8	Specific application of metal matrix composites	23
1.9	Discrete alumina reinforced aluminium 6061 composite shafts for rotor applications	24
1.9.1	Aluminium 6061	24
1.9.2	Alumina (Al_2O_3) as reinforcement	26
1.10	Characterization of metal matrix composite	27
1.10.1	Microstructure	27
1.10.2	Tensile strength and elastic modulus	27
1.10.3	Hardness	28
1.10.4	Composition analysis and Residual Stress	28
1.11	Multi-scale modelling of metal matrix composite.	28
1.11.1	Image analysis of microstructure	28
1.11.2	Prediction of effective properties	28
1.11.2.1	The Generalized Method of cells (GMC)	29

1.11.2.2	The Equivalent Modulus Beam Theory (EMBT)	29
1.11.2.3	The Modified EMBT	30
1.11.2.4	Simplified Homogenized Beam Theory (SHBT)	30
1.11.2.5	Layerwise Beam Theory	31
1.12	Dynamic analysis of metal matrix composite	31
1.13	Thesis scope	31
1.14	Contribution of present work	32
1.15	Organisation of thesis	32
	Chapter 2: Literature Review	34
2.1	Applications of metal matrix composite as rotor	34
2.2	Development of metal matrix composite material	35
2.3	Characterization of metal matrix composite material	51
2.4	Computation of effective properties	53
2.5	Dynamic analysis of metal matrix composite rotor	58
2.6	Experimental validation	61
2.7	Outcome of literature review	62
2.8	Problem statement	63
2.9	Thesis objectives	63
2.10	Research methodology	63
2.11	Summary	64
	Chapter 3: Development of metal matrix composite	65
3.1	Introduction	65
3.2	Image analysis method	68

3.3	Box-Behnken design for parametric optimization	71
3.4	Results and discussion	73
3.4.1	Pareto analysis of variance (ANOVA) and coefficient of determination (R^2)	73
3.4.2	Response surface analysis	79
3.4.3	Solution and validation	82
3.5	Summary	86
	Chapter 4: Characterization of metal matrix composite	88
4.1	Optical microscopy	88
4.2	Scanning electron microscopy	89
4.3	X-ray diffraction	90
4.4	Residual stress	93
4.5	Microhardness	95
4.6	Tensile test	98
4.7	Density and porosity	99
4.8	Results and discussions	101
4.8.1	Microstructure and composition analysis	101
4.8.2	Residual stress analysis	107
4.8.3	Microhardness	110
4.8.4	Tensile strength	110
4.8.5	Density and porosity	111
4.8	Summary	113
		115

Chapter 5: Computation and experimental validation of effective properties	
5.1	Introduction 115
5.1.1	Estimation of effective mechanical properties through mean-field homogenization by using parameters extracted through image processing 115
5.1.2	Experimental evaluation of Elastic properties 119
5.2	Results and discussion 122
5.3	Summary 136
Chapter 6: Dynamic analysis of MMC rotor	138
6.1	Bond graph modelling 138
6.2	Simulation 146
6.3	Summary 155
Chapter 7: Conclusions and scope for future work	157
7.1	Conclusions 157
7.1.1	Material and method 157
7.1.2	Development of metal matrix composites 157
7.1.3	Characterization of metal matrix composite 158
7.1.4	Computation and experimental validation of effective properties 158
7.1.5	Dynamic analysis of MMC rotor 159
7.2	Future Scope 160
References	161
List of Publications	169

LIST OF FIGURES

Figure No	Title	Page No.
Fig. 1.1:	Classification based on reinforcement	3
Fig. 1.2:	Classification based on matrix	4
Fig. 1.3:	Fibre-reinforced composites	4
Fig. 1.4:	Particle reinforced Composites	5
Fig. 1.5:	Laminar Composites	7
Fig. 1.6:	Sandwich Honeycomb Structure	8
Fig. 1.7:	Powder blending	10
Fig. 1.8:	Diffusion bonding	11
Fig. 1.9:	Microstructure of multilayered Al/SiC composite deposited by PVD	12
Fig. 1.10:	Vortex generation in stir casting set-up	12
Fig. 1.11:	Squeeze casting, infiltration setup	13
Fig. 1.12:	Spray deposition	14
Fig. 1.13:	In-situ Processing of composite in unidirectional solidification	15
Fig. 3.1:	(a) Stir casting set up	65
	(b) Stir casting set up	65
	(c) Stir casted shaft	65
	(d) Sand casting setup	66
Fig. 3.2:	Proposed Methodology for quantifying homogeneity through image analysis method.	68

Fig. 3.3:	(a) 8-bit grayscale SEM image	70
	(b) Binary image	70
	(c) Denoised image with analyzed particles in elliptical form	70
	(d) Grid formation of the image	70
Fig. 3.4:	Convergence of D_{index} values for 2N number of lines	71
Fig. 3.5:	Residual vs Run plot for D_{index}	75
Fig. 3.6:	Dissipated scatter plot for D_{index}	76
Fig. 3.7:	Residual vs Run plot for area fractions for 2N number of lines	77
Fig. 3.8:	Dissipated scatter plot for area fractions for 2N number of lines	78
Fig. 3.9:	Response surface analysis of D_{index} vs various parameters	80
Fig. 3.10:	Response surface analysis of area fraction vs various parameters	81
Fig. 3.11:	Optimal parameters and the response at these values	82
Fig. 3.12:	Image analysis of composite fabricated at optimized parameters	83
Fig. 3.13:	(a) EDS analysis of the composite	84
	(b) EDS maps of the distribution of oxygen (O Ka 1)	84
	(c) EDS maps of the distribution of aluminium (Al Ka 1)	84
Fig. 3.14:	Pores observed in the composite material matrix	86
Fig. 4.1:	Measurement of strain in Debye-Scherrer ring in $\cos\alpha$ method	95
Fig. 4.2:	(a) ASTM E8M-04 standard specimen size	97

	(b) Composite specimen prepared	97
Fig. 4.3:	Gaussian fit for peak at $[^{\circ}2 \text{ Theta}] = 38.4035$	100
Fig. 4.4:	(a) Optical micrograph of Al 6061	102
	(b) Optical micrograph of Al 6061/6wt.% Al_2O_3	102
	(c) Optical micrograph of Al 6061/12 wt. % Al_2O_3	102
	(d) Optical micrograph of Al 6061/18wt.% Al_2O_3	102
Fig. 4.5:	(a) SEM image of Al 6061	103
	(b) SEM image of Al 6061/6wt.% Al_2O_3	103
	(c) SEM image of Al 6061/12wt.% Al_2O_3	103
	(d) SEM image of Al 6061/18wt.% Al_2O_3	103
Fig. 4.6:	(a) Ruptured and scratched surface due to agglomeration of particle for MMC sample with 24% alumina particle reinforcement at 500X.	104
	(b) High resolution image showing porosity induced due to agglomeration at 2000 X.	104
Fig. 4.7:	(a) XRD diffraction pattern of Al_2O_3 powder (b) Al 6061 sample	105
	(b) XRD diffraction pattern of Al 6061 sample	105
Fig. 4.8:	(a) Waterfall model of XRD pattern of composites	106
	(b) Cascade model of XRD pattern of composites	106
Fig. 4.9:	(a) 3D Debye ring and distortion for Al 6061	108
	(b) 3D Debye ring and distortion for Al 6061/6wt.% Al_2O_3	108
	(c) 3D Debye ring and distortion for Al 6061/12wt.% Al_2O_3	108

	(d) 3D Debye ring and distortion for Al 6061/18wt.% Al ₂ O ₃	108
Fig. 5.1:	(a) SEM Image of a composite sample	116
	(b) Cropped SEM image converted into a binary image	116
	(c) Particle analyzation of the binary image	116
	(d) RVE with mean aspect ratio, size and volume fraction.	116
Fig 5.2:	Experimental set up for impact hammer	119
Fig. 5.3:	First and second bending mode with sensor positioning.	121
Fig. 5.4:	FRF and coherence for Al6061	128
Fig. 5.5:	FRF and coherence for Al6061/ 6 wt. % Al ₂ O ₃	129
Fig. 5.6:	FRF and coherence for Al6061/ 12 wt. % Al ₂ O ₃	130
Fig. 5.7:	FRF and coherence for Al6061/ 18 wt. % Al ₂ O ₃	131
Fig. 5.8:	Comparison of range of predicted and experimental value of In-plane	136
Fig. 6.1:	Rotor system with DC motor drive and pin-pin end condition.	138
Fig. 6.2:	Force and Moment on a Rayleigh beam.	139
Fig. 6.3:	Velocity Transformation capsule.	140
Fig. 6.4:	Insight of the spinning shaft mechanism	141
Fig. 6.5:	Capsule of the spinning shaft	142
Fig. 6.6:	Spinning hub capsule	143
Fig. 6.7:	Bond graph model by connecting sub models	143
Fig. 6.8:	Internal Damping calibration	147

Fig. 6.9:	Mapped plots for calibrated internal damping coefficients.	150
Fig. 6.10:	Displacement response for modelling impact hammer response.	151
Fig. 6.11:	Response for first mode excitation in bond graph	152
Fig. 6.12:	Whirl orbits or the response of the MMC shafts in first and second mode.	154

LIST OF TABLES

Table No	Title	Page No.
Table 1.1	Series of wrought aluminium alloy	25
Table 1.2	Suitable reinforcements for the metal matrix	26
Table 3.1	Response of 29 sets of experiments determined by Box- Behnken design	72
Table 3.2	ANOVA analysis for D_{index}	73
Table 3.3	Coefficient of determination (R^2) analysis	74
Table 3.4	ANOVA analysis for area fraction	76
Table 3.5	Coefficient of determination (R^2) analysis for area fraction	77
Table 3.6	Comparison of confirmation test range and experimental value at optimized parameters	84
Table 4.1	Essential Specification: EVO 50	89
Table 4.2	X-Ray Diffraction machine specification	92
Table 4.3	PULSTEC μ -X360n Specification	94
Table 4.4	Specification of Microhardness testing machine (Struers Duramin-40)	96
Table 4.5	Tinius Olsen H50KS UTM Specification	98
Table 4.6	Peak report for an Al 6061 alloy	107
Table 4.7	Residual stress for different materials	109
Table 4.8	Microhardness for different materials	110

Table 4.9	Tensile strength of the specimen	111
Table 4.10	Density of the specimen	112
Table 4.11	% Porosity of the different materials	112
Table 5.1	Mean volume fraction, aspect ratio and particle size for various SEM images	123
Table 5.2	Image analysis overall mean results	124
Table 5.3	Initial set of standard values for Al 6061	125
Table 5.4	Mean-field homogenization results for 6 wt. % Al ₂ O ₃ /Al 6061	125
Table 5.5	Mean-field homogenization results for 12 wt. % Al ₂ O ₃ /Al 6061	126
Table 5.6	Mean-field homogenization results for 18 wt. % Al ₂ O ₃ /Al 6061	126
Table 5.7	Experimental natural frequency mean, standard deviation and range	132
Table 5.8	Experimental damping mean, standard deviation and range	132
Table 5.9	Experimental amplitude mean, standard deviation and range	133
Table 5.10	Comparison of Predicted and experimental value	134
Table 6.1	Parameters for simulation.	146
Table 6.2	Experimental and bond graph Damping ratio for approximate value.	148
Table 6.3	Calibrated internal damping factor for different MMC shaft.	149

Table 6.4	Comparison of result after calibrated internal damping factor for different MMC shaft.	153
-----------	---	-----

NOMENCLATURE

Abbreviation	Details
WEF	World Economic Forum
GDP	Gross Domestic Product
<i>MMC</i>	Metal Matrix Composites
<i>CMC</i>	Ceramic Matrix Composites
<i>PMC</i>	Polymer Matrix Composites
PM	Powder Metallurgy
<i>PVD</i>	Physical Vapour Deposition
DIMOX	Directional Oxidation Of Metal
CFC	Carbon Fiber Composites
RVE	Representative Volume Element
FRF	Frequency Response Function
SEM	Scanning Electron Microscopy
XRD	X-Ray Diffraction
DSR	Debye–Scherrer Ring
FEM	Finite Element Method
MT	Mori- Tanaka
ASTM	American Society For Testing And Materials
CNT	Carbon Nanotubes
MWCNT	Multi Walled Carbon Nanotubes
EDS	Energy Dispersive X-Ray Spectroscopy

RPM	Revolution Per Minute
D_{index}	Distribution Index
ANOVA	Analysis Of Variance
R^2	Coefficient Of Determination
DC	Direct Current

Introduction

1.1 Motivation

With the advent of Industry 4.0, there is an incessant quest for advanced technologies that ensure high and optimum productivity across the entire manufacturing industry spectrum [1]. In the development of a nation, the manufacturing sector has been a pioneer enabler in transforming society both socially and economically. India is continuously working in this direction, and in an assessment by the World Economic Forum (WEF) in January, it ranked 30th in the global manufacturing index [2]. The Government of India aims to increase the manufacturing sector share from 16 to 26 per cent of the gross domestic product (GDP) by 2022. The machinery in the manufacturing sector is the heart of industries, responsible for the high scale operation of industries. Rotary machines are the most vital components of the modern industrial sector. Catastrophic failures of such elements have a colossal effect on the system. Several efforts had been made to reduce the probability of these kinds of failures. Many rotor faults can lead to catastrophic failure if undetected timely and correctly. Therefore, the study and investigation of rotor dynamics are a matter of concern for the last four decades.

Modern industries face various challenges related to performance, economy, emissions, aesthetics, safety, quality and profitability on a daily basis. With cut-throat competition prevailing in the market, industries continuously search for new and innovative ideas for low cost and high-value operations. In this direction, research on materials that could fulfil the need of industries to provide efficient working system is in high demand. This has led to the

invention of novel materials that can have high strength and low weight properties. These materials are composed of a continuous phase (matrix material) and a discrete phase (reinforcements), commonly referred to as composite material. Tailorable properties can be achieved by altering the composition and size of the reinforcements, and a new domain of properties can be achieved. Metal matrix composites are one of the types of composites that are most common in rotor applications.

The physical, mechanical and dynamic properties change abruptly due to the change in material composition. Therefore, there is always a need to develop a thorough and detailed analysis for these composite rotors. The detail about the composite material is provided in the next section.

1.2 Composite Materials

Composites are the combination of two or more different constituents in the form of the composition of materials. There are significant differences in the chemical, dynamic and physical properties of the constituents of composites. Although, in the form of composites, a different kind of material can be developed, which possesses unique characteristics that are highly preferable for the desired application compared to the referred constituents. This improvement in the properties makes composites a priority for the different kind of applications [3,4]. There are many examples of composites, but one of the most common examples of composites around us exists in nature. For example, wood is a natural composite made of organic polymer lignin as a base material infused with fibrous chains of cellulose molecules [5,6]. Bone is also an example of a natural composite composed of an organic material matrix called collagen, reinforced by hydroxyapatite inorganic crystals [7]. Composites differ from mixtures like alloys and solid solutions. As in the case of composites, the reinforcement and matrix do not dissolve or blend. Instead of losing their identities, both matrix and reinforcement

are synergistically combined and contribute to the enhancement of the final product's properties [8,9]. With the help of microscopic analysis, the characteristics of the distinct components in the form of matrix and reinforcement can be identified. Therefore, it can be stated that the composite is an amalgamation of two or more different constituents in which one of them is the base material, whereas others will be working as the filler materials. The base material binds the filler materials in the composite and is termed as the matrix material. On the other hand, filler material is distributed in the matrix as particles, fibres, whiskers and fragments and are termed as reinforcements [10,11]. The matrix material is generally a soft phase constituent with better ductility, thermal conductivity and formability in which reinforcement with low thermal expansion, high strength and high stiffness are embedded [12]. The composites are broadly classified on the basis of reinforcement and matrix, as illustrated in the next section.

1.3 Classification of Composites

The composites can be classified as follows:

1. Based on Reinforcement
2. Based on Matrix

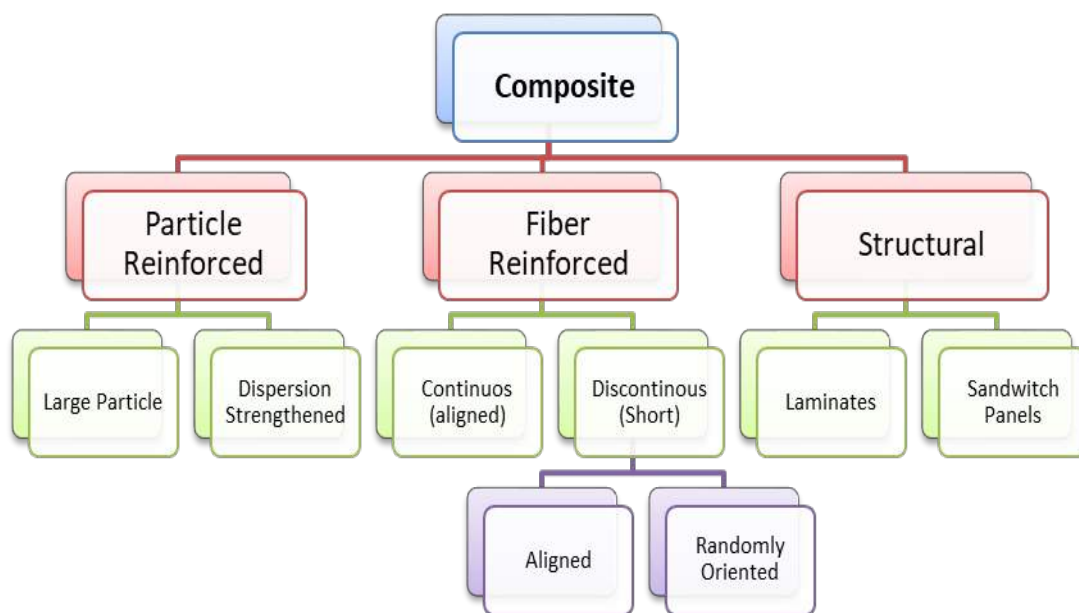


Fig. 1.1: Classification based on reinforcement

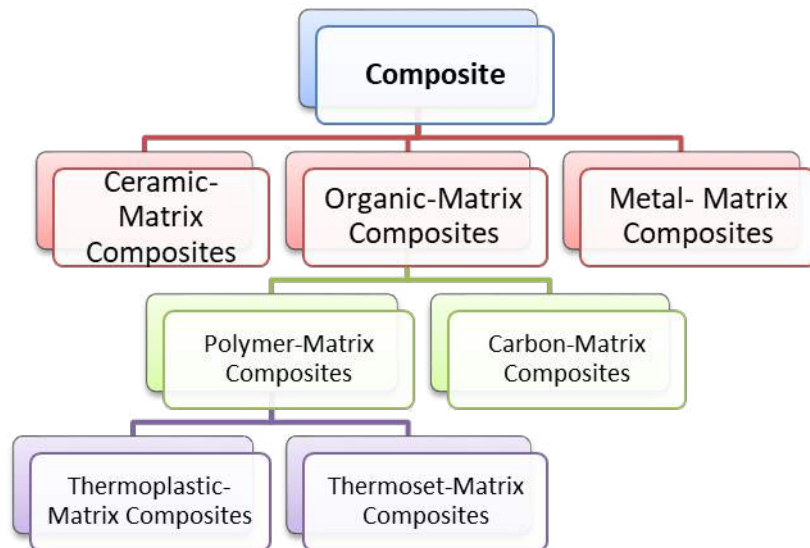


Fig. 1.2: Classification based on matrix

Classification based on Reinforcement is shown in Fig. 1.1, classification based on matrix is shown in Fig. 1.2.

1.3.1 Classification based on Reinforcement

1.3.1.1 Fibre-reinforced composite

In Fibre-reinforced composite materials, the softer matrix material is embedded with high strength fibres to develop composites with high strength to weight ratios, as shown in Fig. 1.3. The load is transmitted from the matrix to the fibres, where the developed stress is absorbed.

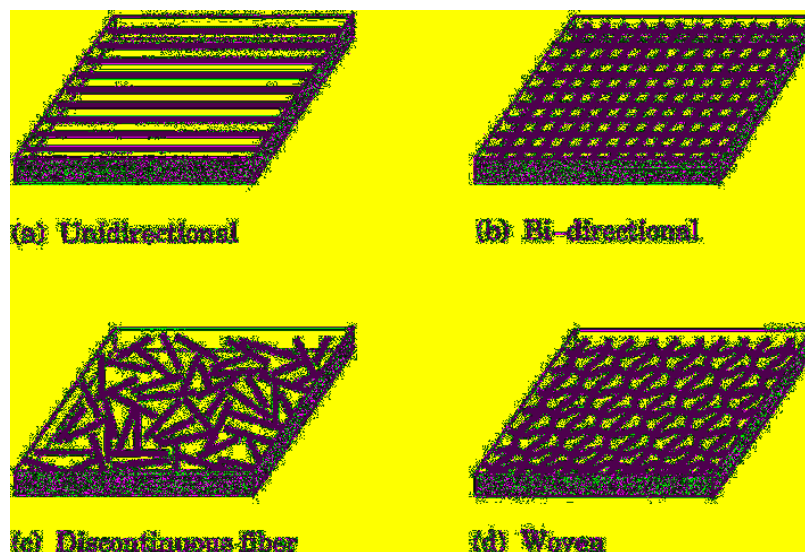


Fig. 1.3: Fibre reinforced composites

The aspect ratio is one of the prominent factors in these composites. It is the ratio of the longitudinal to the lateral dimensions and affects the strength of the composites. In various researches, it has been observed that composites that have reinforcement with a higher aspect ratio have higher strength. Fibres are long particles that have a high aspect ratio and possess better mechanical properties such as high wear resistance, high stiffness, high thermal resistance and high chemical resistance. The fibre shaped reinforcements such as Kevlar, basalt, carbon fibre, boron fibre and glass fibre can be embedded in the matrix material to form fibre-reinforced composites. Recently, various researchers have frequently used fibre reinforced composites with natural fibre reinforcement since the use of chemically treated natural fibre shows better fatigue strength and impact toughness. Moreover, these reinforcements are abundant and readily available, eco-friendly, low-cost, and have a low density than synthetic fibres [13,14]. Fibre-reinforced composites are further classified into continuous or discontinuous fibre-reinforced composites. The continuous fibre-reinforced composites contain long fibres aligned in a specific orientation, whereas discontinuous fibre reinforced composites contain short fibres that are either aligned or discretely oriented in different random directions. The aligned fibre reinforced composites can provide composites with orthotropic properties that change with direction.



Fig. 1.4: Particle reinforced Composites

1.3.1.2 Particle-reinforced composite

In particle reinforced composites, reinforcements have a low longitudinal to lateral dimension ratio (aspect ratio). As shown in Fig. 1.4, the particles are mixed in the matrix material and form a composite material. Due to this reason, particle-reinforced composites have less strength as compared to fibre reinforced composites. But particle reinforced composites have significant application in rotating or friction elements since they provide better wear resistance and thermal tolerance than fibre-reinforced composites. Particle reinforced composites also have applications in the development of road surfaces, civil structures and tyres. For example, by adding gravels as a reinforcement in the cement matrix, significantly high hardness and strength can be achieved. The low production and fabrication cost is also one of the significant advantages of particle reinforced composites [15,16]. The particle reinforced composites are also classified as large particle composites and dispersion strengthening composites. In large-particle composites, reinforced particles are large enough, and the interaction between the particle and matrix cannot be treated on the molecular or atomic level. Therefore, the properties are determined with a simple rule of the mixture by the combination of the product of volume fraction and the respective property. The Young's modulus of elasticity of composites can be predicted by the rule of mixtures is given as relationship of elastic modulus of the matrix (E_m) and the particulate (E_p) phases by:

$$E_c = E_m V_m + E_p V_p$$

where V_p and V_m are the volume fraction of the two phases. Similarly, a lower bound can be expressed as:

$$E_c = E_m E_p / (E_p V_m + E_m V_p)$$

In dispersion type particle reinforced composite matrix is embedded by small particulates or dispersions. The strengthening mechanism is Orowan strengthening mechanism, in which the strength is attained by blocking the dislocations. These dispersed reinforcement particles are

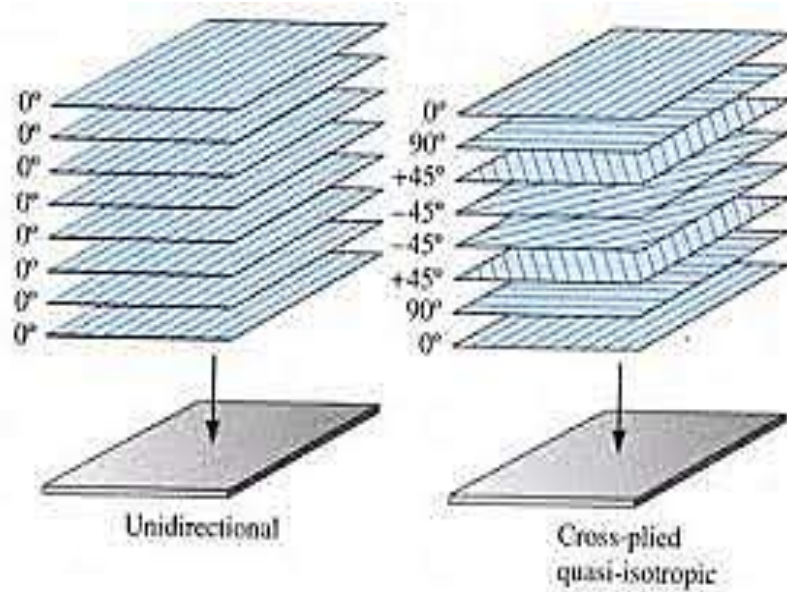


Fig. 1.5: Laminar Composites

usually hard, brittle and high strength material either in oxides or carbide form. The interactions of the matrix and the particle are on the level of molecular or atomic level.

1.3.1.3 Structural composite

Structural composites are classified into two types: Laminates reinforced composites and Sandwich panels. Laminates or laminar composites are layer-based composites. In these composites, the layers are stacked with different orientation in each layer. As shown in Fig. 1.5, the layer can be unidirectional or cross plied as required for a specific application of anisotropic or quasi-isotropic application.

They are applicable when multidirectional stresses are imposed on the material. These composites are strong and lightweight and are used in many applications in aerospace and transportation. Plywood is the general application of the laminates type composites.

The sandwich structures are another type of composites that have a thin layer of facing material on the boundary of the structure, and the inner part is a cob core such as a metal expanded structure or a polymer foam. For example, corrugated cardboard is a sandwich structured composite where two faces of thin paper are filled with a corrugated sheet. In this kind of structures, the core provides strength, and the thin sheets are the facing materials that hold the

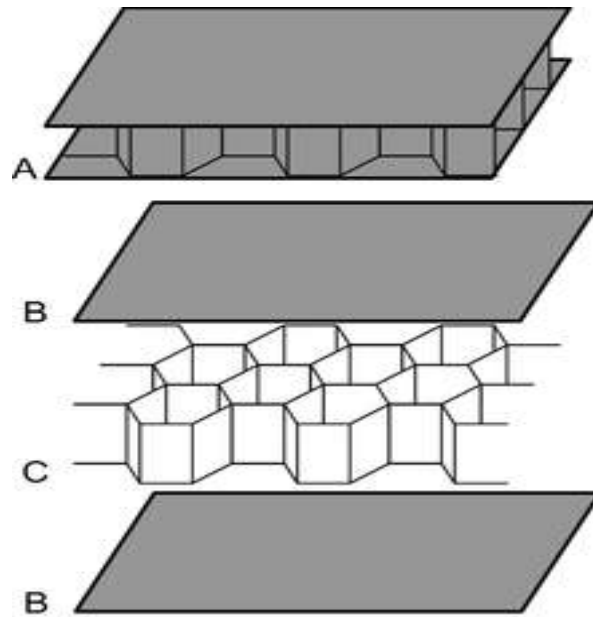


Fig. 1.6: Sandwich Honeycomb Structure

core. The honeycomb structure is one of the most famous structures, which is used for attenuation purpose. In this kind of structure, interlocking hexagonal cells forms the core and fixed by thin films, as shown in Fig. 1.6. The examples of facing materials include plywood, titanium, steel, fibre reinforced composites and aluminium [17].

1.3.2 Classification based on matrix

1.3.2.1 Metal Matrix Composites (MMC)

In metal matrix composites, the matrix is compulsorily a metallic material that binds the reinforcement to form a composite. The matrix material are mostly titanium, magnesium, aluminium, iron, cobalt or copper) and reinforcements of different forms can be embedded in the matrix. The metal needs a high temperature to bind the reinforcement, and thus heating equipment is a must for the fabrication of metal matrix composites. The volume percentage of the reinforcement can vary from a low to around fifty per cent of the total volume. Aluminium matrix composites are aluminium-based metal matrix composite with a wide range of applications in the automobile and aerospace industries. The wide range of aluminium alloys can provide a suitable matrix for different reinforcements, and especially ceramic

reinforcement such as silicon carbide (SiC) and alumina (Al_2O_3) can be effectively mixed with the molten or powder form aluminium alloy [18].

1.3.2.2 Ceramic Matrix Composites (CMC)

Brittleness is the most critical drawback of the ceramic material, and CMCs were introduced to overcome this drawback. The failure strain of the fibres is much higher than the failure strain of the ceramic matrix, and thus CMCs are also termed as inverse composites. Whereas in MMC and polymer matrix composite, the phenomenon is entirely different. CMCs have ceramics as a matrix and is generally reinforced by silicon nitride(SiN), aluminium oxide (Al_2O_3), SiC and carbon fibre. The CMCs are fabricated through Gas or Liquid process route where the matrix and the internal phase are developed around the reinforcement from gas or liquid precursors [19].

1.3.2.3 Polymer Matrix Composites (PMC)

The matrix material for the PMCs is essentially a polymer material and is reinforced by metal fibres, glass fibres, carbon fibres and Kevlar. Thermoplastic and Thermoset plastic are the two different types of PMCs. Since thermosets have higher strength and resistance to high temperature than thermoplastics, they are more prevalent in various applications. Thermosets are manufactured by the same process as thermoplastics, although a specific hardener is mixed in the resin during solidification. The PMCs have various significant advantages, such as simple fabrication, low cost, easy handling, and lightweight.

1.4 Primary processing of composites

On an industrial scale, the primary processing of composites can be classified into the following groups:

- (1) Solid-state processes.
- (2) Liquid-state processes.

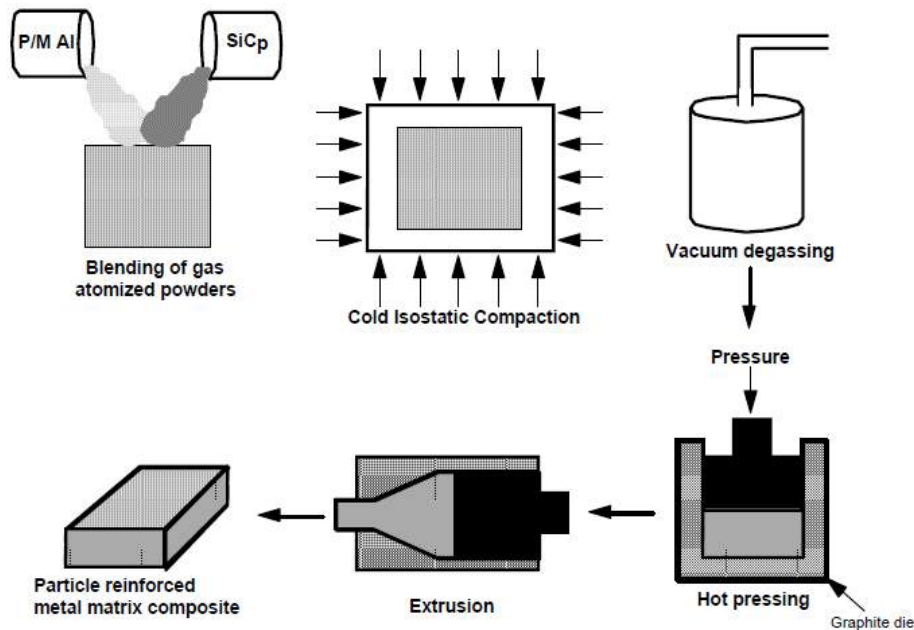


Fig. 1.7: Powder blending

1.4.1 Solid-state processing

In solid-state processing, all the constituents are in solid form and are joined by the application of high pressure and temperature. Solid-state processing is classified into the following:

1.4.1.1 Powder blending

Powder blending is a versatile method for manufacturing metal matrix composites with ceramic short particles, whiskers, or fibres. As shown in Fig. 1.7, in this method, the blend of the mixture of matrix and reinforcement are pressurized with cold isostatic compaction and then degassed, hot pressed and extruded. This technique can be performed in both dry or liquid suspension. The operation of powder blending can be followed by a high-temperature consolidation stage, degassing, canning, cold compaction, extrusion or hot isostatic pressing. This operation is also known as Powder Metallurgy (PM) method, and the processed material contains plate-like particles oxides. The size of these oxides is in nm (nanometer), and the volume fraction ranges from 0.04 to 0.49, and these variations depend on process condition

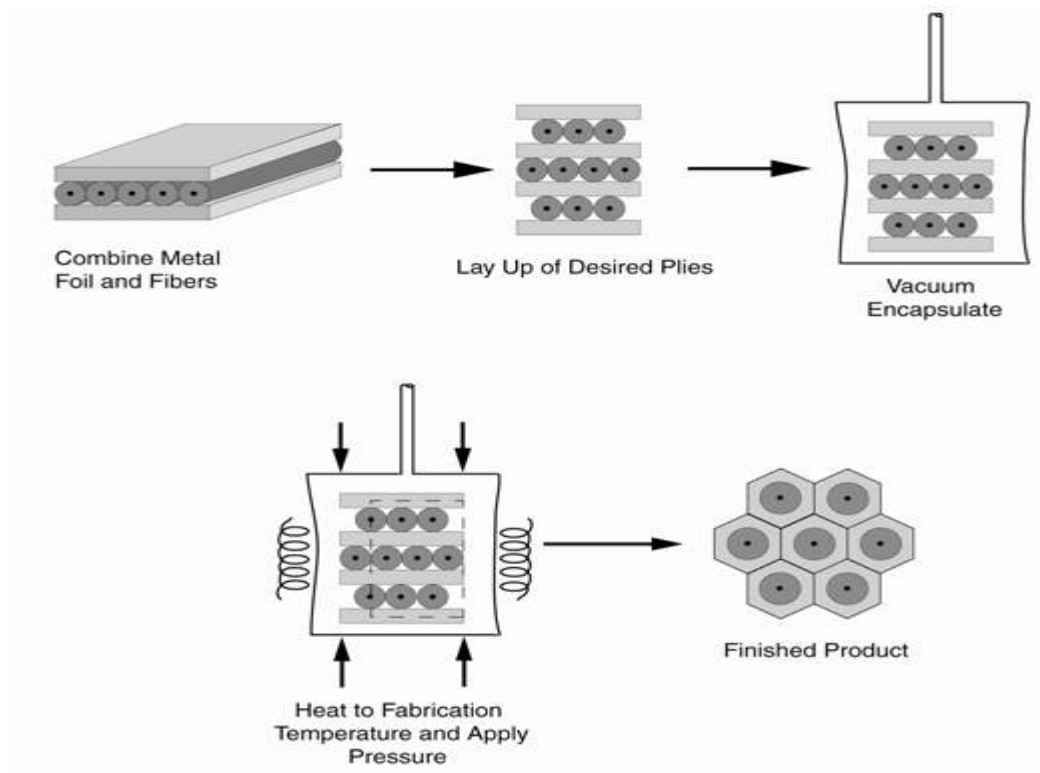


Fig. 1.8: Diffusion bonding

and power preconditions. These oxides are very fine and strengthen the composite and strongly affect the heat-treated properties of the material.

1.4.1.2 Diffusion Bonding

In the diffusion bonding process, the matrix material is deposited on the surface of the fibre in the form of foil-fibre-foil. The diffusion bonding process includes combining metal foil and fibre followed by layup of desired plies, vacuum encapsulation and heating, as shown in Fig. 1.8. The thicker layer of the evaporated matrix material diffuses with the fibre and form the composite. This process is suitable mainly for monofilament reinforced metal matrix composites. Titanium-based monofilament fibre composite is commonly produced by this method. Since it is difficult to obtain homogenous distribution and large volume fraction of fibre, it is unsuitable for the production of components with complex shape.

1.4.1.3 Physical vapour deposition (PVD)

In this process, the fibre is continuously passed through a region of high partial pressure, where the evaporated metal is deposited on the fibre. The deposits of the matrix material form a thick

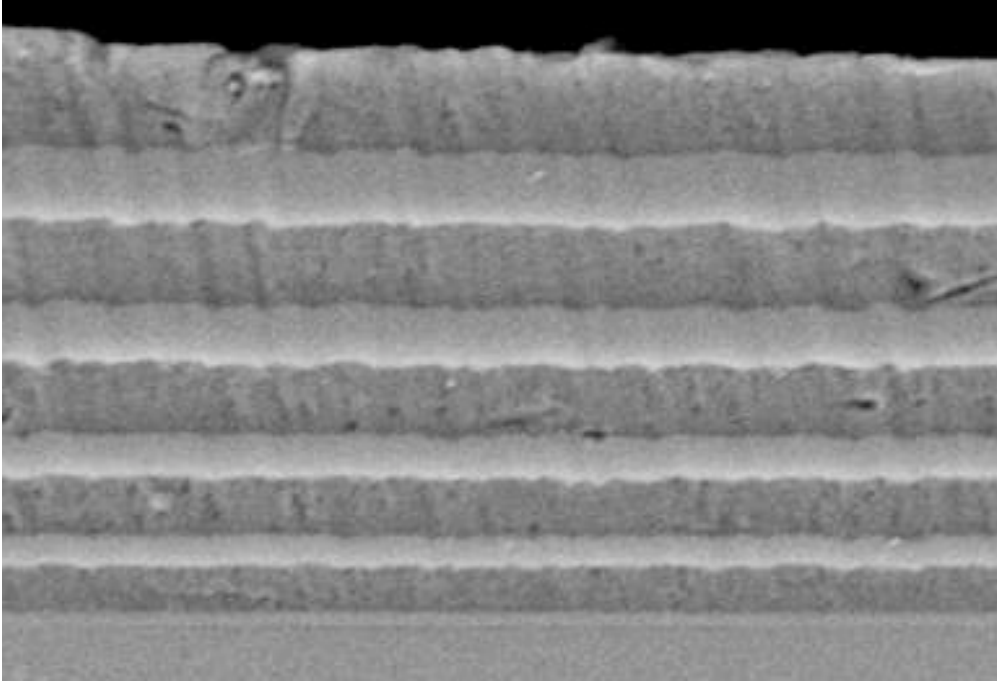


Fig. 1.9: Microstructure of multilayered Al/SiC composite deposited by PVD layer on the fibre as a coating. A high power electron beam produces vapour of the matrix material, which is deposited with a rate of 4 to 11 μm (micrometre) /minute. This technique can produce composites with uniform distribution of fibre and volume fraction as high as 80%. The microstructure of the physical vapour deposition is shown in Fig. 1.9.

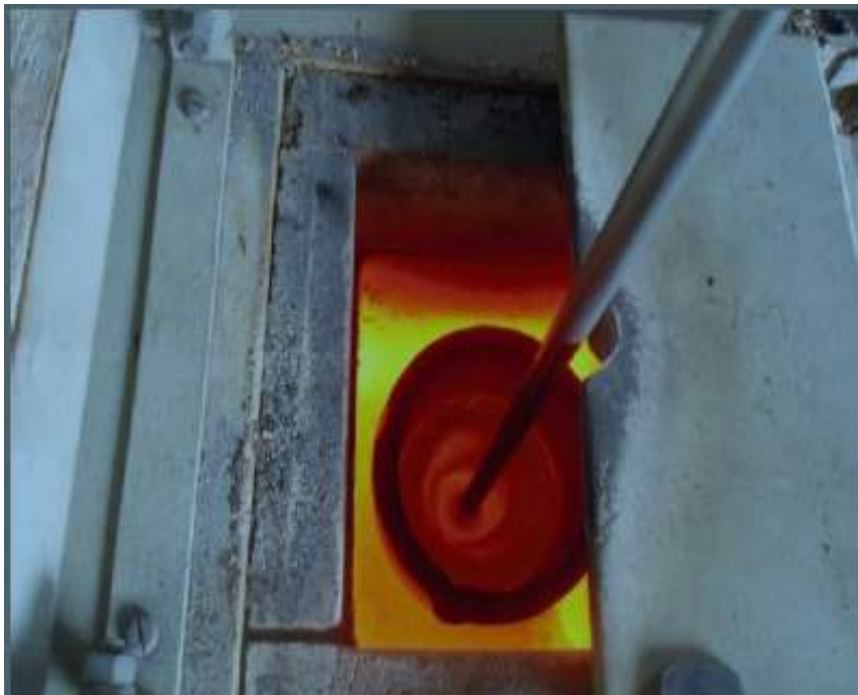


Fig. 1.10: Vortex generation in stir casting set-up

1.4.2 Liquid state processing

In this method, the matrix material is melted into liquid form, and the composite is formed with the interaction of the matrix material with reinforcement.

1.4.2.1 Stir Casting

In the stir casting method, the matrix material is fed in a crucible and melted into a liquid form. When the matrix material is melted, the ceramic particles are mixed into the molten material, and then the mixture is stirred with a stirrer. As shown in Fig. 1.10., the vortex generated by the stirring action allows a better wetting of the reinforcement and the liquid melt. Stir casting is the most economically viable solution for the development of composites. It is best suited for the large-sized reinforcement since it can provide a homogenous composite by setting the parameters of the stir casting setup.

1.4.2.2 Infiltration process

In the infiltration process, a preheated preforms are placed in the chamber, and then liquid metal is injected into the porous preforms of the reinforcements. Infiltration can be in various

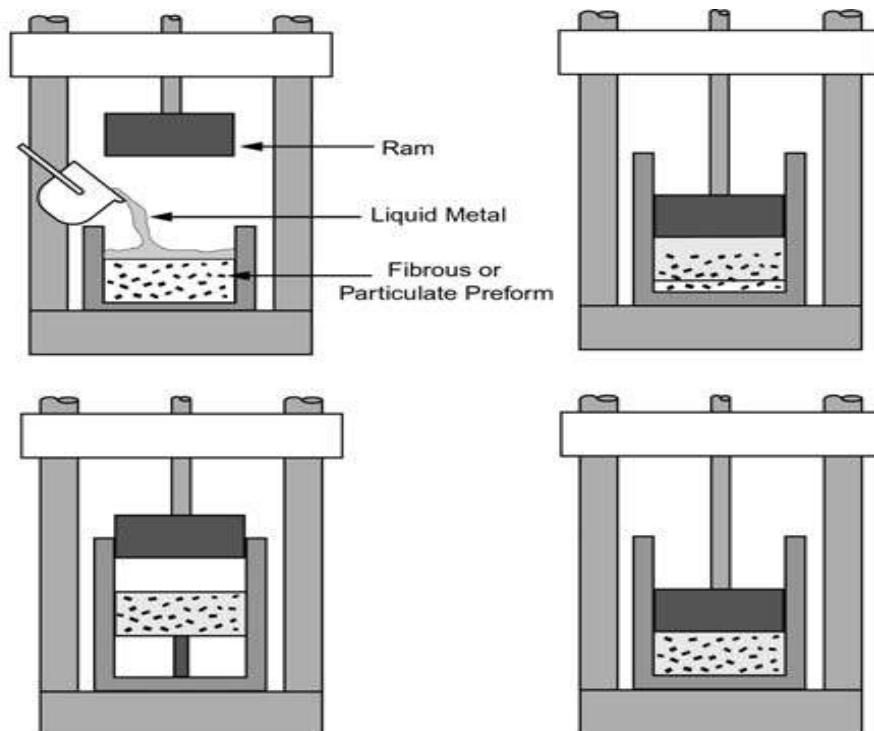


Fig. 1.11: Squeeze casting, infiltration setup

forms, such as pressurized infiltration and squeeze casting injections. A method of squeeze casting infiltration is shown in Fig. 1.11. The volume fraction that can be infiltrated can be determined by the size and nature of the preforms. Inhomogeneity and porosity are a concern in this kind of production method. The quality of preforms decides the infiltration and product characteristics, and a range of 8-75% reinforcement volume fraction can be attained. Alumina and silica-based mixture is used as a binder to retain its integrity and shape.

1.4.2.3 Spray deposition

In the spray deposition method, the composite is formed through the deposition of the heat matrix phase on the reinforcement through a spray. Spray deposition can be performed by two different techniques. As shown in Fig. 1.12, when a molten bath produces a droplet stream with the help of pressurized gas flow, it is called the Osprey process. In contrast, continuous feeding of the metal in cold form into a zone of high-speed heat injection is called thermal spray injection. The level of porosity in the composites of spray deposition is about 4-9%. It is applicable for processing particulate reinforced metal matrix composites, and the product is

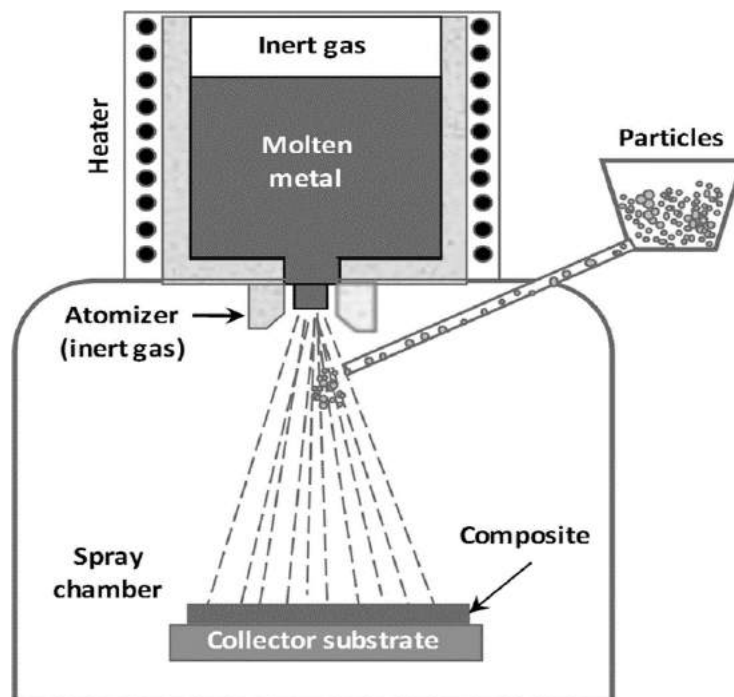


Fig. 1.12: Spray deposition

homogeneous with less porosity. In some specific cases, continuous fibre reinforced composites can also be manufactured through this process.

1.4.2.4 In-situ processing

Various processes, including liquid-liquid, liquid-gas, mixed salt reactions and liquid-solid, would fall under the category of in-situ processing. In these processes, refractory reinforcement can be fabricated in the metal matrix alloy matrix. For example, directional oxidation of metal (termed as DIMOX process) is a process where aluminium and magnesium alloy is placed on the top of the ceramic preform in a crucible. A gas mixture along with the alloy is heated along with the entire setup. A composite is formed when aluminium-magnesium alloy infiltrates the preform after melting. Another technique of in-situ processing is the XDTM process or Martin–Marietta's exothermic dispersion process. This process is also used for the development of aluminium matrix composites reinforced with TiB₂ particles. This technique can provide better flexibility in operations, and various parameters such as the size of particles, hardness of reinforcement, type of matrix material can be altered easily. Tic reinforced metal matrix

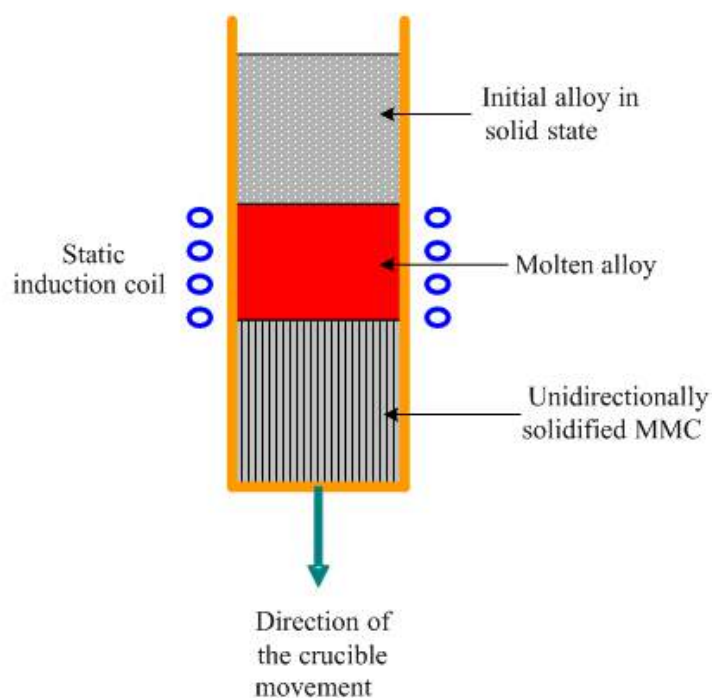


Fig. 1.13: In-situ Processing of composite in unidirectional solidification

composites can be manufactured using gas-liquid reaction. Aluminium/TiC_p composites are fabricated by infiltrating the bubbles of carbonaceous gas(CH₄, C₂H₆) into Al–Ti melt kept at elevated temperature. Various industries have adopted the in situ process, which fabricates the composites by utilizing mixed salt reaction processes. There are some restrictions associated with the in-situ processing, and it limits the composition and nature of the reinforcement phase. Also, there are few kinetic restrictions on the volume fraction, size and shape of the reinforcements under a given set of test conditions. An example of unidirectional solidification of in situ processing is shown in Fig. 1.13. Unidirectional solidification of in-situ processing is capable of producing high-end unidirectional composites with low porosity.

1.5 Properties of composites

The wide range of superior and tailor made properties can be attained for the different composites that increases the applicability of the composites.

1.5.1 Flexural strength

Composites have better strength to weight ratio, and therefore they can be a more suitable alternative from the parent materials. The composites have a high Young's modulus to density ratio and therefore have better flexural strength. The flexural strength can be directionally varied in laminates and fibre reinforced composites. Discrete particle metal matrix composites have a minimal directional variation in the flexural strength for composites with homogeneously distributed particles.

1.5.2 Wear Resistance

The reinforcements embedded in the matrix increase the wear resistance of the composite material. The grinding wheels are made of composites with a binder material that holds

abrasive particles in the matrix material and has high wear strength. Reinforcement such as boron carbide, silicon carbide, aluminium oxide and titanium carbide are frequently used to increase the wear resistance of the parent matrix material.

1.5.3 Impact Strength

The impact strength is one of the most important properties that a material used for defence application must possess. The high impact strength reduces the possibility of damage during collision and blast conditions. Recently developed fibre and particle reinforced composites are replacing the conventional materials for armour and protection equipment. Composites have given outstanding results of the ballistic test with velocity. Graphene and carbon nanotubes vastly increase the impact strength of composites and are highly suitable for energy absorption applications. [20]

1.5.4 Corrosion resistance

Spray deposition and other coating related techniques used for the development of composites are widely used to increase corrosion resistance. Poly 4-Vinylpyridine-co-butyl methacrylate and Reduced Graphene Oxide are the eco-friendly composite coating to make composites using Electrophoretic Deposition. It is essential that the coating should be uniform, homogeneous and there should be no porosity within the sample for attaining high corrosion resistance.

1.5.5 Lightweight

Conventional materials with high density have high mechanical strength, and low-density materials have low strength. Composites can attain high strength with relatively low density. Few specific types of polymer matrix composites display excellent strength characteristics for a relatively low density. Composites have wide applications in the domain of transportation,

space and aerospace industries because of this trait. Various automobile components such as drive shafts, brakes and chassis are preferred to be manufactured with composite materials.

1.5.6 Damping

Dealing with vibration is a significant issue in industries as continuously operating machinery is exposed to vibrations. The high level of vibrations can be limited only to a certain extent. Therefore, there is a high demand for materials with high damping properties in the present scenario. Since the composites have many imperfections in their microstructure and can absorb the energies, they are excellent in damping these vibrations. Therefore, composites possess good damping characteristics and are suitable for this kind of applications.

1.5.7 Temperature resistance

Among different composites, titanium matrix composites are best suited for high-temperature applications. The material used in thermal applications with high-temperature resistance should also have a low thermal coefficient. The components under high thermal load results in huge deformations, and the fixed ends are susceptible to massive stresses. Therefore, composites with high-temperature strength and a low coefficient of expansions are highly suitable for high-temperature applications.

1.6 Application of composites

The applicability of the material is a primary concern and it is important to study the market applications of the material. There is huge application scope for metal matrix composite due to their superior and tailor made characteristics. The composites can provide wide variety of attributes and therefore can fit into various kind of applications.

1.6.1 Transportation

The transportation industry includes automobile and railways application where fuel efficiency and weight carrying capacity are the leading factors. Nowadays, composites are commonly used in these applications since they provide tailorable properties. Few examples of the application of composites in transportation are as follows:

1.6.1.1 Braking and Clutch System

The braking and clutch systems require a high wear strength for the extended operations of the mechanisms since they are the friction elements. Therefore, composites are much efficient than their respective parent materials and provide better life and performance. Metal matrix composites are highly recommended for these applications since they are less weight, high strength and high-temperature resistant materials.

1.6.1.2 Driveshaft

Driveshafts are the rotating element in the automobile that transmits the power from the engine crankshaft to the gearbox to the differential gear mechanism and then to the wheels. These elements require high flexural strength and damping since they are prone to vibrations, jerks and shocks. Therefore, composites are in high demand for this kind of applications. Aluminium matrix composites with discrete reinforced composites are used to manufacture driveshafts for trucks and cars.

1.6.1.3 Engine Body

Various engine components such as piston, crankshaft, gudgeon pin, valves, and cylinder have been manufactured by replacing conventional material with composites. These components require a high strength /weight ratio for better efficiency. These components are also exposed to huge vibrations and thus material with better damping properties are required. The composite are suitable as they provide better damping properties as compared to the conventional material.

1.6.1.4 Automotive body parts

Automotive vehicle body parts must have a high impact strength and must have high shock absorption capacity. Moreover, the body should be lightweight and should act as a supercapacitor for attenuation. Carbon fibre-reinforced polymer matrix composites are suitable since they can create more free space in the underhood area.

1.6.2 Aerospace

Various challenges are faced by aerospace to attain profitability in the cut-throat competition. There is a continuous search of new kind of materials which can optimize the value of the component. The researchers find many solutions related to strength, weight and safety by replacing the parent material with composites.

1.6.2.1 Aircraft brakes

Carbon fibre, silicon carbide reinforced composites have a high coefficient of friction, resistance to environmental conditions and therefore used as aircraft brakes. High-temperature sections such as exhaust nozzle ceramic-matrix composites are used. MMCs with particulate reinforced composites are also used for the development of the aircraft brakes.

1.6.2.2 Aircraft Structure

The structure of the aircraft must withstand huge variation in pressure, vibration and temperature. Polymer and metal matrix composites are replacing the conventional aluminium base alloy. There are many examples of the utility of the MMCs for the manufacturing of the various components in aircraft structure.

1.6.2.3 Gas turbine

For gas turbines, woven ceramic matrix composites (CMC) can help in optimizing the coolant gas requirement. A substantial gain in the inlet combustor chamber can be achieved by using a multi-hole cooled ceramic matrix composite.

1.6.2.4 Aircraft seats and fabric

Aircraft seats and fabric should be soft, self-cleaning, photo-oxidized, anti-sticking, hydrophobic and comfortable in nature. Since multilayer polymeric/TiO₂ composites have these properties, it is used for the fabric of carpets and seats in aircraft.

1.6.3 Defence

Composites have wide application in the defence sector, such as in the naval system, arms and ammunition, military aircraft, land vehicle and body armour. Military aircraft used many components made of fibre-reinforced composites such as canopy fairing, leading-edge radome, and forward fuselage. The land vehicle armour is now preferred to be of metal matrix composite because of its high energy absorption/attenuation characteristics. The metal matrix composite material also provide better strength to weight ratio and therefore are suitable for defence applications.

1.6.4 Biomedical

Composites are utilized in various biomedical applications such as skin grafting, orthopaedic, haemodialysis and angiography. Skin grafting requires a porous material for wound healing. A chiton based composite is a biodegradable material that is suitable and frequently used for skin grafting. For orthopaedic applications, titanium is the best suitable material because of its mechanical properties, biocompatibility and ability to integrate with native bone. However, carbon nanotube-based composites have a massive potential in replacing titanium, as they have added advantage of absorption ability, spontaneous differentiation of osteoblastic and osseointegration. It has been observed that composite having cellulose acetate matrix with carbon nanotube and graphene oxide reinforcements have the highest protein retention. Therefore, it is applicable for tissue generation and haemodialysis.

1.7 Metal matrix composites for rotor applications

The rotor is an integral part of almost every mechanical system, and therefore it is mandatory to analyze its behaviour periodically and accurately. Catastrophic failures can occur due to malfunctioning of rotors, especially in the automobile and aerospace field. Dynamic analysis of composite rotors is an emissive field of research due to its practical importance. Several issues are associated with this analysis due to its complexity and increasing demand for reliable defect detection techniques. In order to achieve high fuel efficiency, a continuous effort has been made to reduce the weight of the overall transmission system. This need had forced researchers to envisage various composite materials. Within few decades, several efforts have been made for the development of 'composite rotors'. Various composite material applications to drive shafts and rotors have already been substantially explored and detailed in the literature. Composites show improved mechanical properties as compared to parent alloys. Therefore composites have evolved as a substitute to front-drive aero gas turbine engine's supercritical power turbine shaft. Other examples of the applications are an aircraft power take-off shaft, propeller shafts in small ships, transmission shafts, boring bars, and high-speed machine tool spindles.

Carbon Fiber Composites (CFCs) generally obscure Metal Matrix Composites (MMCs) when it comes to lightweight operations. However, MMCs possess several peculiar advantages with respect to other lightweight materials such as high-temperature stability, low-velocity impact resistance and better joining ability etc. These are the significant reasons that MMCs have been used by industries such as defence, nuclear fusion, oil and gas, space, aircraft, manufacturing, renewable energy and automotive parts. The major advantage of these composites is that tailorable properties can be achieved by altering the processing method, composition and processing parameters of MMCs. For rotor applications, two material properties are a matter

of concern. One of them is Specific Modulus (associated with whirling performance) that is the ratio of the Young's Modulus and the density. The second property of concern is the Shear Modulus (related to torque carrying capacity). Metal Matrix Composites provide access to reach a tailorable property as per requirement, and it is possible to attain higher values of specific modulus and shear modulus mentioned earlier.

1.8 Specific applications of metal matrix composites

Metal matrix composites possess suitable properties which make them an optimum solution for rotor applications. The application of MMCs in various fields of the industry has been reported in many research works of literature. Automobile and Aluminium Matrix Composite (AMC) driveshafts have been used in selected applications for several years [21]. *Rohtagi et al.*, [22] elaborated the potential applicability of MMCs in industry and provided a datasheet for various applications fields. Driveshafts with this configuration are been used because of high specific stiffness and fatigue strength. Other driveline components such as shift fork are also been manufactured of MMC material. Many manufacturers such as Duralcan, GKN, Toyota, GM and Nissan have used MMC material to develop various components with both static and dynamic application [23].

Discontinuously reinforced aluminium (DRA) MMCs driveshafts are used for many automobiles and light-duty trucks. A 6061Al/Al₂O₃ DRA driveshaft along with cylinder driveshafts manufactured by a stir casting method where molten metal is stirred for a particular time to mix reinforcements, and direct, seamless extrusion have various applications. [24-26]. The main reason is that it allows a longer length of operation for an equivalent diameter. MMCs possess a relatively higher value of specific stiffness than conventional aluminium or steel driveshafts, due to which they can perform for longer lengths. This eliminates the requirement for multiple driveshafts and the associated centre support structure in trucks and large

passenger vehicles. Aluminium composite driveshafts have been used in pickup trucks by various companies such as GMC Sonoma and Chevrolet S-10. Moreover, it was introduced as the rotor component for the Chevrolet Corvette and used in the 'Ford Police Interceptor' version of the Crown Victoria [25].

Some of the proven commercial applications of AMMCs are as given below:

- Brake rotors made from aluminium composites (AlSi7Mg+SiC particulates) for German high-speed train ICE-1 and ICE-2 developed by Knorr Bremse AG
- MMC continuous fibre reinforced pushrods produced by 3M for racing engines. These pushrods weigh 40% of steel
- MMC wires also developed by 3M for the core of an electrical conductor
- Pistons, brake rotors, callipers, liners and propeller shafts manufactured by Duraclan, Martin Marietta, GKN and Lanxide using Al-SiC particle composites
- Connecting rods of Nissan using Al-SiC whiskers composites
- Connecting rods of DuPont, Chrysler, and Piston rings of Toyota using Al- Al₂O₃ composite
- Pistons and connecting rods of Martin Marietta using Al-TiC particle composite
- Engine blocks of Honda using Al-Al₂O₃-carbon fibre hybrid composites
- Brake rotors of Lotus Elisse, Chrysler and Volkswagen using Al-SiC particle composites.

1.9 Discrete alumina reinforced aluminium 6061 composite shafts for rotor applications

1.9.1 Aluminium 6061

Material availability is one of the prominent factors for the selection procedure for the composite matrix for any application. Aluminium has a wide range of applications in the

industries and is one of the most abundant metals, and has a total of 8 wt. % (weight percentage) in the earth crust. Therefore, aluminium is suitable for selection as a matrix material for rotor applications. In addition to that, attributes such as better formability, high strength to weight ratio, flexural strength, durability and stability make it most suitable for engineering applications, specifically rotor applications.

Aluminium can be alloyed with various other elements such as zinc, Silica, magnesium, manganese and copper. The alloys of aluminium are designated differently and depend on the first number is based on the alloying element. The designation of the first number is shown in Table 1.1.

Table 1.1 Series of Wrought Aluminium alloy

Series number	Description
1st	Pure aluminium alloy
2nd	Aluminum and copper as a major alloying element
3rd	Aluminum and manganese as a major alloying element
4th	Aluminium and silica as a major alloying element
5th	Aluminum and magnesium as a major alloying element
6th	Aluminum, magnesium and silica as a major alloying element
7th	Aluminum and zinc as a major alloying element
8th	Other alloys

Metal matrix composites for rotor applications are generally manufactured by liquid processing method. In the liquid processing method, the wettability of the reinforcement into the molten metal matrix is one of the primary concerns. Magnesium and silica, due to their low surface tension properties, improve the wettability of the reinforcements. Therefore, the 6th series aluminium alloy is preferred as a matrix material for developing the metal matrix composite

rotor. Since aluminium 6061 has the best compatibility with the most common reinforcements, it is one of the best-suited matrix materials for rotor applications.

1.9.2 Alumina (Al₂O₃) as reinforcement

For a particular matrix material in composite, reinforcement selection is based on its compatibility and adaptability with the matrix. The suitable reinforcement for the various matrix material is shown in Table 1.2.

Table 1.2 Suitable Reinforcements for the metal matrix

Reinforcement	Metal matrix
Boron, fibre (including coated)	Titanium, Aluminium
Alumina particulate	Magnesium, Aluminium
Boron carbide particulate	Magnesium, Aluminium
Silicon carbide particulate	Magnesium, Aluminium
Silicon carbide whisker	Magnesium, Aluminium
Alumina fibre	Magnesium, Aluminium
Alumina-silica fibre	Aluminium
Silicon carbide fibre	Titanium, Aluminium
Graphite fibre	Aluminium, Magnesium, Copper

Aluminium is compatible with most of the reinforcements for the production of aluminium matrix composite. Silicon carbide and alumina are the most common reinforcements available in the market and are readily used in composite manufacturing. For aluminium alloy, silicon carbide is much more suitable than alumina since it has better wettability and produces more homogenous products. But it is not suitable for rotor application because it does not allow welding of rotors or shaft to the yoke since it produces Al₄C₃ embrittlements. Due to this

reason, alumina is preferred as a reinforcement material for the aluminium matrix composite rotor.

1.10 Characterization of metal matrix composite

1.10.1 Microstructure

The microstructure of the composite material can be analyzed on two different levels. The first level is for observing the grain structure, and the second one is for the observation of the particle distribution. The grain size can be observed with a magnification of 200X through an optical metallurgical microscope. An optical microscope works on the reflected light principle, where it utilizes transmitted illumination through a unique setup where light is reflected after travelling between the objective turret and head of the microscope. For further magnification up to a scale of 1000X, Scanning Electron Microscope (SEM) is used. This equipment generates images by using a focused beam of electrons for scanning the surface of the samples. When the high energy electrons collide with the atoms present in the sample, various signals are produced from which the information about the surface topology is attained. A secondary electron detector detects the secondary electrons emitted by the atoms due to the collision of the electron beam.

1.10.2 Tensile strength and elastic modulus

The elastic modulus and tensile strength of the composite can be determined on the Ultimate Testing Machine (UTM). Generally, the dimensions of the sample used in the testing should conform to ASTM E8M-04 standard. UTM applies a tensile force to the specimen, and it measures the strain developed in the composite and the amount of force required for the necking and breaking point.

1.10.3 Hardness

For hardness testing of the composites, Brinell hardness cum superficial testing is used, an indentation hardness test. A predefined force is applied to a sample by a spheroconical diamond indenter under specified conditions in this test.

1.10.4 Composition analysis and Residual Stress

The composition analysis of the material is essential to determine the presence of the reinforcement and the matrix material. Residual Stresses are developed in the metal matrix composites due to the mismatch in the coefficient of thermal expansion in composites. Residual stresses and composition analysis are performed by the X-Ray diffraction method. In this method, X-ray impinges on the sample, and the radiation due to the collision of the beam and the atoms of the composite material is analyzed.

1.11 Multi-scale modelling of metal matrix composite

1.11.1 Image analysis of microstructure

The SEM micrographs can provide a qualitative analysis of the particle distribution. But for estimating the properties of the composite, a quantitative analysis is required for the data generation. Quantitative analysis can be made possible by the method of image analysis. The image is analyzed by binarising the image into two parts and determining a particular threshold value.

1.11.2 Prediction of effective properties

For the prediction of metal matrix composite's effective properties, there are several theories proposed. Different theories justify the behaviour of composite rotors and can be utilized for the analysis of such components. These approaches are illustrated in a concise manner below.

1.11.2.1 The Generalized Method of cells (GMC)

It is a tool to determine the effective mechanical properties of the composite material by utilizing the properties of the parent materials using a micromechanical model. It is based on the assumption that this composite possesses a repetitive microstructure where discrete particles with a predefined size and shape are assumed to be distributed throughout the material in a uniform manner. A representative volume element (RVE) of a composite is identified as the smallest unit of the material, which could represent the volume throughout. Consecutively, macroscopic values or average values are derived by integrating individual component of microscopic stress and strain values by imposing the continuity of displacements and tractions at the interfaces between the matrix and reinforcement. Finally, by establishing the relationship between relative microscopic and macroscopic strains, overall macroscopic constitutive equations for the derivation of effective properties of these composite are generated. The overall elastic behaviour of the periodically assumed MMCs is predicted by these resulting three-dimensional micromechanical model [27]. A model proposed as the Mori-Tanaka model is readily used in industries to predict the composite material. Digimat is a dedicated tool developed by MSC software that uses this model to predict the composite properties.

1.11.2.2 The Equivalent Modulus Beam Theory (EMBT)

Effective material properties are obtained from micro-mechanical behaviour analysis of the composite rotor in this EMBT theory. Therefore, the composite rotor assumed in layers is substituted with an equivalent homogeneous shaft. The shaft bending and torsional behaviour are controlled by the effective moduli E_x and $G_{x\theta}$. Experimental Investigations by Zinberg and Symmonds [28], Bauchau [29], Zorzi and Giordano [30] were almost complementary to the values evaluated through EMBT. Bending stretching coupling effects and shear normal coupling effects are not accounted in typical beam theory. EMBT has a practical application

for the analysis of composite shafts, and it provides accurate results for configurations possessing symmetries.

1.11.2.3 The Modified EMBT

In EMBT, Classical Laminate Theory (CLT) is used to evaluate the effective in-plane and longitudinal shear moduli. Then Timoshenko beam theory utilizes these moduli to determine shaft natural frequencies. However, it has some limitations, such as it doesn't entertain stacking sequence for the prediction of equivalent longitudinal and in-plane shear moduli. Secondly, shear-normal, bending-stretching coupling and bending-twisting couplings are not included in EMBT formulation. Therefore in modified EMBT, Bresse-Timoshenko beam is introduced in which rotary inertia, gyroscopic effects and transverse shear deformation are considered. Also, this theory is generalized to incorporate shear-normal, bending-twisting and bending-stretching coupling effects. In order to overcome the limitations of the EMBT, Gubran developed modified EMBT. Also, Gubran and Gupta [31] provided derivations for modification in EMBT to incorporate the necessary modifications in order to overcome its limitations.

1.11.2.4 Simplified Homogenized Beam Theory (SHBT)

It is an alternative approach by Sino et al. [32], which exploits an energy formulation to evaluate the homogenized parameters of the beam, such as flexural as well as shear stiffness. It also simultaneously considers shear modulus, modulus of elasticity, the axial eccentricity of the shaft, specific damping capacity and the layer thickness of the shaft. By obtaining the solution of a boundary value problem, flexural warping can be determined, which is interpreted on the cross-section then the shear corrector factor is evaluated. Although, this formulation is simplified by inferring that the mechanical coupling effects, instigated by the non symmetrical stacking of layers, are negligible.

1.11.2.5 Layerwise Beam Theory (LBT)

The Layerwise Beam Theory preserves the layerwise constitution of the tubular shaft. It presumes that this composite shaft comprises of different layers throughout the thickness of the shaft wall, and each layer has different thickness and fibre orientations. At the interface of two layers, the continuity of displacement will be taken as it is assumed that there is perfect adhesion between plies. But, a discontinuity in slope or a sudden deviation in the slope within each ply to other can exist. Two different components of cylindrical coordinates can define deflection in the transverse direction of shaft cross-section, one is normal, and the other is circumferential displacements. Using displacement along the axis of the shaft because of the rotation of the cross-section across a neutral axis, a strain field is obtained.

1.12 Dynamic analysis of metal matrix composite

For metal matrix composite rotors, the system's dynamic response changes abruptly with the change of material. A multi-physical approach is required for the dynamic analysis of this kind of rotors. The dynamic response can be simulated through a computational approach and then can be validated experimentally. A dynamic physical system can be represented graphically through a multi-physics approach, called a bond graph. A system can be analyzed as a state-space representation through this approach, and the dynamic response can be obtained. The dynamic response can also be obtained experimentally through a data acquisition system and piezoelectric sensors. The frequency response function (FRF) can provide an insight into the dynamic nature of the component under observation.

1.13 Thesis scope

The present experimental study has been conducted to develop and characterize aluminium metal matrix composite rotors and analyze the dynamic behaviour of these rotors with different

composition. Various contemplated aspects were literature review, material selection (Al6061 as matrix material and alumina (Al_2O_3) as reinforcements) and synthesis of composites through stir casting technique. This research investigation was essentially concentrated on the mechanical behaviour of the different compositions of the composite rotor. The following section explains the contribution of the present research work.

1.14 Contribution of present work

The main objective of this experimental work is to develop a methodology for the fabrication, characterization and dynamic analysis of high-performance metal matrix composite rotors. The present study strongly rationalizes the rotor applications of synthesized aluminium matrix composites with maximum different weight percentages of alumina reinforcements with exceedingly intensified mechanical and rotodynamic attributes. Synthesized Al606/Al₂O₃ composites with their ameliorated traits may have an extensive spectrum of state-of-the-art applications, including automotive, high strength structures, thermally modifiable/ lightweight aerospace and defence applications. The organization of the thesis is explained in the forthcoming section.

1.15 Organization of Thesis

The thesis mainly consists of seven chapters and is organized as follows.

- ***First chapter*** comprises discussions on the background of composite materials, their classification, fabrication methods, characterization, dynamic analysis, scope of the thesis, contribution of present work and organization of the thesis.
- ***Second chapter*** presents an exhaustive literature review through assorted research articles spanning the distinctive research contributions in terms of different kinds of composite applications, processing techniques and characterization methods, computation of effective

properties and dynamic analysis. This chapter includes a brief explanation of various processing techniques for the synthesis of aluminium metal matrix composites. It discusses the outcomes of the literature review related to aluminium metal matrix composites. This chapter also includes the problem statement, research objectives of the present research work, and the methodology adopted to achieve these objectives.

- **Third chapter** presents the development and optimization of the development parameters of the metal matrix composite. The parameters are optimized for the quantitatively determined distribution index and area fraction of the composite. These values are extracted from the Scanning Electron Microscopy.
- **Fourth chapter** deals with the characterization of the metal matrix composites developed through the stir casting route, followed by the preparation of standard test specimens for various mechanical characterizations. It includes discussions on elemental analysis and microstructural studies of composites using various techniques such as XRD, EDS and SEM. This chapter also discusses the tensile strength and microhardness of the components.
- **Fifth chapter** provides an insight into the prediction of effective properties through computation and image analysis. The effective properties are predicted through the mean-field homogenization method and image analysis. These properties are experimentally validated through ASTM E1876 impact hammer vibration analysis.
- **Sixth chapter** presents the dynamic investigation of the composite rotor. The dynamic response of different compositions of the rotor is simulated through bond graph modelling.
- **Seventh chapter** summarizes the key findings of the present research work. It also discusses various future scopes related to the present experimental investigation.

This chapter encompasses research motivation and a detailed introduction of composites materials. It highlights the scope of the thesis, contribution of present research investigation and organization of the thesis. A review of the literature shall be excogitated in the next chapter.

Literature Review

2.1 Applications of metal matrix composite as rotor

With the advent of composite materials, industries have started focusing on the use of lighter weight materials with the same mechanical properties. Metal matrix composites have the edge over the parent metals for rotor applications, as it has a higher specific modulus, tensile strength and other mechanical properties. Aluminium /alumina MMCs have shown prominent growth in the composite material market because of their compatibility to the rotor systems.

Koczak et al., 2013 [21], provided a review on the applications of metal matrix composite rotors. They concluded that driveshafts in trucks and large passenger cars offer a particularly attractive application of (Discontinuously Reinforced Aluminium) DRA. Although the majority of automotive drive shafts are constructed from steel, aluminium driveshafts have been in use in selected applications for a number of years.

Miracle et al., 2005 [33], concluded that DRA driveshafts are used for automobiles and light-duty trucks. As with the cylinder liners, system-level benefits aided the decision to apply a 6061Al/Al₂O₃ DRA produced by stir casting and direct, seamless extrusion. The higher specific stiffness relative to steel or Al driveshafts allows a longer length at equivalent diameter to be used. This eliminates the need for two driveshafts and the associated centre support structure in trucks and large passenger vehicles. DRA driveshafts have been used in the Chevrolet S-10 and GMC Sonoma pickup trucks, was introduced as standard equipment for the

Chevrolet Corvette in 1997 and has been used in the 'Ford Police Interceptor' version of the Crown Victoria.

Nturanabo et al., 2019 [34], reviewed the novel applications of the aluminium matrix composites. The research focused on the applications related to the rotary components of industrial machinery. It was concluded that the use of Aluminium matrix composites for rotary applications results in increased efficiency and better critical speed handling.

2.2 Development of metal matrix composite material

Metal matrix composites can be manufactured by various methods from liquid and semi solid-state of matrix mixed with solid reinforcement particles. There are various methods such as powder metallurgy, diffusion bonding, infiltration, stir casting and spray forming to manufacture MMC as per requirements. Stir casting is one of the most inexpensive methods which has been used for the fabrication of metal matrix composites. For complicated and extensive size design of metal matrix composites, stir casting is very convenient and useful. The quantitative distribution index and area fraction may be very useful in optimising the process parameters and can provide more authentic and reliable results as compared to the qualitative analysis. There are various methods used for parametric optimisation having multivariant parameters. Box-Behnken designs (BBD) are one of rotatable or nearly rotatable second-order designs based on three-level incomplete factorial designs. BBD is one of the main types of response surface design, the other being central composite design. The BBD design requires a smaller number of runs as compared to central composite design. The Box-Behnken design operates within the range of parameters and does not generate experimentation points beyond the range of parameters like the central composite design. BBD is suitable for the designs where the range of operations are constrained by manufacturing conditions.

Ekinci et al., 2014 [35], produced aluminium metal matrix composites (Al-MMCs) reinforced with aluminium oxide (Al_2O_3) (5, 10, 15 wt. %) using the powder metallurgy (PM) process. The microstructures were investigated by optical microscopy and scanning electron microscopy (SEM). More homogeneous dispersion of Al_2O_3 in the Al matrix and improved mechanical properties of the composites were achieved with increased milling time. More homogeneous mixtures are obtained using a vertical high-energy attritor for the milling process. Transverse rupture strength of the sample milled for up to 3 h increased, and hardness of composite samples also increased with increasing milling time. Optimum material parameters were observed in samples milled for 3 h, which was long enough for samples to achieve a steady-state.

Sarina et al., 2012 [36], stated that the wettability of pure aluminum on filter materials and on inclusions is believed to be an important factor affecting the filtration of aluminium. To describe the wetting behaviour of the Al on ceramic at lower temperatures used in filtration and casting aluminium, a semi-empirical calculation was employed. It indicated that aluminum does not wet alumina or graphite (or Al_4C_3) around the casting temperature but wets SiC at this temperature. Thus a priming height is required for aluminum to infiltrate an alumina filter. Increasing temperature can also improve the wettability of Al on ceramic. An improved wetting of aluminum on ceramics with temperature is an advantage in getting molten metal to infiltrate alumina. In priming filters, it is necessary to have a metal height above the filter or to increase the temperature. However, filtration may proceed at a lower temperature once the metal has entered the filter.

Va et al., 2014 [37], synthesized metal matrix composite using 6061Al as matrix material reinforced with ceramic Al_2O_3 particulates using liquid metallurgy route in particular stir casting technique. The addition level of reinforcement is being varied from 6 - 12wt. % in steps of 3wt. %. For each composite, reinforcement particles were preheated to a temperature

of 200°C and then dispersed in steps of three into the vortex of molten Al6061 alloy to improve wettability and distribution. The optical micrographs of composites produced by the stir casting method show a reasonably uniform distribution of Al₂O₃ particulates in the 6061Al metal matrix. The microstructure of the composites contained the primary D-Al dendrites and eutectic silicon. In contrast, Al₂O₃ particles were separated at interdendritic regions and in the eutectic silicon. The hardness of the prepared composites increases with increasing wt. % of Al₂O₃ particulates and strength of prepared composites, both tensile and yield was higher in case of composites, while ductility of composites was less when compared to as-cast 6061Al. Further, with increasing wt. % of Al₂O₃, the tensile strength shows an increasing trend. Maximum weight loss was observed in as-cast 6061Al alloy, and minimum weight loss was observed in 6061Al+12% Al₂O₃ composites at a constant load of 19.62 N and speed of 300 rpm, and higher wear rate was observed in as-cast 6061Al alloy when compared to 6061Al- Al₂O₃ composites at a constant load of 19.62N and speed of 300 rpm.

Mazaherya et al., 2009 [38], introduced a new method in stir casting to fabricate nano-Al₂O₃ particulate reinforced aluminum composites and avoid agglomeration and segregation of particles. Different volume fractions of nano-alumina particles were incorporated into the A356 aluminum alloy by a mechanical stirrer and then cylindrical specimens were cast and tested. The microstructural characterization of the composite samples showed uniform distribution of reinforcement, grain refinement of aluminum matrix, and presence of minimal porosity. In general, nano-sized Al₂O₃ particles are incorporated into aluminum matrix with the help of micro-Al particles mixing and under the processing conditions of stir casting used in this study. SEM micrographs indicate that nano- Al₂O₃ particles are homogeneously dispersed throughout the composite samples. There are also a few agglomerated particles. The grain size measurements show that the grain size of aluminum composite is smaller than that of monolithic aluminum.

Kanga et al., 2004 [39], depicted that the hardness and tensile behaviors of aluminum matrix composites reinforced with nanometric Al_2O_3 particulate have increased with the volume fraction of the reinforcement. Above 4 vol. % of Al_2O_3 , however, the strengthening effect levelled off because of the clustering of Al_2O_3 . The primary strengthening mechanism was the Orowan strengthening of effective nano- Al_2O_3 particles evenly distributed in the matrix.

Khorshid et al., 2010 [40], prepared aluminum matrix composites reinforced by two sizes of alumina particles (35 nm and 0.3 μm) by wet attrition milling and hot forward extrusion processes. The effect of the ratio of the nano- to submicron-sized particles (2:8, 3:7, 4:6, 5:5, and 6:4 in weight percent) on mechanical properties of the composites is evaluated by micro-hardness and tensile tests. It was found that by increasing the nanoparticle content, the hardness and strength of the composites first increase and then decrease when the amount of the nanoparticle exceeds 4 wt.%. The tensile fracture surfaces are also observed by scanning electron microscopy.

Mazen et al., 1998 [41], have studied the advantages of alumina composites and have manufactured metal matrix composites (MMC) using hot pressing followed by hot extrusion of aluminium (Al) powder reinforced by alumina (Al_2O_3) particles. Different properties were tested of the specimen obtained and compared with the simple metals. Under tensile as well as compressive loads, a strength improvement of 64 to 100% compared to the matrix material strength was obtained. Such strength improvement was attributed to the formation of fine subgrain structure as revealed by the SEM fractographs. The percent elongation to fracture ranged from 20 to 30%, which indicates good ductility as compared to the ductility of MMC manufactured by other techniques. Optical as well as scanning electron microscopy (SEM) examinations were used for characterization of the material microstructure and fracture behaviour. Porosity retained in the microstructure was very limited in the case of pure

aluminium billets. The SEM revealed the formation of a complex fine subgrain structure. Such a polygon zed structure is a major source of strengthening. SEM fractographs revealed that the main fracture mechanism in Al- Al_2O_3 MMC is the ductile mode of void initiation, growth, and coalescence. Voids initiated at Al- Al_2O_3 interfacial sites or the porosity retained in the aluminium matrix.

Park et al., 2001 [42], have studied that the mechanical properties of metal matrix composites (MMCs) are critical to their potential application as structural materials. A systematic examination of the effect of particulate volume fraction on the mechanical properties of an Al_2O_3 -Al MMC has been undertaken. The material used was powder metallurgy processed Al 6061 matrix alloy reinforced with MICRAL-20TM, a polycrystalline microsphere reinforcement consisting of a mixture of alumina and mullite. The volume fraction of the reinforcement was varied systematically from 5 to 30% in 5% intervals. The powder metallurgy composites were extruded then heat treated to the T6 condition. Extruded liquid metallurgy processed Al Alloy 6061 was used to establish the properties of the unreinforced material. The main purpose for producing metal matrix composites (MMCs) is to achieve light materials with high specific strength and stiffness. Of special interest in this regard are particulate reinforced metal matrix composites (PRMMCs), which possess several additional advantages. The composites had higher elastic module than the unreinforced alloy. The elastic modulus increased as particle volume fraction was increased but at a progressively decreasing rate. The decrease in the rate of stiffening with increasing particle volume fraction is attributed to an increase in the number of fractured particles present in the composites. The composites had better tensile and yield strengths than the unreinforced alloy. However, there was no significant change in strength as the particle volume fraction changed.

Daoud et al., 2003 [43], have studied that Al/Mg alloy matrix composites reinforced with different percentages of Al_2O_3 (60 μm) or SiC (90 μm) particulates were prepared by the

vortex method. The composites were then subjected to hot or cold rolling with different reduction ratios. The microstructures of the rolled composites revealed that the matrix grains moved around the particulate causing deformation. By continuing deformation, the particulates rearranged themselves in the matrix, leading to lensoid distortion. It was found that the addition of Al_2O_3 or SiC particulates increased the 0.2% proof stress and reduced both the tensile strength and ductility, compared with the monolithic alloy. Scanning electron microscopy (SEM) fractographic examinations showed that the composites reinforced with Al_2O_3 particulates failed through particulate fracture and matrix ligament rupture. However, the failure of the composites reinforced with SiC particulates was through particulate decohesion, followed by ductile failure of the matrix. Abrasive wear results showed that the wear rate of the Al/Mg alloy decreased with the addition of SiC particulates. However, increasing the volume fraction of SiC particulates did not have a prominent effect on the wear rate. The composites reinforced with Al_2O_3 particulates exhibited a higher wear rate than that of the unreinforced alloy. Furthermore, addition of both SiC and Al_2O_3 particulates into the Al/Mg matrix alloy did not significantly improve the wear resistance. For all the composites studied in this work, hot or cold rolling has marginal effect on the wear properties.

Saiza et al., 2003 [44], have demonstrated that the wetting behaviour and strength at aluminium/alumina interfaces is an active subject of research. Al/alumina applications include ceramic-metal composites and several applications for electronic industries. They found that in a solid-state joining, the strength of the joint increases with increasing joining temperature, whereas, in a liquid-state joining, the strength of the joint gradually decreases with increasing temperature due to the formation of unbounded areas. The highest strength reached 400 MPa when the interface was formed around the melting temperature of aluminium. An aluminium layer close to the interface became a single crystal when it was bonded to a sapphire. The combination of alumina and aluminium is well known and has many applications. For instance,

alumina has been used in the electronic industry for many years as a ceramic insulator, whereas aluminium is one of the best electrodes, having good electric conductivity, second only to copper.

Aqida et al., 2004 [45], porosity in cast metal matrix composite (MMC) have been known as a defect affecting the enhancement of strength, particularly in particle-reinforced MMC. Among the causes of porosity formation is air bubbles entering the melt matrix material, water vapour on the surfaces of the particles, gas entrapment during the mixing process, the evolution of hydrogen, and shrinkage during solidification. Many studies had revealed that casting parameters are the main factors affecting porosity formation. Optimum properties of cast MMC are attained with least porosity content. Generally, increasing content of porosity will decrease the mechanical properties of MMC such as tensile strength, Young's modulus, Poisson's ratio, and damping capacity. The presence of porosity decreased the mechanical properties of cast MMC as the failure process is initiated from the voids formed. Porosity formation is largely caused by gas entrapment during vigorous stirring, air bubbles entering the slurry either independently or as an air envelope to the reinforcement particles, water vapour on the surface of the particles, hydrogen evolution, shrinkage during solidification, and volume fraction of reinforcement material in MMC. The presence of porosity, consequently, decreases most of the mechanical properties of cast MMCs. Failures initiated from the pores within the matrix material, particle fracture and reinforcement-matrix interface are due to voids coalescence, reduction of ductility, and reduced MMC cross-section.

Meguid et al., 2004 [46], have studied that the tensile debonding and shear properties of composite interfaces reinforced by two different homogeneously dispersed nano fillers, carbon nanotubes and alumina nanopowder, are investigated. The composite adherends used are made of carbon fibre/epoxy laminate and aluminium alloy 6061-T6. The results reveal that varying the weight percentage of the nano fillers into the epoxy matrix adhesive favourably

influences the debonding and shear characteristics of the interface. The results also indicate that increasing the amount of the nano fillers beyond a certain weight fraction of the adhesive reduces the interface strength. SEM and TEM images of the fillers are presented and used in support of a proposed strengthening/weakening mechanism(s). The attention of the study was focused on the determination of the influence of the homogeneous dispersion of nano fillers in a special epoxy adhesive for the purpose of increasing its interfacial strength and properties. The work concentrated on the experimental determination of the tensile and shears properties of the nano-reinforced interface. The results reveal that at a given weight (volume) percent, the presence of nanoparticles plays a major role in determining the strength of the interface. It was also shown that dependence of the tensile and shear properties of nano-reinforced interface to the large surface area and the consequent interlocking of the nanofillers with the epoxy adhesive.

Lu et al., 2005 [47], have shown the improved ductility and thermal conductivity of Al_2O_3 ceramics by using wet chemical coating method to prepare $\alpha\text{-Al}_2\text{O}_3$ coating Al nano-composites powders. $\alpha\text{-Al}_2\text{O}_3$ -coated Al particles were synthesized by calcining Al $(\text{OH})_3$ gel coating on nano-size Al particles because of these processing nano-size Al shows high yield strength and high breaking strength, which are 5–6 times higher than that of coarse-grain. The advantage of the Al_2O_3 - coating Al powder is that a fine transition layer may be formed between Al and Al_2O_3 , which can be improved the bonding between Al and Al_2O_3 .

Razavi et al., 2007 [48], have demonstrated that densification response of aluminium powder reinforced with 5 vol.% nanometric alumina particles(35 nm) during uniaxial compaction in a rigid die. The composite powder was prepared by blending and mechanical milling procedures. To determine the effect of the reinforcement nanoparticles on the compressibility of aluminium powder, monolithic Al powder, i.e. without the addition of alumina, was also examined. It was shown that at the early stage of compaction when the

rearrangement of particles is the dominant mechanism of the densification, the disintegration of the nanoparticle clusters and agglomerates under the applied load contributes in the densification of the composite powder prepared by the blending method. As the compaction pressure increases, however, the load partitioning effect of the nanoparticles decreases the densification rate of the powder mixture, resulting in a lower density compared to the monolithic aluminium. It was also shown that reinforced aluminium powders. Morphological changes of the particles upon milling increase the contribution of particle rearrangement in densification whilst the plastic deformation mechanism is significantly retarded due to the work hardening effect of the milling process. Meanwhile, the distribution of alumina nanoparticles is improved by mechanical milling, which in fact, affects the compressibility of the composite powder.

Durai et al., 2007 [49], have revealed that nanocrystalline materials have a high potential for use in structural applications in which enhanced mechanical characteristics are required. Al-Zn/ Al₂O₃ and Al-Zn-Cu/ Al₂O₃ have been prepared via reaction sintering of partially reacted oxide mixtures derived from a high-energy ball milling process. The sintered samples have been characterized by XRD. Pin on disc type apparatus has been used for determining the wear rate. It is proposed in this study that the wear resistance of the milled composites is better than that of the unmilled composites since Al₂O₃ particle size plays the main role in bearing the external load, and there is a good interfacial cohesion between Al₂O₃ particles and the matrix. On the basis of microscopic observations and analysis of the wear surface a change in mode of wear from mild to severe has been proposed at different loads. Mechanical milling process causes a uniform distribution of the dispersed second phase in the matrix and lowers the inter-particle distance. Milled and then sintered composites have better hardness and wear resistance than the conventional (unmilled but sintered) composites. The

wear rate decreases with the sliding distance and attains a stable value after some time for both the composites, and this is presumably owing to the subsurface hardening.

Zhang et al., 2008 [50], have measured the wear resistances of alumina, alumina/silicon carbide composite and alumina/mullite composite by abrasive wear. And they studied the influence of fracture mode and worn surface pullout on wear resistance. The results are as follows: the main wear mechanisms of alumina and alumina/silicon carbide were fracture wear and plastic wear, respectively, and for alumina/mullite composite, fracture wear and plastic wear mechanisms worked together. The wear resistance of the alumina/silicon carbide composite and the alumina/mullite composite was better by a factor of 1 to 3 than that of the monolithic alumina. There were two main reasons for the better wear resistance, i.e., the improved mechanical properties and the more smooth worn surfaces. However, the primary reason was the reduction of area fraction of pull out on the worn surfaces induced by fracture mode transition.

Mula et al., 2009 [51], have investigated the structure of an ultrasonically cast nanocomposite of Al with 2 wt. % nano-sized Al_2O_3 (average size ~10 nm) dispersoids showed that the nano-composite was consisting of nearly continuous nano-alumina dispersed zones (NDZs) in the vicinity of the grain boundaries encapsulating Al_2O_3 depleted zones (ADZs). And they also revealed that nearly 92% increase in the hardness and 57% increase in the tensile yield strength were obtained in the present nanocomposite, as compared to those of the commercially pure Al, cast by the non-contact ultrasonic casting method. These improvements in the hardness and tensile strength were due to the reinforcement by only 1.4 vol. % nano-sized Al_2O_3 dispersoids in the Al matrix.

Mazaherya et al., 2009 [52], have investigated the effects of nano- Al_2O_3 particle content on the mechanical properties of the composites. For manufacturing the MMCs, 0.75, 1.5, 2.5, 3.5 and 5 vol. % Al_2O_3 particles were used. The required amount of Al_2O_3 was

calculated according to the ratio of Al/ Al₂O₃. The metal matrix composites have been produced by using a vortex method. Based on experiments, it was revealed that the presence of nano-Al₂O₃ reinforcement led to significant improvement in hardness, 0.2% yield strength, UTS and ductility. This combination of enhancement in UTS and ductility exhibited by nano- Al₂O₃ reinforced aluminium is due to uniform distribution of reinforcement and grain refinement of aluminium matrix.

Reddy et al., 2010 [53], have revealed that the yield strength and fracture strength increase with increase in volume fraction of Al₂O₃, whereas ductility of 6063/Al₂O₃ composites decreases. For this purpose dip coating slurries were prepared by adding the refractory filler to the liquid binder using sufficient agitation to breakup agglomerates and thoroughly wet and disperse the filler. Colloidal silica binder and alumina filler (particles of size 45 nm) were used to prepare dip-coating slurring. Prior to the machining of composite samples, a solution treatment was applied at 550°C for 15min quenched in cold water, and aged at 150°C for 100 hours.

Mazahery et. al., 2013 [54], incorporated 0.75, 1.5, 2.5, 3.5, and 5 vol. % of alumina nanoparticles into the A356 aluminium alloy by a mechanical stirrer and then, cylindrical specimens at 800°C and 900°C were casted. A uniform distribution of reinforcement, grain refinement of aluminium matrix, and presence of the minimal porosity were observed by microstructural characterization of the composite samples. Characterization of mechanical properties revealed that the presence of nanoparticles significantly increased compressive and tensile flow stress at both casting temperatures. The highest compressive flow stress was obtained by 2.5 vol. % of Al₂O₃ nanoparticles.

Ezatpour et al., 2013 [55], used a novel two-step mixing method, including injection of particles into the melt by inert gas and stirring to prepare aluminum matrix composites (AMCs) reinforced with Al₂O₃ particles. Different mass fractions of micro alumina particles were

injected into the melt under a stirring speed of 300 r/min. Then the samples were extruded with ratios of 1.77 or 1.56. The microstructure observation showed that the application of the injection and extrusion processes led to a uniform distribution of particles in the matrix. The density measurements showed that the porosity in the composites increased with increasing the mass fraction of Al_2O_3 and stirring speed and decreased by extrusion process. Hardness, yield and ultimate tensile strengths of the extruded composites increased with increasing the particle mass fraction to 7%, while for the composites without extrusion, they increased with particle mass fraction to 5%.

Soltani et al., 2017 [56], reviewed the stir casting method and stated that stir casting is a simple, flexible and low-cost method that is generally used for the fabrication of AMCs. The adaptability of this method with the conventional foundry method makes it an economical and viable method for manufacturing the metal matrix composites.

Pazhouhanfar et al., 2018 [57], observed that wettability and homogeneity of the solid reinforcement are essential factors that affect the mechanical properties of the stir casted products. The parameters such as the depth of the stirrer in molten metal, speed of the stirrer, blade angle, stirring time and preheating of reinforcement, etc. were optimized to achieve MMCs with better properties. These parameters affect the homogeneity, porosity, and distribution of the particles. Therefore, it is crucial to optimize these parameters in order to achieve the desired targets.

Chauhan et al., 2017 [58] illustrated the improvement of mechanical properties of Al 6061/ (Al_2O_3 and fly-ash), hybrid metal matrix composite using aluminium alloy Al 6061 as a matrix and alumina, fly-ash as a reinforcing material prepared by stir casting technique.

Ahmed et al., 2019 [59] investigated the detailed characterization such as tensile strength, hardness, fatigue, creep, corrosion behaviour, and wear resistance of the stir cast AMCs reinforced with nanocomposites.

Pitchayapillai et al., 2016 [60] evaluated the mechanical behaviour, tribological behaviour, and the machinability behaviour of the Al 6061/Al₂O₃/MoS₂ hybrid composite fabricated using stir casting process.

Haslam et al., 2013 [61] presented a new technique and index to quantify dispersion of CNTs in a composite material. The technique was partially based on a quadrat method, and takes into account the dispersion and agglomerate size distribution of the CNTs. This index has been benchmarked against the ASTM index using computer generated images and images experimentally obtained from thirty CNT composite material specimens with different CNT loading rates up to twenty volume percent. The new index has been more versatile and reliable than the ASTM index. They also stated that qualitative methods do not assist in providing numerical and objective oriented results and suffer from subjective judgment that can be utilised to compare the dispersion of reinforcements consistently. Therefore, quantitative measurement of dispersion is essential for optimising the process parameters in order to attain better results.

Yazdanbakhsh et al., 2011 [62] discussed the previously proposed methods for quantifying dispersion are reviewed and their applications and possible shortcomings. In the second part, a novel definition for dispersion based on the thermodynamic concept of work; dispersion is measured based on the amount of work required to translate inclusions so they form the state of maximum uniformity was proposed. The method quantifies dispersion with a single parameter. Although multiple parameter methods can provide more information about the spatial distribution of inclusions, the proposed method is particularly useful when comparing overall dispersion quality of different domains. As an example, the dispersion of carbon nanotubes in an Al coating was quantified to demonstrate the robustness and practicality of the novel dispersion quantification method.

Slipenyuk et al., 2004 [63] investigated the effect of particle size ratio (PSR) on the reinforcement spatial distribution, fabricability, and resulting mechanical properties of a P/M processed AlCuMn/SiC/15_p composite. It was concluded that matrix to reinforcement particle size ratio (PSR) is the main factor governing the homogeneity of the reinforcement particle distribution in composites manufactured by the powder metallurgy route. To improve the homogeneity of the distribution, reinforcements with larger average particle size should be used. At the same time, increasing the reinforcement particle size leads to worsening of the mechanical properties due to lower work hardening and higher damage accumulation rates. It is therefore important to optimize the microstructure somewhere in between a smaller reinforcement particle size and a more homogeneous spatial distribution. It was shown that increasing the PSR results in a less-uniform reinforcement distribution, which in turn leads to a decrease in the material fabricability and a general worsening of the mechanical properties. A close to linear dependence of the mechanical properties (yield stress, UTS, elongation before fracture, Young's modulus) on PSR was found. Tensile elongation shows the highest sensitivity to the worsening of the homogeneity of the reinforcement spatial distribution caused by increasing the PSR. The effect of microstructural homogeneity on the relative change of mechanical properties does not seem to depend on matrix alloy plasticity.

Jahedi et al., 2015 [64] synthesized the metal-matrix composites of commercially pure copper (Cu) and silicon carbide (SiC) by standard high-pressure torsion (HPT) and novel high-pressure-double-torsion (HPDT) processes of severe plastic deformation (SPD). Based on detailed microstructural examinations, they quantified the parameter and found that significant homogeneity of fine particle distribution as well as weakness of crystallographic texture can be obtained in the composites fabricated using these processes. The most homogeneous particle distribution is obtained in the material processed under HPDT, which imposes the highest strain levels. Crystallographic texture in the composite is found to be weaker than in monolithic Cu

processed under the same processing conditions. The randomization of texture in the composites is linked to the homogenization of the particle distribution.

Luo et al., 2008 [65] performed quantitative measurements of the filler dispersion degree of carbon nanofiber (CNF) and nanotube (CNT) reinforced polymer nanocomposites have been made by transmission electron microscopy. Samples were prepared by either high-shear mixing or twin-screw extrusion processing. It was found that the filler dispersion degree was largely influenced by the filler size. As the filler dimension became smaller, the dispersion parameter D_{index} largely decreased as quantified, which demonstrated the challenges associated with improving the dispersion of smaller fillers. A method to quantitatively compare the dispersion degrees of CNF/CNT polymer nanocomposites was provided.

Yakaboğlu et al., 2017 [66] developed a microstructural image analysis method with a new distribution index for quantifying the degree of distribution in composite materials. The free-path spacing between particles was measured to calculate the distribution D_{index} based on the coefficient of variation. The proposed method was applied to six digitally created reference patterns as representative binary composite microstructures and three actual ceramic-matrix composites, respectively. It was found that the D_{index} increased from 0.00 to 0.67 depending on the degree of distribution or homogeneity level based on the reference patterns. The homogeneity levels for the binary composites are then classified from a perfect (maximum) to very low level (minimum) based on increasing D_{index} values, where a high D_{index} presents a poorer distribution. The results obtained for reference patterns and metal silicide-refractory oxide composite microstructures indicated that the proposed method is a useful tool to quantify the degree of distribution with high accuracy, and can be efficiently used for different types of composite microstructures.

Ferreira et al., 2007 [67] described the fundamentals, advantages and limitations of the Box-Behnken design (BBD) for the optimization of analytical methods. A comparison between

this design and composite central, three-level full factorial and Doehlert designs was also established. A detailed study on factors and responses involved during the optimization of analytical systems was also presented. Functions developed for calculation of multiple responses were discussed, including the desirability function. Concept and evaluation of robustness of analytical methods were also discussed. Finally, descriptions of applications of this technique for optimization of analytical methods were presented.

Gopalkrishnan et al., 2012 [68] adopted BBD design for the prediction of wear rate for titanium oxide reinforced aluminium composites. Al-TiC_p castings with different volume fraction of TiC were produced in an argon atmosphere by an enhanced stir casting method. Specific strength of the composite has increased with higher % of TiC addition. Dry sliding wear behaviour of AMC was analysed with the help of a pin on disc wear and friction monitor. The present analyses reveal the improved specific strength as well as wear resistance.

Kumar et al., 2019 [69] also used BBD technique for process optimisation of stir casting to enhance the effect of particulates in composites. The effects of SiC, Al₂O₃, and ZrO₂ particles on the characteristics of Al/SiC, Al/Al₂O₃, and Al/ZrO₂ metal matrix composites (MMCs) were studied in the research work. The comparison of machining characteristics was done to analyze the behavior of various reinforced particles with the variation of laser machining variables. The output characteristics such as dross height and kerf deviation have been investigated and compared with each MMCs. SEM and XRD were used for the investigation of morphological changes in the structure and agglomeration of reinforced particles. The crack and recast layer formation were examined in the specimens of higher quantity of reinforced particles. It was observed that the MMC material reinforced with SiC particles has shown different behavior as compared to other MMC materials.

2.3 Characterisation of metal matrix composite material

Ravi et al., 2015 [70] observed that tensile strength is increased by increasing the percentage of reinforcement particles in the composite and it happens due to better interfacial bonding between the matrix and reinforcement. They found enhanced tensile strength of Al metal matrix from 117 MPa to 145 MPa. It was also observed that the hardness value was increased by increasing the wt% of reinforcement particle in the composite and they microhardness increased from 62 HV to 68 HV with incremental weight percentages.

Pradhan et al., 2016 [71] concluded that composite developed by stir casting contains higher hardness and greater tensile strength without much loss of ductility. It was also found that in the extruded composite the yield and ultimate tensile strength of the composite increases with Al₂O₃ content increasing because of increase in load stress.

Tanaka et al., 2019 [72] reviewed state of the art of the $\cos\alpha$ method. The concluded that X-ray stress measurement is widely used as one of the most powerful nondestructive tools to measure residual stresses in polycrystalline solids. In most cases, the $\sin^2\psi$ method has been used to determine the stress. In recent years, however, the $\cos\alpha$ method has attracted engineers as a new method to measure the stress using two dimensional detectors, such as imaging plates. For biaxial stress cases, the $\cos\alpha$ method utilizes the whole Debye-Scherrer ring recorded on a two dimensional detector taken by single exposure of X-rays, and normal and shear stresses are determined simultaneously. The accuracy of the stress measurement of the $\cos\alpha$ method has been confirmed to be equivalent to that of the $\sin^2\psi$ method for various metals. The simple optical system of the $\cos\alpha$ method makes stress analyzers smaller, lighter and more convenient to use for on-site or field measurements. A recent portable stress analyzer adopting the $\cos\alpha$ method shortens the measurement time to 60 s. The method has been further developed to analyze triaxial residual stresses. Various advantages of the $\cos\alpha$ method are highlighted in

comparison with the other methods of X-ray stress determination. Applications of the $\cos\alpha$ method to machines and engineering structures are presented, together with future perspectives of the method.

Noyan et al., 1987 [73] observed that residual stresses are introduced into the material during manufacturing due to various factors. The intensity of these residual stresses may act as an essential factor in the performance of the component. Large values of residual stresses can lead to plastic deformation and local yielding, both on a macroscopic and microscopic level.

Akiniwa et al., 2008 [74] observed that tensile residual stresses may cause quench cracking, fatigue failure and stress corrosion cracking. Although, all type of residual stresses does not hurt the performance of components. For example, fatigue strength and the resistance to corrosion cracking increases when compressive residual stresses are induced on the surface of a component.

Wang et al., 2015 [75] stated that a common non-destructive technique used to determine the residual stresses is X-ray diffraction (XRD). Recently, a two-dimensional (2D) X-ray detector has been available to allow the collection of a large part of the Debye–Scherrer Ring (DSR) for the stress calculation.

Wang et al., 2018 [76] concluded that the full 2D detector technology is among the upcoming technology for the evaluation and analysis of residual stress through portable X-ray residual stress equipment. This technology is reliable and thus well suited for various industrial test data such as in pipelines, driveshafts, bridges, high-speed trains, automobiles.

Chatterjee et al., 2016 [77] observed that residual stress is induced in metal matrix composites, during manufacturing due to the mismatch of thermal expansion coefficients between the reinforcement and matrix. Also, it has been found both theoretically and experimentally that compressive residual stress is dominant than the tensile residual stress on the surface for MMCs. Therefore, the characterization of internal/residual stresses is essential

in utilizing MMCs .There are a few types of research available on the residual stress analysis of MMCs by the 2D X-ray detector, which uses the Debye Ring $\cos \alpha$ method although such type of research work is restricted to general alloys.

2.4 Computation of effective properties

Multiscale computation of composites is a two phase process where the effective macroscopic properties are derived through micromechanics. Analysis of composites with discrete reinforcements with random orientation have been found in archival literature. There are various approaches through which these effective properties can be predicted efficiently.

Eshelby, 1957 [77] developed a method for the determination of the elastic field of an ellipsoidal inclusion, and related problems with a dilute scheme. It was proposed that a region within an isotropic elastic solid undergoes a spontaneous change of form which, if the surrounding material were absent, would be some prescribed homogeneous deformation. Because of the presence of the surrounding material stresses will be present both inside and outside the region. The resulting elastic field may be found very simply with the help of a sequence of imaginary cutting, straining and welding operations. In particular, if the region is an ellipsoid the strain inside it is uniform and may be expressed in terms of tabulated elliptic integrals. This work was proposed for the composite having a low volume fraction of reinforcements.

Christensen et al., 2016 [79] concerned with the theoretical derivation of the effective stiffness properties for two types of randomly oriented fibre systems:

- (a) A system with completely three-dimensional random orientation of fibres in an isotropic matrix phase;
- (b) A system with two-dimensional (planar) random orientation of fibres in an isotropic matrix phase, appropriate to thin sections in a state of plane stress.

The formulas derived predicted the effective isotropic properties of the composite in terms of the elastic properties of each phase and the volume concentration of the fibre phase. These results provide the theoretical limits with which experimental results can be compared to assess the effectiveness of bonds, dispersion of fibres and any other factors which may affect the performance. In the last section a comparison was made with experimental results. It utilised the aggregate model for composites with higher volume fraction of inclusions.

Mori et al., 1973 [80] have proposed a theory by assuming that the average strain in the inclusion is related to the average strain in the matrix by a fourth order tensor. It was shown that the average stress in the matrix is uniform throughout the material and independent of the position of the domain where the average treatment was carried out. It was also shown that the actual stress in the matrix is the average stress plus the locally fluctuating stress, the average of which vanishes in the matrix. Average elastic energy is also considered by taking into account the effects of the interaction among the inclusions and of the presence of the free boundary. The relation between the uniform strains in the inclusion in the matrix was provided by this fourth order tensor.

Benveniste et al., 1987 [81] extended the Mori-Tanaka theory to investigate the stress and strain concentration tensors along with the overall elastic modulus of composites. In this paper they adopted the ‘direct approach’ of defining and computing effective moduli. By elucidating the nature of the approximation in applying Mori—Tanaka's theory to composites insofar as the ‘concentration-factor’ tensors are concerned, a straightforward exposition and interpretation of the method which are different than those existing in previous formulations was achieved. The analysis was given for two-phase composites with anisotropic elastic constituents and an inclusion phase consisting of aligned or randomly oriented ellipsoidal particles. The derived simple expressions for the predicted stiffness and compliance tensors permit a proof of the self-consistency of the method, a discussion of the predictions' relation to

the bounds in the case of isotropic constituents and randomly oriented ellipsoidal particles, and finally a derivation of some new results in randomly cracked bodies with penny-shaped cracks.

Abaimov et al., 2019 [82] explored the differences among one, two, and multi-step procedures in the Mori-Tanaka-Benveniste theory. It was concluded that for two-phase unidirectional composites, two- and one-step procedures differ by change in effective field related to change in concentration tensors. For porosity, two- and one-step homogenizations become identical if Eshelby tensor is multiplied by a scalar coefficient depending on volume fractions. Finally, applicability of the two-step procedure was verified for anisotropic three-phase composites.

Imani et al., 2018 [83] proposed two modifications to be applied to the well-known Mori-Tanaka (MT) scheme to improve its performance in the estimation of the mechanical properties of highly porous ceramic structures containing complicated agglomerates of merged and open-cell spherical pores of different radii. In the first modification, the effect of the merged pores was considered by estimating their number with the theory of geometrical probabilities and treating them as corresponding ellipsoids of the same volume. In the second modification, porous structures containing open pores were treated as a damaged material with reduced load-carrying capacity and the formulations are modified to consider the effect of the open pores. In order to investigate the reliability of the analytical estimations, different groups of artificial porous structures with porosity values ranging from 10% to 90% were constructed by random positioning of the spherical voids of different radii in a representative volume element (RVE) and their effective elastic properties are obtained by means of the finite element method (FEM). For each level of porosity, a total of 30 random structures were examined to assess the variations caused by the statistical nature of the microstructure. Comparison between the findings of the statistical FEM and the analytical results showed that the proposed modifications considerably increase the precision of the MT scheme in the estimation of the

effective elastic moduli of highly porous materials. Good agreement were also observed between the results obtained from the developed formulations and published numerical and experimental observations for ceramic structures.

Gubran et al., 2014 [84] designed six automotive propeller shafts made of different materials are. Finite element modeling based on shell element was used in the eigenvalue analysis. Shaft weights, buckling torque and dynamic performance for different design alternatives, were studied. Simulated Annealing (SA) Algorithm was used for optimization. Results obtained clearly show the possibility of designing a single-piece propeller hybrid shaft made of fibre-reinforced composite and aluminum tube having less weight compared to that of steel shaft and having its fundamental natural frequency above the shaft operating speed.

Elomari et al., 1995 [85] investigated the effect of prestraining on the elastic modulus, E , and damping capacity, $\tan \Phi$ of 10 and 20 vol. % Al_2O_3 particle-reinforced composites as function of temperature using dynamic mechanical analysis. Both elastic modulus and damping capacity were found to increase with volume fraction. At 10 vol.% the modulus and damping were relatively insensitive to prestrain. However, at 20 vol. % it was observed that the modulus decreased with increasing prestrain while damping increased significantly. These results are discussed in terms of fraction of broken particles, particle size, and differential in thermal expansion between the matrix and Al_2O_3 particulate. The 20 vol.% composite which showed the greatest particle damage with prestrain also had the highest damping capacity, $\tan \Phi \sim 0.42$ at 10 % prestrain. Therefore, the damping capacity measured with the DMA can be used as a sensitive indicator of microstructural damage in MMCs.

Zhang et al., 1993 [86] presented a concise summary of the damping data for metallic materials, ceramic materials and MMCs. The damping data for metals, alloys and ceramics are useful in selecting constituents for processing an MMC, while the data on present MMCs may indicate some prospective research trends to obtain high damping MMCs to MMC researchers.

The damping data reviewed in the paper reveal that MMCs may be effectively designed to exhibit attractive damping characteristics compared with their matrix materials although the highest value of damping capacity for the present MMCs has not reached the same level as some hidamets. While continuous fibre-reinforced MMCs show the same or slightly higher damping capacity than the matrix, particulate-reinforced MMCs exhibit much improved damping behaviour. It is also evident, however, that it will be necessary to develop a detailed understanding of the mechanisms governing the intrinsic damping behaviour of the individual MMCs before these MMCs can measure up to their commercial potential.

Eruslu et al., 2007 [87] explored the vibration behavior of the Al/Sic metal matrix composite plates containing randomly oriented and unidirectional aligned reinforcements was studied. The effective elastic modulus of composite material was expressed by using different micromechanical approaches namely: the Mori-Tanaka mean field theory, rule of mixture and Mori-Tanaka based transversely isotropic solution. Governing equations of vibration were solved by using Navier type solution, Ritz method and Ansys finite element program. The elasticity modulus and vibration results indicate that for randomly oriented case probability density function based transversely isotropic solution is good agreement with experimental measurements and better results than Mori-Tanaka theory. The rule of mixture elastic modulus results is smaller than the effective elastic modulus results of transversely isotropic solutions. In the analysis of unidirectional oriented composite for larger aspect ratios numerical results approximate continuous fibers.

Luan et al., 2015 [88] calculated the Macro-mechanics properties parameters of the material aiming at the question of predicting mechanics properties of long fiber reinforced metal matrix composites (MMC) shafts, two periodical arrangement of fiber. Six representative volume element models (RVE) were presented. The results were compared with that of three frequently Micro-mechanics models. On this basis, taking a low pressure turbine as study

object, then the results calculated of specified RVE model were used in modal analysis of shafts with MMC. The numerical simulation method is used to calculate natural frequency, analyzing the influence of layers angles, thicknesses and sequences on modal and natural frequency.

Chang et al., 2004 [89] studied vibration behaviors of the rotating composite shafts containing randomly oriented reinforcements . The Mori–Tanaka mean-field theory is adopted here to account for the interaction at the finite concentrations of reinforcements in the composite material. The effective elastic moduli of the composite material are expressed as a function of the phase properties, volume fraction, and orientation angles of its constituents. The finite element model of the rotating continuous fiber-reinforced composite shafts derived was extended here to the case that contains the fiber inclusions by taking these effective elastic moduli into account. Based on this model, the natural frequencies of the stationary shafts, and the whirling speeds as well as the critical speeds of the rotating shafts are investigated. The results reveal that the content and the orientation of reinforcements have great influence on the dynamic characteristics of the composite shafts.

2.5 Dynamic Analysis of Metal Matrix Composite Rotor

For various rotor systems, natural frequency, steady state response, stability and the transient response passing through the critical speeds are the pivot of dynamic analysis of the rotors. In addition to that, a system approach which can encapsulate different domains of energy system is a prerequisite for the analysis of rotor systems. For that reason, a modular and robust rotordynamic model is required for the study of the response of the rotor system for different internal properties. Bond graph is a multi-domain approach which is capable to support such an objective. One of its advantage is that it enables the user to visualize the power flow and track the effects of these variants which can be very useful for understanding the counterintuitive phenomenon of rotordynamics for any system.

This approach, coined by Paynter et. al. [90] has been adopted in various researches for modelling the different variants of rotor dynamic systems.

Campos et al., 2005 [91] proposed simple model capable of allowing visualization of the parameters and problematic aspects associated with an unbalanced rotor (Jeffcott rotor) using bond graphs, which provide a structured and unified method for modeling a large class of nonlinear, multienergetic systems. A high-fidelity, experimentally proven bond graph model of the Jeffcott rotor to aid in the design and analysis of high-speed rotational machinery often associated with pulsed energy systems was provided. The intent of the model was the ability to use it as a modular and foundational piece in more complex rotordynamic models.

Hubbard et al., 1979 [92] has used the bond graph technique interpret whirling modes and critical frequencies associated to it. The formulation was shown to be a natural one when control forces and moments are included for active control of the whirling modes. Critical frequencies were interpreted as rotational speeds at which non-zero equilibrium configurations exist for displacements (as opposed to the more familiar momenta) and arise when the system dynamics matrix of the complete whirl motion has two zero eigenvalues. In addition, oscillatory modes corresponding to non-zero eigenvalues are examined. Time simulations and other numerical results are given for an example flywheel system which has been proposed for electric utility energy storage.

Vikas et al., 2011 [93] successfully introduced both external and internal damping of the shafts in bond graph. The dynamic behavior of a hollow rotor shaft with internal damping driven by a dissipative coupling was illustrated. The coupling in the system was absolutely flexible in transverse and bending; however, it was assumed to be torsionally rigid. Bond graph was adopted for modeling as it facilitates the system modeling from the physical paradigm itself, and the model can be easily extended to incorporate modifications. Simulation results show interesting phenomenon of limiting behavior of rotor shaft with internal damping beyond

the threshold speed of instability. It is further shown that the shaft entrainment frequency of the rotor shaft primarily depends on the ratio of external and internal damping.

Borutzky, 2011 [94] provided an insight to the bond graph modelling of engineering systems. It was stated that dynamics of the rotor systems depends decidedly on the internal damping as well as external damping of the system. External damping as stated is the external friction acted because of the resistance of the medium (liquid/air). While internal damping is the friction existing within the rotating part and is the intrinsic property of the material. Since internal damping is the material property, the dynamics of the rotor changes drastically with the change of material and calibrated internal damping is mandatory to correctly imitate the dynamic response computationally.

Karthikeyan et al., 2015 [95] generated the rotor response with finite element (FE) model by assuming an ideal drive. Thereafter, the rotor system's response with ideal drive was used in a power balance equation to theoretically predict the amplitude and speed characteristics of the same rotor system when it is driven through a non-ideal drive. The integrated system with drive-rotor interaction is modeled in bond graph (BG) form and the transient analysis from the BG model is used to validate the theoretical results. The results are important from the point of actuator sizing for rotor dynamic systems.

But for composites, internal damping changes with various factors like reinforcement size, aspect ratio, volume percentage etc. Efforts for determining the effect of these factors on the modal response by utilizing Finite element method are shown in various researches [96,97]. But these studies are limited to the linear and small variation and have only highlighted the effect of damping on the rotordynamics of composite shafts.

Kafi et. al., 2019 [98] investigated the nonlinear nonstationary vibration of a rotating composite shaft passing through critical speed excited by non-ideal energy source. It was

shown that damping has a main effect on the dynamic response of the composite shafts and analyzed the nonlinear dynamic response of the composite shaft.

2.6 Experimental Validation

Experimental characterization of metal matrix composites is limited to the evaluation of tensile strength, impact strength and tribological properties. There has been a scarcity of experimental analysis for modal response of the shafts. Critical speeds for Aluminum–Boron Carbide Metal Matrix Composite shaft has been evaluated both computationally and experimentally in recent work [99]. However, they have directly used the effective properties of the MMC shaft and not compared the analytical result.

Vipin J. et. al., 2019 [100] have used beams with smaller length specimens for optimization and dynamic analysis of silicon carbide reinforced different aluminium matrix MMCs. However, smaller length specimens are restricted for rotor drive applications.

Various researches have reported a significant increase of tensile strength, yield strength and hardness on the addition of alumina particles in the aluminium matrix [101-103]. However, determination of properties such as Young's modulus, Poisson's ratio and shear modulus are also important. As discussed above, these effective properties are computationally derived successfully by various researchers. Experimental validation of these effective properties with standard practice and technique is equally important. These properties can be experimentally determined by impact hammer test based on ASTM E1876 standard [104].

Praveen et al., 2019 [105] performed an impact hammer test based on ASTM E1876 to evaluate the dynamic elastic properties of composites at ambient temperatures. The micro, macro and structural analysis of composites with and without reinforcement of multi walled carbon nanotubes (MWCNT) was investigated. The impact hammer test based on ASTM E1876, tensile test based on ASTM D3039 and free and forced vibration analysis of the hybrid

composite beams were carried out to identify the elastic properties, fundamental natural frequencies, damping ratio and transverse deflection of the hybrid structure. It was shown that the addition of 1 wt% of COOH-MWCNT in fiber reinforced composite beam increases the stiffness of the structure and consequently increases the natural frequencies and damping at each resonant response dominant peaks. The strong adhesion of bonding and proper dispersion of CNTs in the wide surface area of composite strengthen the polymer composites substantially than those of the Glass/epoxy composite structures without reinforcement of MWCNT.

Daramola et al., 2020 [106] compared the mean-field homogenization technique with the experiment and estimated an error of 4.2% between the predicted and experimental values.

2.7 Outcome of Literature Review

After thorough literature survey on development, characterization and dynamic analysis of composite rotor following points are observed.

- A thorough research is available on Carbon/graphite epoxy polymer composite shaft but the field of metal matrix composite rotors is yet to be explored.
- In metal matrix composites vibration analysis has been done on plates but rotors behavior is still to be investigated.
- An exhaustive study is required to be done to study the effect of reinforcements on the vibration characteristics of these rotors.
- Processes for manufacturing these rotors and their effect on its properties are to be understood thoroughly in order to have uniform dispersion, improved wettability and uniform interfacial bonding without affecting the microstructural integrity of composites.
- Experimental validation is not much focused for composite effective properties and researches are limited to computational analysis of these properties.

- Collective effort in the field of metal matrix composite with discrete randomly oriented particle composites has not been seen in the literature.

Next section defines problem statement of present research investigation.

2.8 Problem Statement

A reliable and more accurate methodology is needed to be adopted for analysis of composite rotors especially for metal matrix composites. So, this research work is planned to conduct an experimental and analytical study for the development and characterization of composite rotors with enhanced mechanical and physical properties fabricated through liquid metallurgy route. The upcoming section explains thesis objectives.

2.9 Thesis Objectives

- Development of metal matrix composite rotor through stir casting route with aluminium as matrix and alumina as reinforcement.
- Characterization of metal matrix composite rotor material.
- Development of computational framework for predicting effective properties of composite rotor material.
- Dynamic investigation and experimental validation of composite rotor.

Research methodology endorsed for present research work has been discussed in next section.

2.10 Research Methodology

The research methodology adopted to fulfil various research objectives of proposed research work involved the following steps:

- The methodology begins with literature review that relates to this work for better understanding of subject and knowing state of the art
- To identify the relevant aluminium alloy as base metal and reinforcement
- Design of experiment and optimization of process parameters by utilizing non-destructive method of image analysis.
- Synthesis of metal matrix composite shafts of standard dimension with cost effective and feasible stir casting method.
- Preparation of standard specimens for various characterizations
- Microstructural, elemental, physical and mechanical characterization of developed composites
- Computation of effective properties of composite material through mean field homogenization and image analysis.
- Experimental validation of the computed effective properties using impact hammer test.
- Dynamic analysis of the composite rotor using bond graph modelling.

Summary of present chapter has been conferred in a nutshell in next section.

2.11 Summary

The present chapter discusses salient features of research work carried out by various researchers in recent years. Different phases and aspects related to the development, characterization and dynamic analysis of aluminium metal matrix composites have been discussed. Fabrication of metal matrix composite by stir casting method have been discussed in next chapter.

Development of Metal Matrix Composite

3.1 Introduction

The composite shaft samples are fabricated using a stir casting process, as shown in Fig. 3.1. The aluminium 6061 metal matrix is mixed through stirring with a different weight percentage of alumina (Mesh size 100-325, calcined, 99% pure Al_2O_3 , 0.2% SiO_2 , 0.25% Fe_2O_3 , Other balance) supplied by Loba Chemie Pvt. Ltd. The low density alumina is on the surface of the melt and is required to be mixed with the molten material. The pressure difference due to the vortex created due to stirring action mixes the reinforcement into the metal matrix. The high speed vortex generates a low pressure at the impeller end and this low pressure results in the infusion of alumina at atmospheric pressure. To increase the wettability of the alumina particles in the aluminium matrix, the alumina particles were preheated, and magnesium was added during the stir casting process. Magnesium forms an interface of MgO and MgAl_2O_4 between the alumina and aluminium, resulting in better wettability and strong bonding. The stirred material was then casted through gravity sand casting mold made by Dunger Lal Metal Foundry Works, Anand Parbat, New Delhi. The sand mold was made in a steel frame of 75 inch X 25 inch X 15 inch for both cope and drag. Sand for casting was composed of high-quality quartz sand, about 10 percent bentonite clay (as the binder), 2 to 5 percent water and about 5 percent sea coal (a carbonaceous mold additive to improve casting finish).

For a cylindrical cavity of 1000mm length and 24 mm diameter the gating ratio of 1:4:4 was used with proper vent system. The throat area was kept as 12 mm^2 and the sprue height was

180 mm. The major issue was with the length of the specimen and the gas entrapment. For the same reason proper venting and riser arrangement was used to permit the escape of evolved air and mold gases as the mold cavity is being filled with the molten metal. as shown in Fig. 1(d).

Various factors affect the properties of the composite fabricated through the stir casting process. Stir casting is one of the most economical composite manufacturing processes, which is highly suitable for large scale production of the components. Various properties such as tensile strength, hardness and wear resistance are related to the process parameters. Process

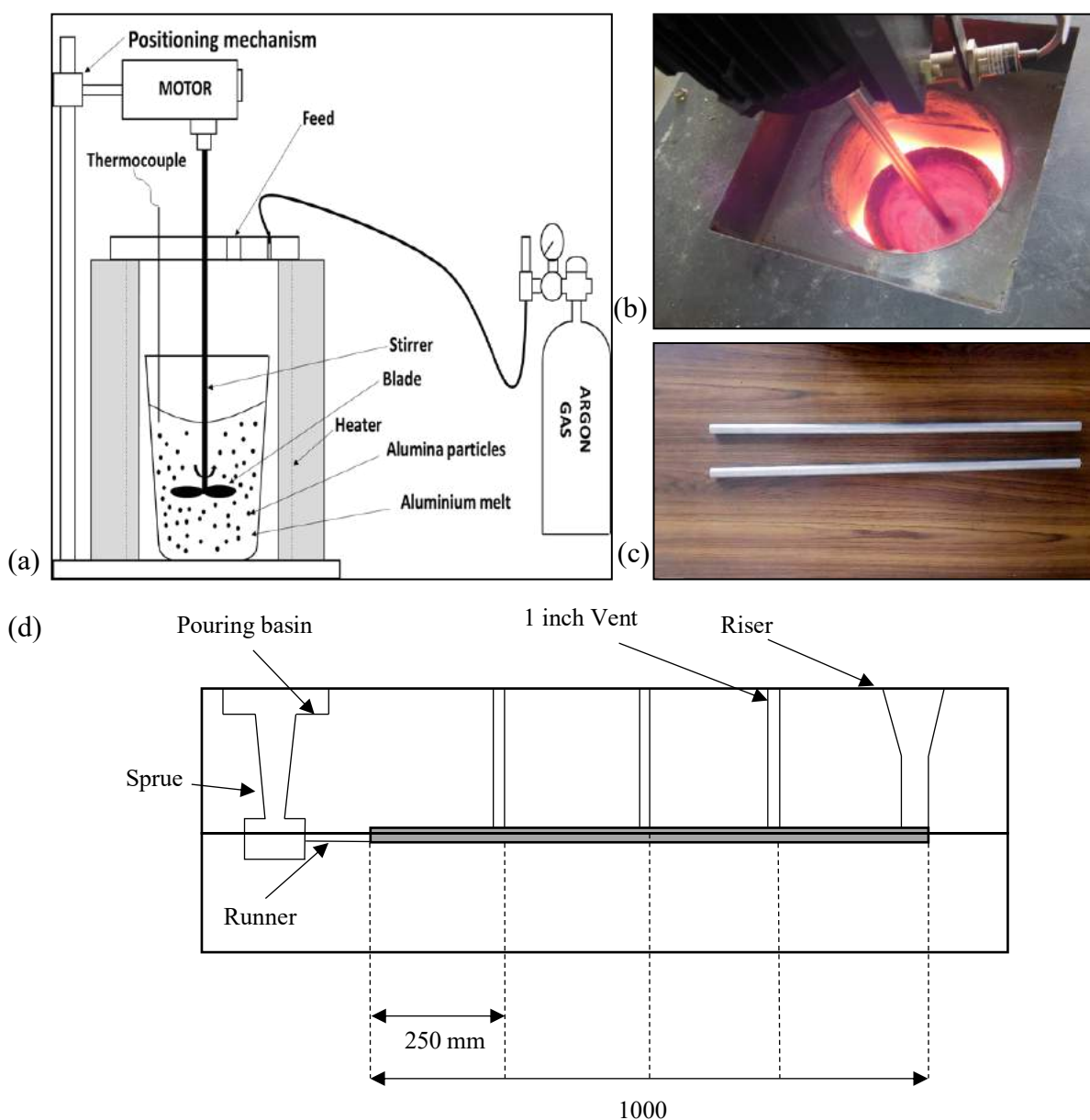


Fig 3.1: (a) Stir casting set up (b) Vortex Generation (c) Stir casted shaft (d) Sand casting set-up

parameters have been optimized for these properties in different researches. Although, experimental evaluation of these properties is destructive and leads to a loss of the product and cost. Stirrer rpm, stirring time, furnace temperature and preheat temperatures are the major factors that affect the properties of the fabricated composite.

These parameters are optimized by a novel approach where a newly developed distribution index and area fraction of the composites are quantitatively determined through microstructural image analysis method, for maximum area fraction and minimum distribution index. The distribution index (D_{index}) is calculated by estimating the free-path spacing within particles. The stir casting process parameters (Stirrer rpm, time of stirring, furnace temperature and preheat temperatures) are optimised by Box- Behnken design of response surface methodology. The quantitatively assessed responses provide an authentic base for optimisation of process parameters. The Scanning Electron Microscopy (SEM) images are taken for different samples, and then these images are analysis through an image analysis method. The quantitatively assessed responses of homogeneity and area fraction are determined by analyzing the images. The stir casting process parameters are optimized by Box-Behnken design for homogeneity and area fraction responses. For optimization the 18% weight percentage of alumina is added for each operation. The Furnace Temperature range was taken as $650^{\circ}\text{C} - 850^{\circ}\text{C}$ since 850°C is the highest operating limit, and the aluminium melt does not sustain for sufficient Time at a temperature below 650°C . The stirring time was changed within a range of 300 - 600 seconds and the stirring rotation was ranged within 450 to 650 rpm. These ranges were the manufacturing specifications of the stir casting machine. The particles were also preheated to the temperature ranging from $200^{\circ}\text{C} - 300^{\circ}\text{C}$.

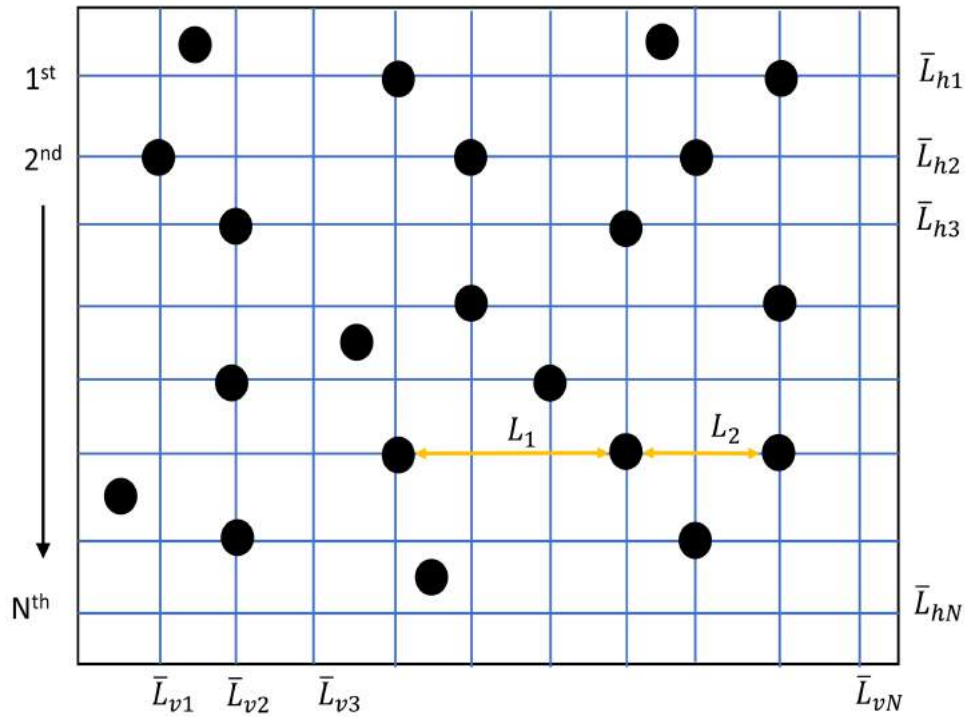


Fig 3.2: Proposed methodology for quantifying homogeneity through image analysis method.

3.2 Image Analysis Method

The homogeneity and the area fraction of the composite are analyzed through image analysis, and the values were quantitatively determined. The methodology of the quantification of the particle distribution is based on the mean free path spacing. The distance between the particles is considered as a basis of the determination of the homogeneity. The 8-bit greyscale image is converted into a binary image, and the particles are quantized into elliptical shapes by using *ImageJ software*®. The area of a binary image is divided into several grid lines so that there is a total of $2N$ lines (N horizontal lines + N vertical lines). The black coloured circles (Fig. 3.2) are the denotation of the particles distribution. All the particles are separated from its neighbouring reinforcement by a mean-free spacing (termed as L_1, L_2, \dots, L_n) as shown in Fig. 3.2.

These values are consolidated and processed into a unit of micrometre (μm) by proper scaling. For each line, the arithmetic mean (A.M) of the scaled free-path spacing are calculated separately, shown in Eq. (3.1) and Eq. (3.2).

$$\overline{L_{h1}} = \frac{1}{n} \sum_{i=1}^n L_i \quad (3.1)$$

$$\overline{L_{v1}} = \frac{1}{n} \sum_{i=1}^n L_i \quad (3.2)$$

Where vertical and horizontal lines as abbreviated as v , h respectively and n is the free -spacing number in the line.

The overall arithmetic mean (\bar{L}) and the standard deviation (σ) are then calculated by Eq. (3.3) and Eq. (3.4).

$$\bar{L} = \frac{(\overline{L_{h1}} + \overline{L_{h2}} \dots \dots + \overline{L_{hN}}) + (\overline{L_{v1}} + \overline{L_{v2}} \dots \dots + \overline{L_{vN}})}{2N} \quad (3.3)$$

$$\sigma = \sqrt{\frac{[\sum_{i=1}^N (\overline{L_{hi}} - \bar{L})^2] + [\sum_{i=1}^N (\overline{L_{vi}} - \bar{L})^2]}{2N - 1}} \quad (3.4)$$

As discussed above, the arithmetic mean and the standard deviation can be used to determine the homogeneity of particles in the composite system. For perfectly homogeneous systems, the arithmetic mean of the mean-free spacing between the particles for all lines analyzed should be same. Also, the values of the individual line mean-free spacing should be equal to the overall arithmetic mean of all the lines. However, for inhomogeneous systems, there will be a deviation in the values. In order to assess the variability of the results, the coefficient of variation is taken as a standard measure of distribution of particles in the matrix. This coefficient of variance termed as D_{index} is the ratio of the standard deviation and the overall arithmetic mean, which is shown in Eq. (3.5).

$$D_{index} = \frac{\sigma}{\bar{L}} \quad (3.5)$$

The higher value of D_{index} indicates a high deviation in the values for the mean value and low homogeneity of the particles. Composites with a high level of agglomeration will have high D_{index} value and vice-versa. For perfectly homogeneous composites, the D_{index} value will

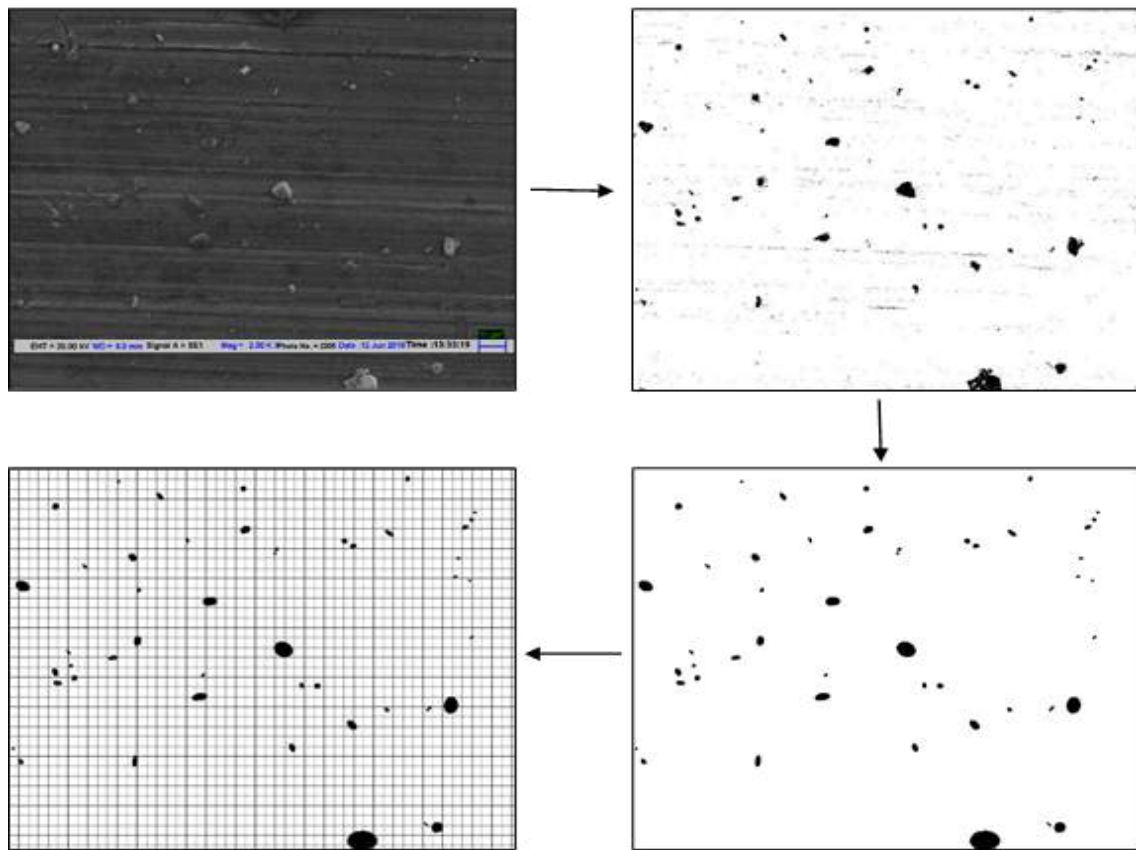


Fig 3.3: (a) 8-bit grayscale SEM image converted into (b) Binary image and (c) Denoised image with analyzed particles in elliptical form and (d) Grid formation of the image be zero since there will be no deviation in the mean-free spacing values for different lines and the arithmetic mean. As an example, image analysis of composite fabricated at furnace temperature 650°C , 550 stirrer rpm, 300 seconds stirring Time and 250°C preheat Temperature are shown in Fig. 3.3.

The Scanning Electron microscopy (SEM) images with two different magnification levels of 2K X (2000) and 1K X(1000) are taken by the *Zeiss EVO 50* at SEM Central Facility, Indian Institute of Technology, Delhi. The magnification of 2K X provided better visibility and bifurcation of alumina reinforcement and the matrix. However, images of magnification 1K X were selected for optimization process because this magnification level provided a more substantial area for a better understanding of homogeneity and distribution. The image 8-bit grayscale image is then converted into a binary image, and the particles are analyzed by denoising and elliptical transformation. Area fraction is analyzed simply without the use of

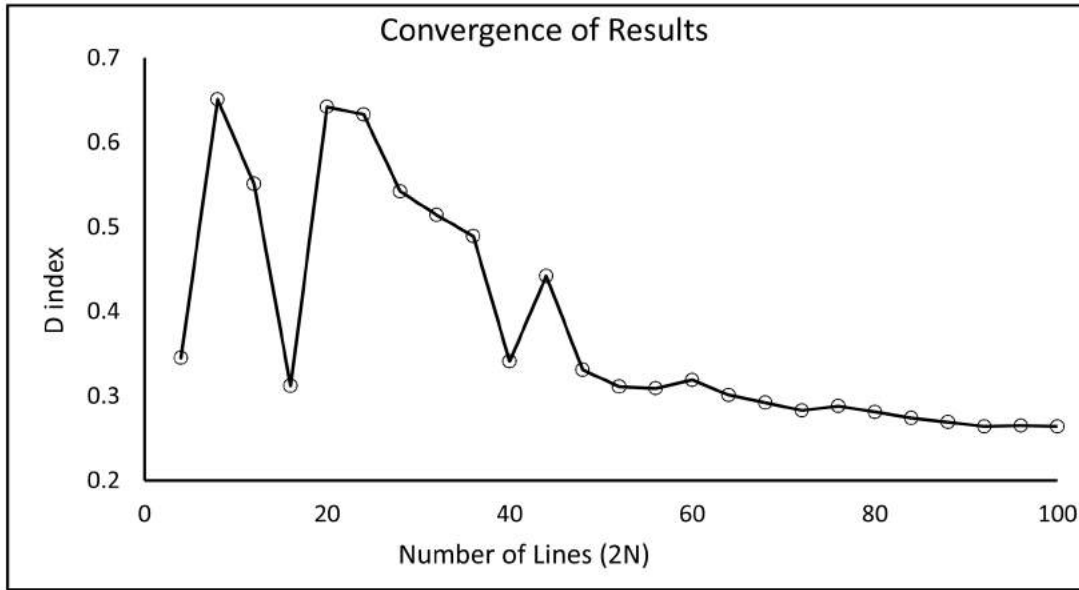


Fig 3.4: Convergence of D_{index} values for $2N$ number of lines

grid lines. The D_{index} is calculated by dividing the image into $2N$ grid lines. The grid lines are adjusted so that the values of D_{index} are converged to a stable form, as shown in Fig. 3.4. The D_{index} value converged to 0.264 for $2N=96$ lines.

3.3 Box-Behnken Design for Parametric Optimization

The stir casting parameters are optimized for the maximization of the area fraction and minimization of the D_{index} . The experimental matrix was statistically designed by response surface methodology (RSM) technique coupled with Box-Behnken design using *Design expert software 12.0 (State Ease, USA)*. Independent parameters considered for process optimization are Stirring Time, Stirring RPM, Furnace Temperature and Preheat Temperature. Area fraction percentage and D_{index} are the responses. Box-Behnken designs (BBDs) are useful designs for fitting second-order response-surface models. In this method, only three levels of each factor are used, and therefore fewer runs are required as compared to Central composite design (CCD). The parametric variables are coded at three equally spaced levels (-1, 0, +1) for low, intermediate and high values respectively. For experimentation, 29 set of parametric combinations are employed for evaluation and optimization. A non-linear regression method

Table 3.1 Response of 29 sets of experiments determined by Box-Behnken design

STD	RUN	TIME (seconds)	RPM	Furnace Temperature	Preheat Temperature	D index	% Area
18	1	600	550	650	250	0.247	11.41
27	2	450	550	750	250	0.198	11.17
21	3	450	450	750	200	0.312	8.21
9	4	300	550	750	200	0.267	6.11
17	5	300	550	650	250	0.264	6.13
15	6	450	450	850	250	0.312	8.21
19	7	300	550	850	250	0.271	6.04
29	8	450	550	750	250	0.198	11.17
24	9	450	650	750	300	0.288	11.51
8	10	450	550	850	300	0.206	11.06
14	11	450	650	650	250	0.302	11.45
12	12	600	550	750	300	0.238	11.52
23	13	450	450	750	300	0.309	8.42
6	14	450	550	850	200	0.208	11.03
16	15	450	650	850	250	0.289	11.42
5	16	450	550	650	200	0.221	10.08
26	17	450	550	750	250	0.198	11.17
7	18	450	550	650	300	0.217	10.11
4	19	600	650	750	250	0.369	11.61
25	20	450	550	750	250	0.198	11.17
20	21	600	550	850	250	0.231	11.48
11	22	300	550	750	300	0.255	6.45
28	23	450	550	750	250	0.198	11.17
13	24	450	450	650	250	0.324	8.13
10	25	600	550	750	200	0.243	11.46
22	26	450	650	750	200	0.292	11.47
3	27	300	650	750	250	0.381	7.06
1	28	300	450	750	250	0.421	4.31
2	29	600	450	750	250	0.406	11.11

is used to fit in the second-order polynomial equation in terms of a quadratic response described in Eq. (3.6).

$$Y = \beta_0 + \sum \beta_i x_i + \sum \beta_{ii} x_{ii}^2 + \sum \beta_{ij} x_i x_j + \varepsilon \quad (3.6)$$

where y is the output response, β is the regression coefficient, x_i is the i_{th} control factor and ε is the random error. Moreover, the results were analyzed using the coefficient of determination (R^2), Pareto analysis of variance (ANOVA) and statistical and response plots.

3.4 Results and Discussion

The 29 sets of experimental parameters are determined by Box-Behnken design. It is observed that due to uncertainty, results deviate even when the process parameters are identical. Therefore, in this work, three samples are prepared corresponding to each run of the experiment. Also, there will always be an inhomogeneity within the sample which leads to interference on the results. Therefore, to avoid this uncertainty, eight micrographs were randomly chosen from the different positions within the sample.

For each micrograph, the value of D_{index} and area fraction was evaluated, and the mean value for each sample was calculated. The mean values of three different samples were averaged and selected as response data for each experimental run. The responses and the set of experimentation are shown in Table 3.1.

3.4.1 Pareto analysis of variance (ANOVA) and coefficient of determination (R^2)

The Pareto analysis of variance and coefficient of determination (R^2) analysis is performed for D_{index} and area fraction. The ANOVA analysis for D_{index} is shown in Table 3.2. The response of D_{index} is analyzed by inverse transformation since the nature of response was similar to the rate responses. The F -value of model is 216.55, which denotes the significance of the model

with a 99.99 % confidence level. P-values (**less than 0.0001**) indicate that in this case, *A*, *B*, *C*, *AC*, *A*², *B*², *C*², *D*² are significant model terms. *A*, *A*², *B*², *C*² are considered significant with 99.99% confidence level and *B*, *C*, *AC* and *D*² are considered significant with a 95 % confidence level. Values higher than 0.1000 indicate the model terms are not significant in the confidence interval of 90%. In this analysis, the Sum of Squares (SS) value of the model is much larger than the residual SS value. Thus, the pure error is negligible and approximated as zero in analysis. Due to this reason, no results are obtained for the F value and p-value in Lack of Fit (LOF) Test.

Table 3.2 ANOVA analysis for D_{index}

Source	Sum of Squares	df	Mean Square	F-value	p-value
Model	20.01	14	1.43	216.55	< 0.0001
A-Time	0.2473	1	0.2473	37.47	< 0.0001
B-RPM	0.1708	1	0.1708	25.88	0.0002
C-Furnance Temp	0.0799	1	0.0799	12.10	0.0037
D-Preheat Temp	0.0185	1	0.0185	2.81	0.1161
AB	1.443E-06	1	1.443E-06	0.0002	0.9884
AC	0.0358	1	0.0358	5.42	0.0354
AD	0.0020	1	0.0020	0.3054	0.5892
BC	0.0002	1	0.0002	0.0346	0.8550
BD	0.0001	1	0.0001	0.0102	0.9208
CD	0.0003	1	0.0003	0.0511	0.8244
A²	5.34	1	5.34	809.10	< 0.0001
B²	16.34	1	16.34	2475.37	< 0.0001
C²	0.2460	1	0.2460	37.26	< 0.0001
D²	0.1351	1	0.1351	20.46	0.0005
Residual	0.0924	14	0.0066		
Lack of Fit	0.0924	10	0.0092		
Pure Error	0.0000	4	0.0000		
Cor Total	20.10	28			

Coefficient of determination (R^2) analysis for D_{index} is shown in Table 3.3.

Table 3.3 Coefficient of determination (R^2) analysis

Parameter	Value
Std. Dev.	0.0812
Mean	3.88
C.V. %	2.10
R^2	0.9954
Adjusted R^2	0.9908
Predicted R^2	0.9735
Adeq. Precision	47.2009

The Predicted R^2 of 0.9735 is in rational agreement with the Adjusted R^2 of 0.9908 with a difference of 0.0173 (desirable difference is less than 0.2). Also, the R^2 value of 0.9954 shows the closeness of the solution with the ideal solution. The signal to noise ratio is determined by Adeq. Precision and ratio greater than four is desirable for analysis. The ratio of 47.201 indicates an adequate signal. This model can be used to navigate the design space.

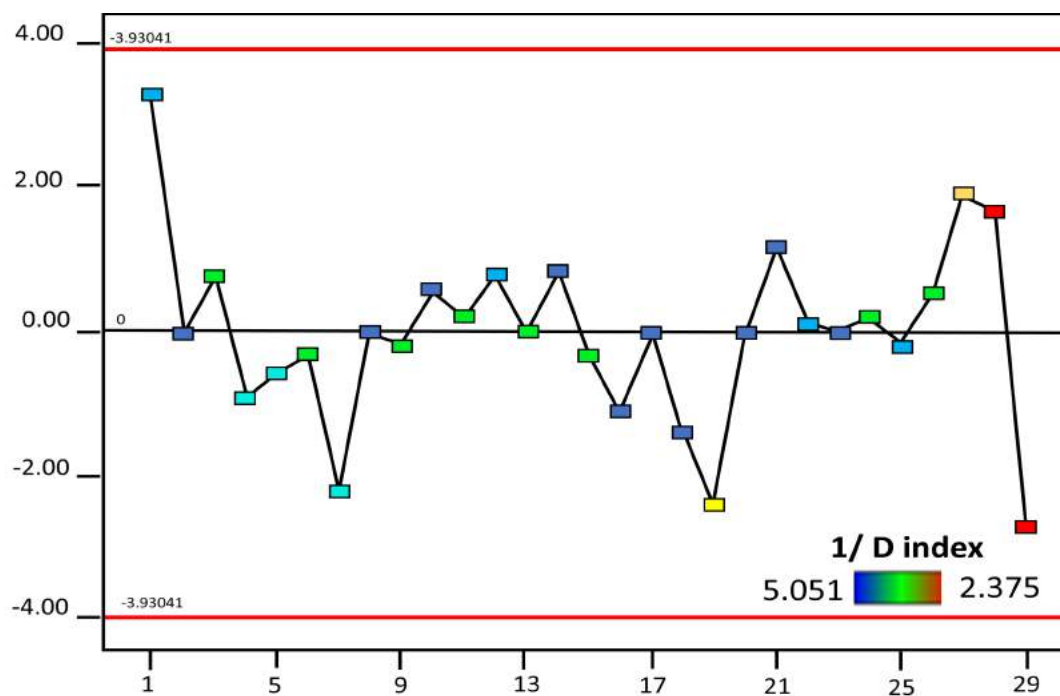


Fig 3.5: Residual vs Run plot for D_{index}

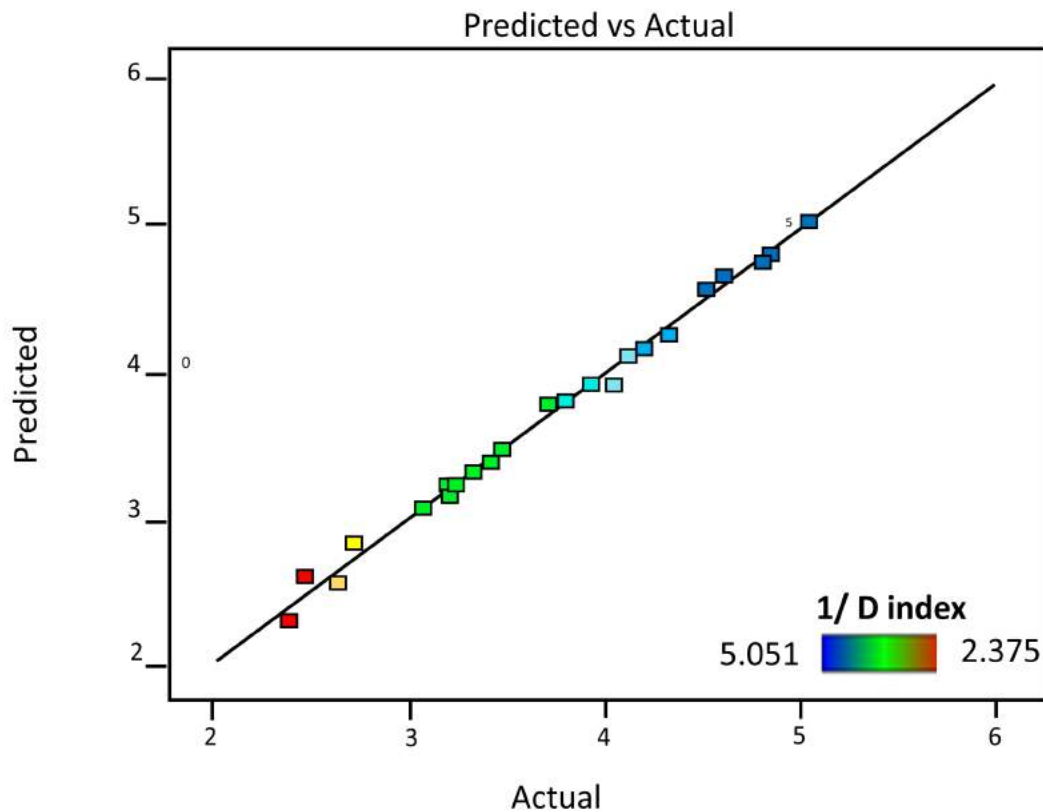


Fig 3.6: Dissipated scatter plot for D_{index}

The validity of this created model was again affirmed for D_{index} by residual vs run plot graphs and dissipated scatter diagrams, as shown in Fig. 3.5 and Fig. 3.6. The result is not varying much with the linear prediction showing the effectiveness of the model. Also, the externally studentized residuals are well within the accepted range of $+3.93$ to -3.93 , and the scatter is in proximity to the predicted line. Moreover, the externally studentized residuals are distributed on both sides of the mean line, which depicts that there is no pattern in the variation.

The ANOVA analysis for area fraction is shown in Table 3.4.

The F-value of model is 57.51, which denotes the significance of the model with a 99.99% confidence level. The P-values denotes that in this case, A, B, AB, A^2 , B^2 , C^2 are significant model terms. A, B, A^2 , B^2 are considered significant with 99.99% confidence level and AB, and C^2 are considered significant with a 95% confidence level. Coefficient of determination (R^2) analysis for area fraction is shown in Table 3.5.

Table 3.4 ANOVA analysis for area fraction

SOURCE	Sum of Squares	df	Mean Square	F-value	p-value
MODEL	136.61	14	9.76	57.51	< 0.0001
A-TIME	86.99	1	86.99	512.68	< 0.0001
B-RPM	22.17	1	22.17	130.64	< 0.0001
C-FURNANCE TEMP	0.3104	1	0.3104	1.83	0.1977
D-PREHEAT TEMP	0.0420	1	0.0420	0.2476	0.6265
AB	1.07	1	1.07	6.31	0.0249
AC	0.0064	1	0.0064	0.0377	0.8488
AD	0.0196	1	0.0196	0.1155	0.7390
BC	0.0030	1	0.0030	0.0178	0.8957
BD	0.0072	1	0.0072	0.0426	0.8395
CD	0.0000	1	0.0000	0.0000	1.0000
A ²	23.95	1	23.95	141.16	< 0.0001
B ²	5.19	1	5.19	30.56	< 0.0001
C ²	1.13	1	1.13	6.64	0.0220
D ²	0.6100	1	0.6100	3.60	0.0788
RESIDUAL	2.38	14	0.1697		
LACK OF FIT	2.38	10	0.2376		
PURE ERROR	0.0000	4	0.0000		
COR TOTAL	138.98	28			

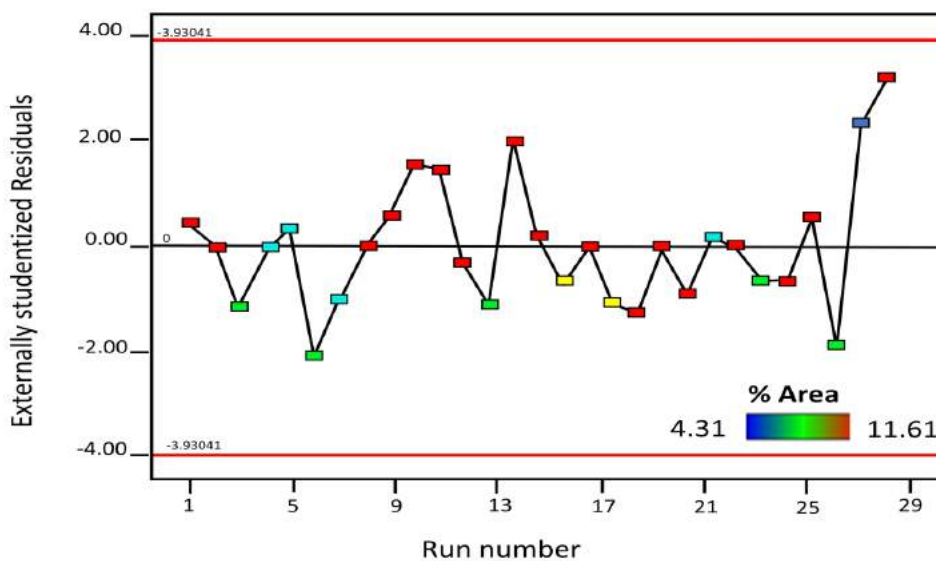


Fig 3.7: Residual vs Run plot for area fraction for 2N number of lines

The **Predicted R²** of 0.9015 is in reasonable agreement with the **Adjusted R²** of 0.9658. **Adeq Precision** measures the signal to noise ratio. The ratio of 27.352 indicates an adequate signal. The validity of this created model was also determined for area fraction by residual vs run plot graphs and dissipated scatter diagrams, as shown in Fig. 3.7 and Fig. 3.8. The externally studentized residuals are well within the accepted range of +3.93 to -3.93, and

Table 3.5 Coefficient of determination (R²) analysis for area fraction

Parameter	Value
Std. Dev.	0.4119
Mean	9.71
C.V. %	4.24
R ²	0.9829
Adjusted R ²	0.9658
Predicted R ²	0.9015
Adeq. Precision	27.3524

the scatter is in proximity to the predicted line.

The mathematical formulation in terms of coded factors for the D_{index} and the area fraction are shown in Eq. (3.7) and Eq. (3.8).

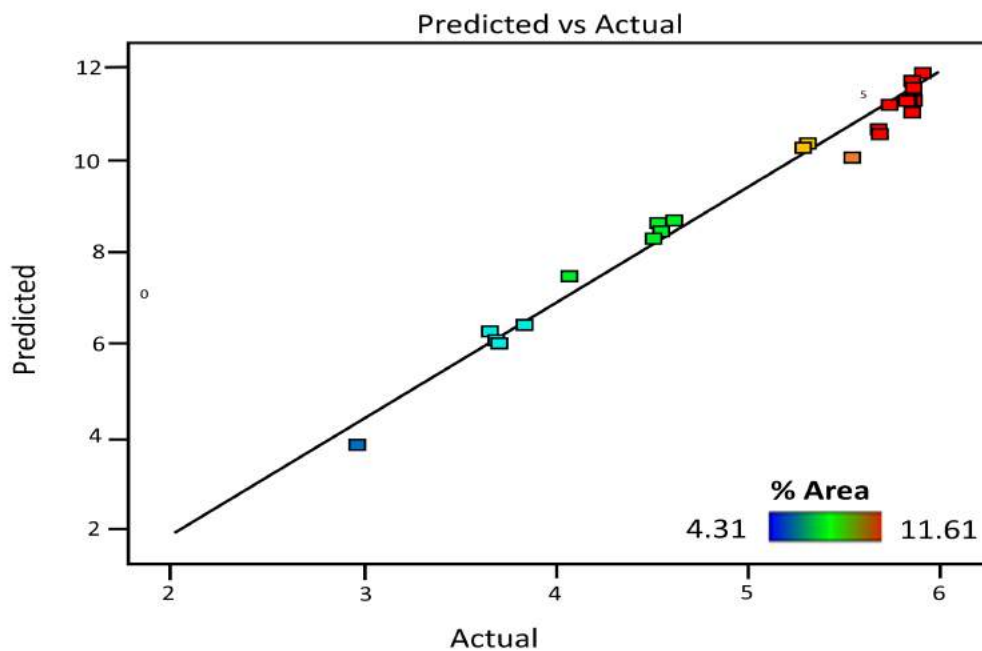


Fig 3.8: Dissipated scatter plot for area fractionues for 2N number of lines

$$\begin{aligned} \frac{1}{D_{index}} = & 5.05 + 0.1436 A + 0.1193 B + 0.0816 C + 0.0393 D - 0.0006 AB \\ & + 0.0946 AC - 0.0224AD + 0.0076 BC + 0.0041 BD - 0.0092 CD \\ & - 0.9074 A^2 - 1.59 B^2 - 0.1947 C^2 - 0.1443 D^2 \end{aligned} \quad (3.7)$$

$$\begin{aligned} Area\ fr. = & 11.17 + 2.69 A + 1.36B + 0.1608C + 0.0592D - 0.5175AB + 0.04AC \\ & - 0.07AD - 0.0275BC - 0.0425BD - 1.92 A^2 - 0.8942B^2 \\ & - 0.4167C^2 - 0.3067D^2 \end{aligned} \quad (3.8)$$

3.4.2 Response surface analysis.

The response surface analysis of D_{index} response concerning various parameters are shown in Fig. 3. 9. The response surface of time and rpm indicates that both the parameters are impactful and the lowest D_{index} is obtained on a combinatorial value within the range. The reason is this combination provides a mushy mixture which homogenizes the particles in the aluminium matrix. The response surfaces of the Time and furnace temperature suggest that minimum value of furnace temperature is attained at a specific combination. This tendency is also related to the attainment of the mushy zone, i.e. if the furnace temperature is high, then the liquid state will result in a density difference which will hinder the stirring action. Also, it is clear that in order to achieve a low D_{index} , RPM is having a dominating effect as compared to the other parameters. The response surface analysis of area fraction (% Area) in reference to various parameters are shown in Fig. 3.10. Area fraction also denotes the volume fraction of the particles into the matrix and thus represents the mixing quality of stirring action. The response of the RPM vs Time suggests that the increase in RPM and Time of stirring increase the area fraction of particles in the composite due to better mixing of the particles into the aluminium matrix. The

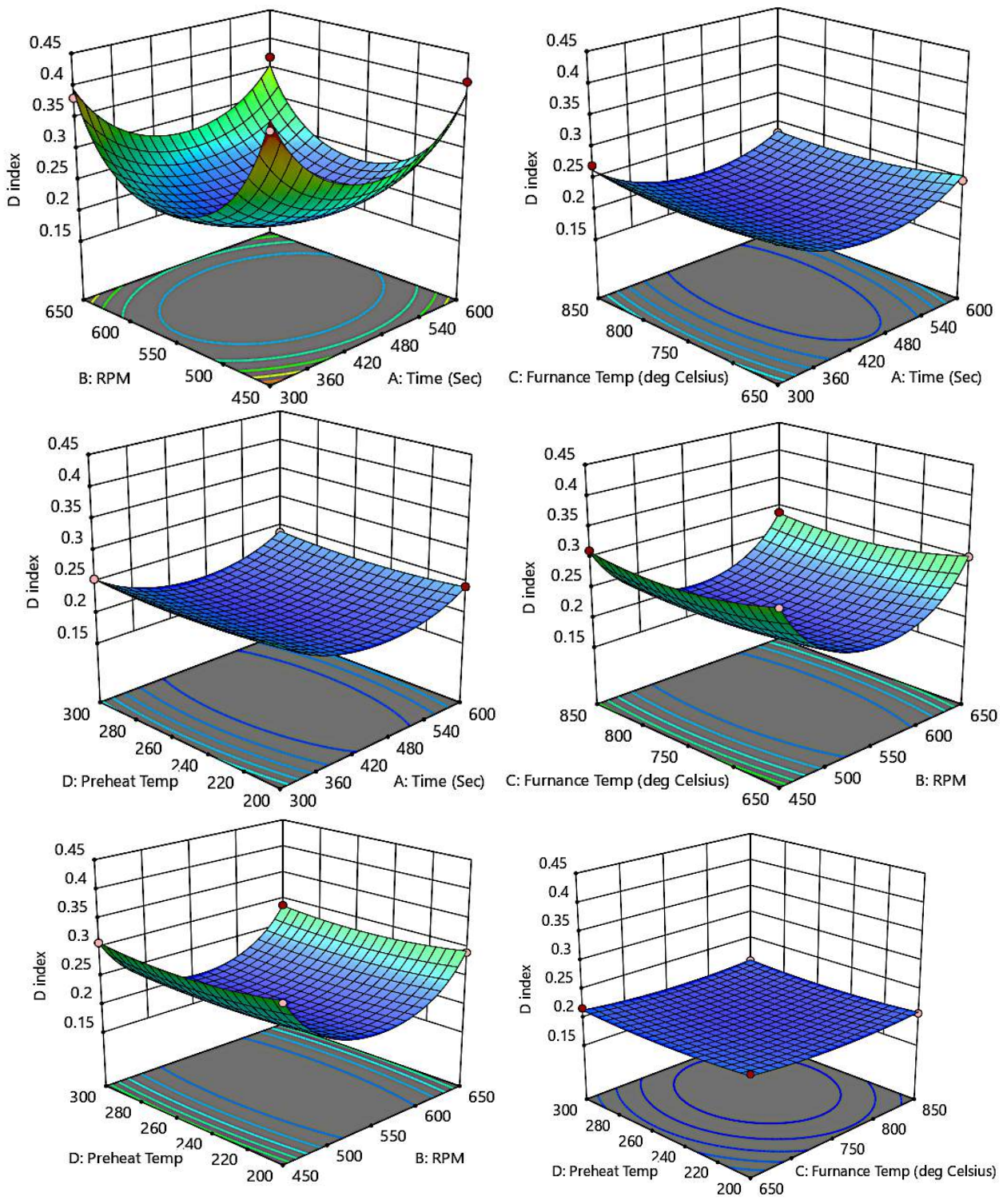


Fig 3.9: Response surface analysis of D_{index} vs various parameters
 response surface of the furnace temperature and Time of stirring indicate that in order to achieve higher area fraction, the furnace temperature should not be the highest. If the furnace

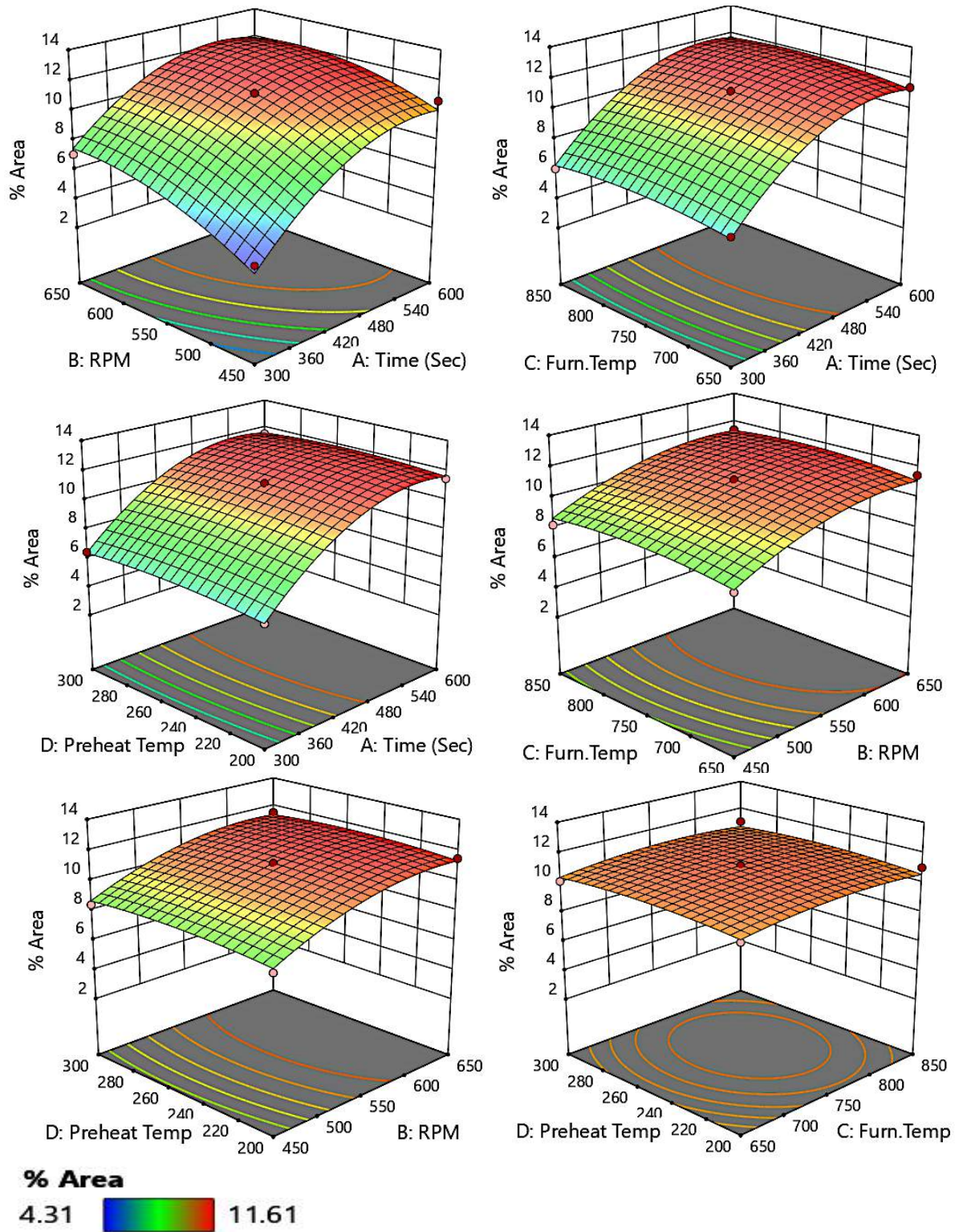


Fig 3.10: Response surface analysis of Area fraction vs various parameters

temperature is higher than the Time of stirring should also be increased up to a specific limit. Similarly, RPM is also the dominant factor when compared with preheat temperature and furnace temperature.

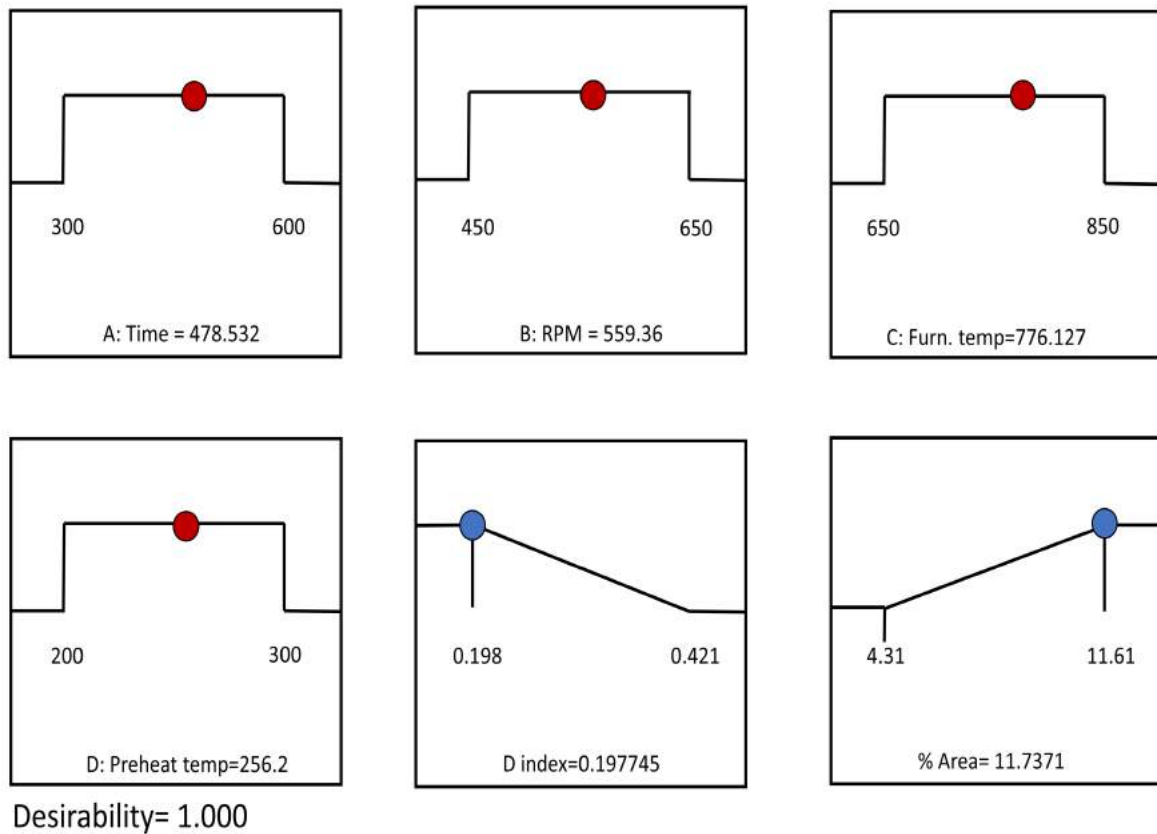


Fig 3.11: Optimal parameters and the response at these values

The leading observation that can be derived from these results is that combination of furnace temperature, stirring Time, stirring rpm and preheat temperature should be in a manner that while pouring, the melt should be in the semi-solid state. If the melt is in a purely liquid state, then the particles will not be incorporated significantly in the aluminium alloy and also stirring action will not be effective in homogenizing the particles.

3.4.3 Solution and validation

The multi-objective optimal solution for maximum area fraction and minimum D_{index} is obtained, as shown in Fig. 3.11. The area fraction is prioritized to the D_{index} with a ratio of 5:4. The optimal parameters for lowest D_{index} and highest area fraction are obtained as- (1) Time of stirring = 478.5 seconds, (2) RPM= 559.36, (3) Furnace temperature= 776.12°C, (4) Preheat Temperature= 256.2°C. The response at these parameters are $D_{index} = 0.197$ and area fraction

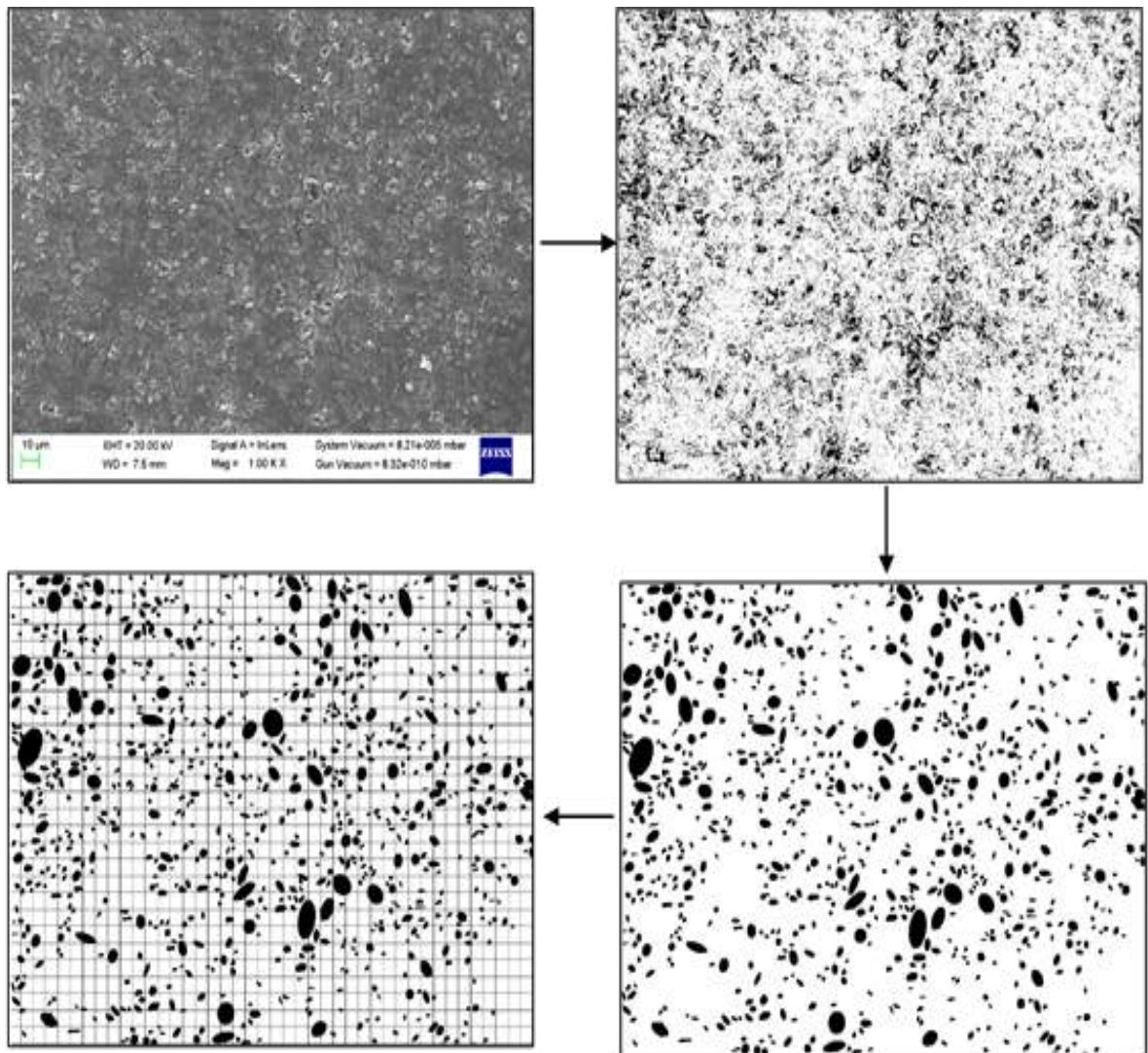


Fig . 3.12: Image analysis of composite fabricated at optimized parameters

=11.73%. The confirmation test of optimization provided a range of 0.185-0.209 for D_{index} and 10.5 -12.96% with a 95% confidence level.

The results are validated by fabricating the composite by taking optimized parameters for stir casting process and evaluating the responses. Since experimental variation pertains to exist, three samples are taken for analysis and the average value of the values are chosen for comparison. One example of the image analysis of the composite fabricated at these parameters is shown in Fig. 3.12.

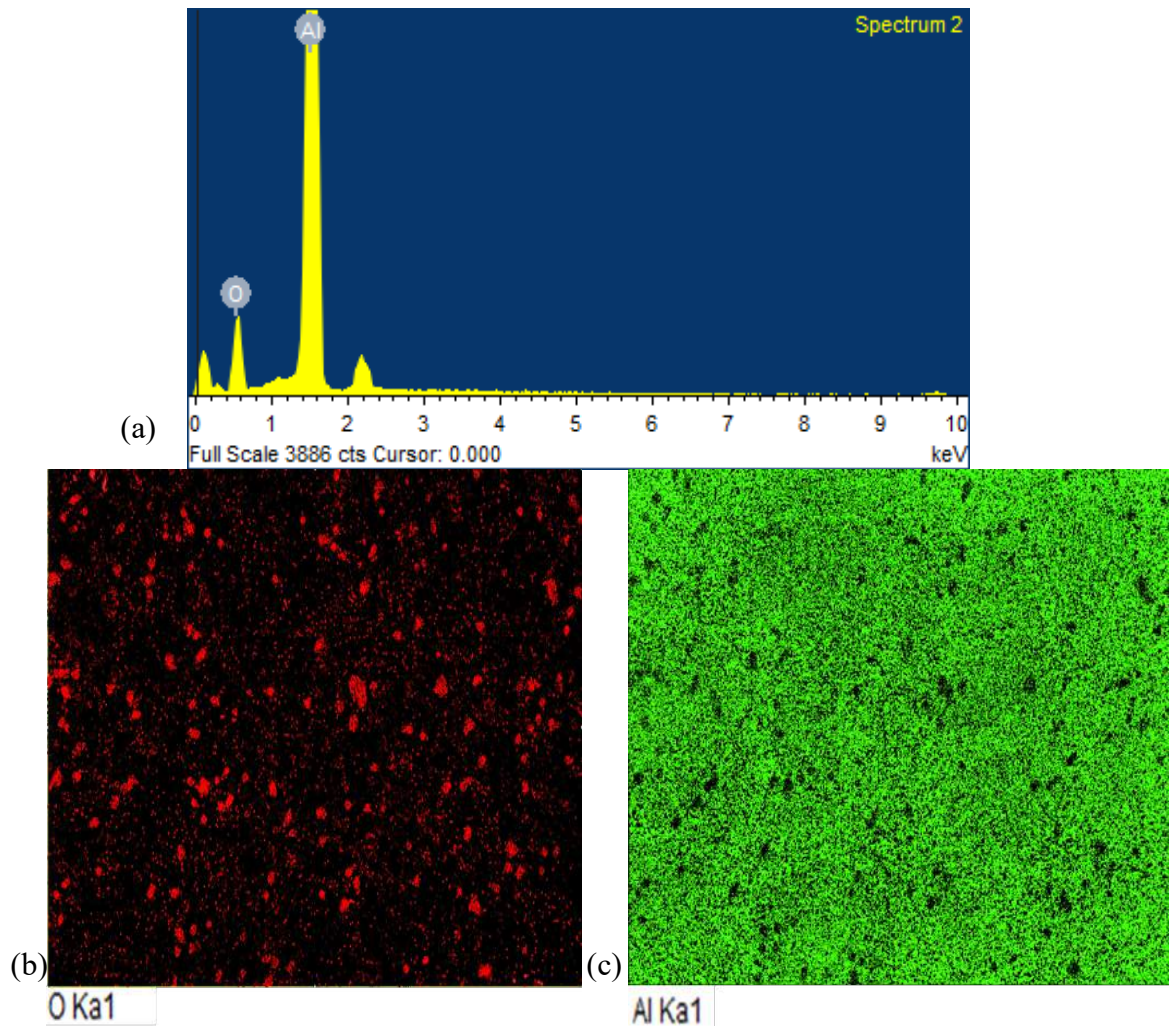


Fig 3.13: EDS analysis of the composite and EDS maps with (b) the distribution of oxygen (O Ka 1) and (c) the distribution of aluminium (Al Ka 1)

The value of D_{index} response for this case converged at $2N= 128$ lines is 0.196 , and the area fraction is 11.84% . The average value of D_{index} and area fraction is 0.203 and 12.14% . The comparison of average experimental values and model range values is shown in Table 3.6. The average value is within the range of the confirmation test. Therefore, it can be concluded that the optimization of the process parameters is appropriate.

Furthermore, EDS analysis of the composite is also performed to confirm the presence of alumina particles, as shown in Fig. 3.13. In Fig. 3.13(a), peaks of aluminium and oxygen confirms the presence of alumina and aluminium. Although, distribution within the samples is shown in the EDS maps of oxygen and aluminium. Fig. 3.13 (b) shows the distribution of

Table 3.6 Comparison of confirmation test range and experimental value at optimised parameters

Process parameter	Value	Model D_{index}	Experimental D_{index}	Model % area	Experimental % area
Time	478.53				
RPM	559.36				
Furnace temperature	776.12	0.197 ± 0.012 (0.185 -.209)	0.203	11.73 ± 1.23 (10.5 -12.96)	12.14 %
Preheat temperature	256.2				

Oxygen (O Ka 1), where the traces of O (red dots) in the micrograph EDS map is mainly due to Al₂O₃ and SiO₂. However, the concentration of red dots confirms the presence and distribution of alumina particles. Similarly, Fig. 3.13(c) represents the distribution of Aluminium (Al Ka 1) in the matrix. A high noise level in EDS maps makes it unsuitable for binary representation, but it can be manually observed that EDS maps replicate the binary image as shown in Fig. 3.12 with some error due to misinterpretation of pores to particles during binary conversions.

These error points are discovered by close manual observation, as shown in Fig 3.14, which highlights the porosity junctions selected by comparing EDS maps with the binary image. These pores might be induced during stir casting process and due to the removal of particles during the EDM wire cutting process (since small samples limited to 10 mm dimension were required for SEM analysis). So, it can be considered as future scope of this work where this error can be reduced by binary conversion of EDS maps. For converting the EDS maps into binary images, the noise level of the EDS maps must be less, and it is suggested that it can be achieved by using SEM images with high magnification.

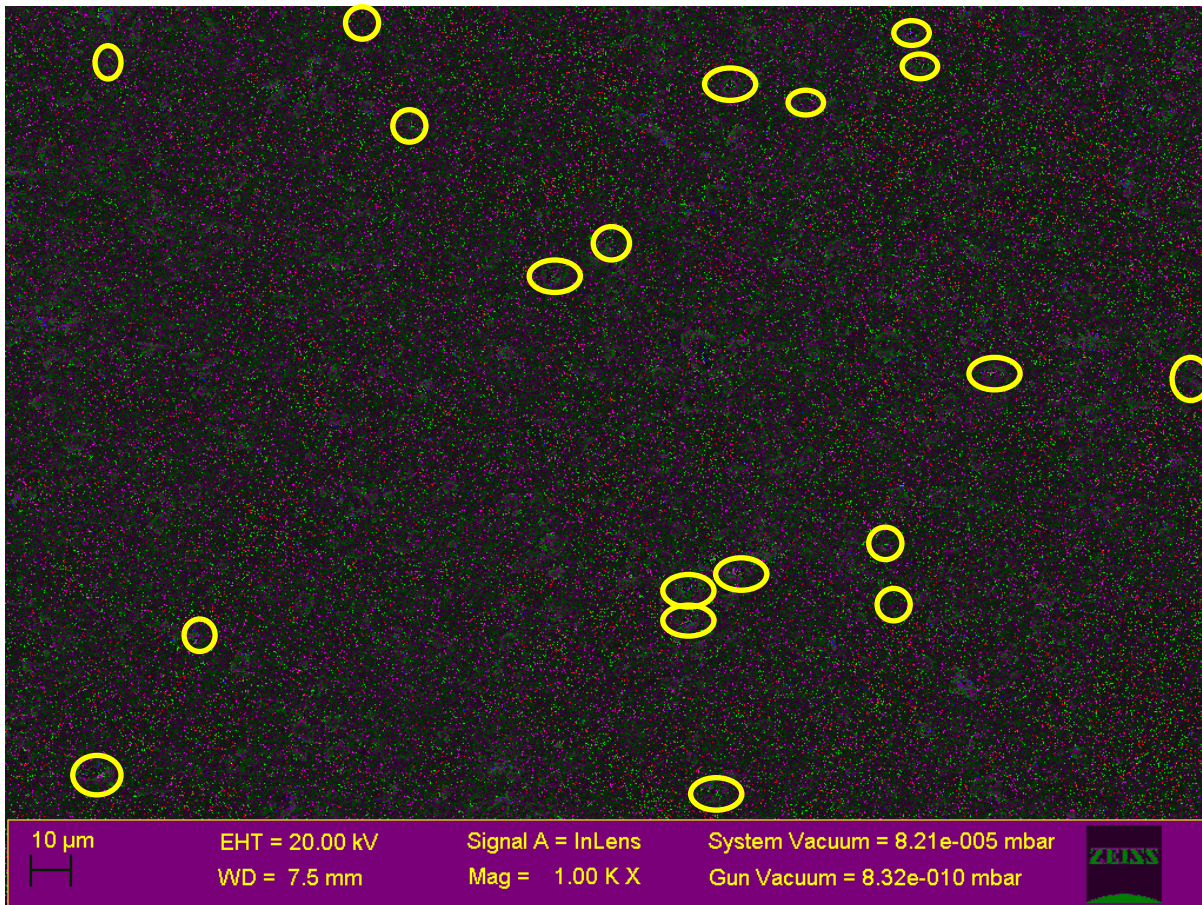


Fig. 3.14: Pores observed in the composite material matrix

3.5 Summary

The composite material was fabricated successfully by stir casting route. The parameters of stir casting were optimized by quantitatively analysing the SEM images. The homogeneity and area fraction of the composites was analysed through an image analysis method. The quantitatively assessed homogeneity factor (D_{index}) and area fractions were determined. Response surface methodology based on Box-Behnken design was employed for optimising the stir casting process parameter for maximum area fraction and minimum D_{index} .

The research work can be summarised with the following observations:

- The experimental response values of D_{index} were significantly fitted as an inverse function and area fraction as a direct function for the quadratic equation model.

- The ANOVA analysis confirms the significance of the model, with a 99.99 % confidence level.
- Stirring RPM and stirring time are more significant as compared to the furnace temperature and preheat temperature for D_{index} and area fraction.
- The following optimum parameters were successfully determined by using Box-Behnken design: (1) Time of stirring = 478.5 seconds, (2) RPM= 559.36, (3) Furnace temperature= 776.12°C, (4) Preheat Temperature= 256.2°C.
- A significant improvement was obtained for responses at optimised parameters due to the formation of semi solid-state of melt. This state results in both better homogeneity and incorporation of particles in the melt.
- The presence of alumina particles was confirmed by EDS analysis.
- The average experimental values of D_{index} and area fraction were 0.203 and 12.14% respectively, which is within the range of confirmation test with a confidence level of 95%.
- EDS maps replicate the binary image with some error due to misinterpretation of pores to particles during binary conversions.
- By optimising these parameters of stir casting route various composites of the required sizes were fabricated and characterized.

Next chapter illustrates the characterization of the metal matrix composite material fabricated through stir casting route.

Characterization of Metal Matrix Composite

4.1 Optical Microscopy

Optical microscopy is suitable for the observation of the grain structure of the composites. Clear images up to the magnification of 200X can be obtained through optical microscopy. It is performed through Olympus GX41 compact inverted metallurgical microscope available at Metallurgy Lab, Delhi Technological University.

The samples were treated and prepared for the proper characterization of the material. The samples of the composite were held along the cross-section by a mounting prepared around the specimen. This mounting was prepared by hot pressing the bakelite powder at a temperature of 140°C for 20 minutes. Once the mounting with the samples was air-cooled, they were again pressed by the mounting press for 15-20 minutes. The topmost surface that was considered for the microscopic analysis was prepared for the analysis. In the very first step, the surface was dry polished using different grades of emery paper to smoothen the rough surface. The range of different grit sizes that were sequentially used for polishing is from P100 to P2500. For further polishing of the wet polishing was used, where velvet emery paper was used with wet alumina powder. The surfaces of different samples were cleaned and then dried with the help of a hot air blower. An etching reagent is essential for revealing the microstructure of the composite material through a selective chemical attack. The etching process is the removal of the highly deformed thin layer that would have been introduced during dry and wet polishing. Keller's reagent is compatible with the aluminium samples and has been used as an etching

reagent. The reagent by mixing 1ml Hydrofluoric acid (HF), 1.5 ml hydrochloric acid (HCL), 2.5 ml nitric acid (HNO₃) and water for 20 seconds. After etching with Keller's reagent, the samples were allowed to dry using a hot air blower and seen under an optical microscope.

4.2 Scanning Electron Microscopy

The magnification scale of 500-1000K is used for analyzing the morphology of the composite material. At this scale of magnification, the particle composition, distribution and homogeneity can be observed. Scanning Electron Microscopy (SEM) is capable of providing high-class images up to this scale of magnification. The primary beam of electrons is generated by an electron gun that falls on the surface of the specimen. The reflection of electrons produces a secondary beam that contains the information of the surface composition and morphology.

The sample image is generated by measuring the low energy secondary electron emission as a function of the position of the primary scanning beam. For composites, it is helpful in determining the particle distribution, size and shape of the reinforcements. The SEM consists of an electric field emission gun that enhances the thermionic emission of tungsten and lowers

Table 4.1 Essential Specification: EVO 50

Properties	Description
Magnification	5X to 1,000,000X
Field of View	6 mm at the Analytical Working Distance (AWD)
Acceleration Voltage	0.2 to 30 kV
Resolution	2.0nm@ 30kV
X-ray Analysis	8.5 mm AWD and 35° take-off angle
Available Detectors	<ul style="list-style-type: none"> • SE in HV - Everhart-Thornley • SE in VPSE • BSD in all modes - quadrant semiconductor diode

the work function. A coherent thin electron beam with high brightness and current density is generated through a field emission gun. The electron probe that is required to interpret the image must be around ten nanometers. It is mandatory to keep the dimensions as small as possible since it is directly influencing the image resolution. This beam of electron covers the entire surface of the specimen through a scanning process known as raster scanning.

The samples of 10mm x 10mm x 10mm were prepared for the SEM analysis. The samples were dry cleaned and no other preparation were required. The specifications of the ZEISS EVO Series Scanning Electron Microscope EVO 50 available at SEM Lab Central Research Facility, IIT Delhi used for SEM analysis are shown in Table 4.1.

4.3 X-Ray Diffraction

X-ray diffraction determines the crystalline nature and the composition of the material and is a powerful tool for the nondestructive characterization of the material. It provides information on preferred crystal orientations (texture), phases, structures, and other parameters related to structure, such as crystallinity, crystal defects, average grain size and strain. The working principle of X-ray diffraction is the interference of the reflected monochromatic X-rays that impinge on the surface of a crystalline sample. A cathode-ray tube produces these X-rays that are filtered, collimated and concentrated before falling on the sample for analysis. Constructive interference occurs within the reflected rays when Bragg's equation ($n\lambda=2d \sin \theta$) is satisfied. Here n is a positive integer, λ is the wavelength of the incident rays, d is the lattice spacing in a crystalline sample, and θ is the incident angle. By scanning the reflected irradiation for all the possible orientation, the characteristics of the material can be analyzed by comparing them to the standard observations. X-ray detector, sample holder and X-ray tube are the elements of which X-ray diffractometers are constituted.

An X-Ray diffractometer of Bruker D8 advanced at Applied Physics department, Delhi Technological University was used and its specifications are shown in Table 4.2. A tungsten or molybdenum filament is heated inside a cathode tube, and it produces electrons. By applying a suitable voltage in a target direction, these electrons are accelerated and bombarded on the specimen surface with high energy. When these high energy electrons fall on the specimen, the inner shell electrons of the atoms of the specimen are dislodged, and characteristic X-ray spectra are produced. K_{α} and K_{β} are the most common spectra and further classified as $K_{\alpha 1}$ and $K_{\alpha 2}$. $K_{\alpha 1}$ have high energy states and therefore have a short wavelength and high intensity as compared to $K_{\alpha 2}$. The wavelength of the corresponding characteristic spectra is a signature of the material, whether it is copper, molybdenum or chromium. Crystal monochromators or foils are used for filtering the X-rays. These filtered X-rays are then collimated and directed towards the direction of the specimen. The intensity of the reflected X-rays is recorded for all the directions by rotating the sample holder and the detector. The direction at which Bragg's equation is satisfied gives a peak due to the constructive interference. This X-ray signal is recorded, processed and converted into a count rate. A detector records and processes this X-ray signal and converts the signal to a count rate which is then output to a device such as a printer or a computer monitor. When the sample in the X-ray diffractometer rotates at an angle θ , the detector rotates at an angle of 2θ to collect the diffracted X-rays. It maintains this position and is rotated with the goniometer, which provides the precision of rotation. Copper is the most common target material for single-crystal diffraction, with CuK_{α} radiation = 1.5418\AA . This X-Ray diffractometer is very suitable for the composition analysis of the composite. The presence of the particles in the composite can also be determined by utilizing this technique. The reinforcement in the composite will have a different characteristic spectrum that can be detected in the XRD plot.

Table 4.2 X-Ray Diffraction machine specification

X-Ray	
Running Condition	Voltage = 40 kV and Current = 40 mA
Source	Long fine focus ceramic X-ray tube with 2.2 kW Cu anode
Goniometer	
Angular range (Theta)	-5° to 40°
Angular range (2Theta)	-10° to 60°
Smallest angular step size	0.0001°
Reproducibility	+/- 0.0001°
Maximum and minimum measurement circle diameter	250 mm & 100 mm
X-ray Beam Shaping Optics	
Beam [Cu-K _{α1}]	Collimated, compressed and frequency filtered by a Göbel mirror and V-Groove
Collimated beam dimensions	0.3 mm by 11 mm
Gobel mirror	60 mm multilayer X-ray mirror on a high precision parabolic surface
Detector	
Maximum count rate	$2 \times 10^6 \text{ s}^{-1}$
Detector electronics count rate	$3 \times 10^7 \text{ s}^{-1}$

4.4 Residual Stress

The stresses are induced in the material when a load is applied to the material. Generally, if the load is removed, then stress is also removed from the material. However, there is some stress left in the material in many cases due to the mismatch and disorders within the material. After removing the original load, these stresses remain in the solid material and are termed as residual stresses. These stresses may be undesirable or desirable for a specific application depending on the nature of the material and type of application.

This behavior is commonly observed in composite materials because of the mismatch in the composition of the material. However, residual stresses can have a considerable impact on the properties of composites and can increase or decrease the material strength depending on the type of fabrication and nature of materials. Since composites have a wide variety of applications in civil infrastructure, aerospace, defense, transportation and other industrial sectors, it is crucial that the residual stresses are measured, interpreted and analyzed correctly.

For the residual stress measurement of the materials, Pulstec μ -X360n Full 2D High-Resolution X-ray Diffraction (HR-XRD) machine available at Precision Engineering Lab, Delhi Technological University. A Pulstec μ -X360n Full 2D High-Resolution X-ray Diffraction (HR-XRD) machine specifications are shown in Table 4.3. The X-Ray tube with Cr filament has a collimator of 1mm diameter and a power requirement of 30 kV X 1mA. This apparatus works on X-Ray diffraction and utilize the $\cos\alpha$ method of the Debye-Scherrer Rings for the measurement of the residual stresses. This process is fast and suitable than the $\sin^2\psi$ technique as in this process goniometer is not required for tilting the specimen/ detector. In the $\cos\alpha$ method, the material is exposed to the X-rays up to 1 μm , and thus it measures the d-spacing and the spacing difference due to anomaly. By using a 2D detector, this measured lattice spacing is collected by Debye ring with a single measurement.

Table 4.3 PULSTEC μ -X360n Specification

Properties	Descriptions
2D Full data of Debye-Scherrer ring	Max. 500 points
X-ray detector	Full 2 D (visual analysis)
Acceleration Voltage	0.2 to 30 kV
Collimator size	ϕ 1 mm (ϕ 0.04 inch)
X-ray tube	30 kV & 1 mA (Safety & Ecology)
Power supply unit weight	6 kg (13.2 lbs)
Cos α line Data	Max. 125 points
Sensor unit weight	4 kg (8.8 lbs) (Z height stage)
Permissible range	+ 5- to -5 mm
Portable	Air cooling, Goniometer not required
Measurement time	90 seconds

The Debye Ring $\cos\alpha$ method is also based on the principle of X-ray diffraction, where it calculates the stress by $\cos\alpha$ diagram in the single exposure. The strain data around the circumference of Debye ring is recorded on the two-dimensional detectors such as Imaging Plates (IP) as shown in Fig. 4.5. For the diffraction angle θ , the strain ε_α at the azimuthal angle α can be expressed as:

$$\varepsilon_\alpha = \frac{\cos^2 2\theta}{2L \cos \theta} (r_\alpha - r_0) \quad (1)$$

where r_α is the radius of the D-S ring at the azimuthal angle, and r_0 is the radius for stress-free crystals. L is the distance between the specimen and the IP. The stress is then determined from the slope of the linear relationship between the ε_α and $\cos\alpha$. The stress measured by X-rays is

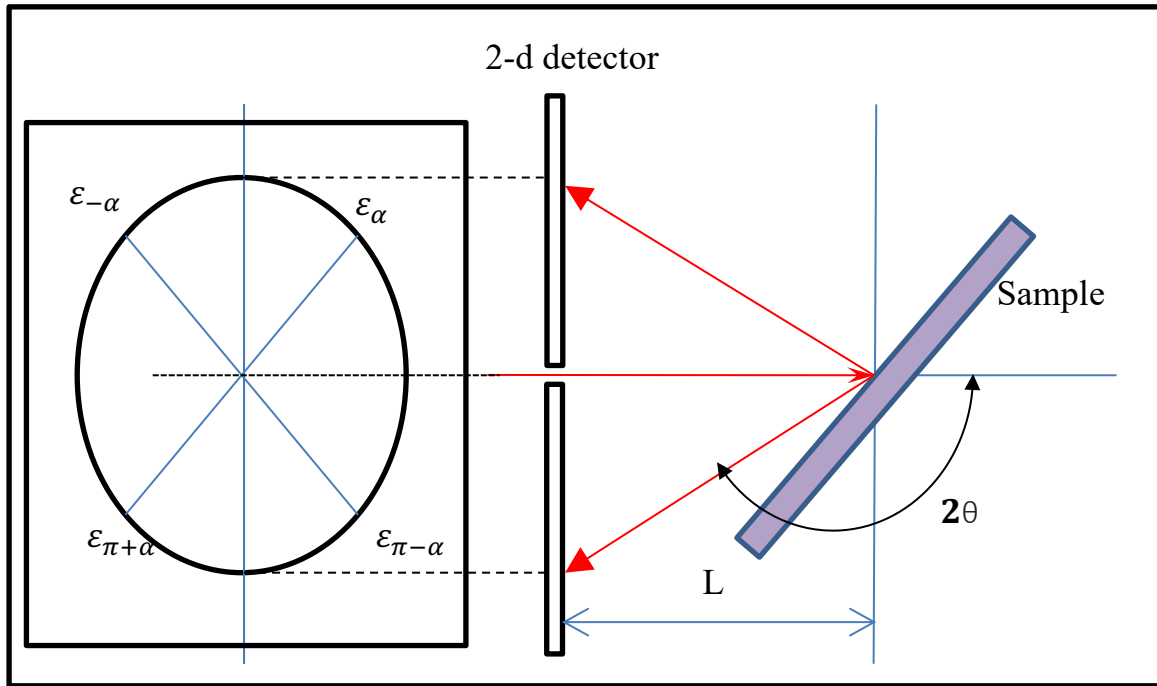


Fig. 4.1: Measurement of strain in Debye-Scherrer ring in $\cos\alpha$ method

the weighted average of the stress distribution within the penetration depth of X-rays below the surface.

4.5 Microhardness

Hardness is the material resistance to localized plastic deformation induced by either mechanical scratches, abrasion or indentation. Microhardness is primarily for the application of thin material with low thickness, such as sheets. It is also used in the case of curved materials which have a specific curvature on the surface. Vickers indenter is used for the microhardness measurement of the specimens. A diamond pyramid with a 136° included angle (Vickers indenter) indents the surface of the specimen, and the corresponding force required is identified, and the microhardness is calculated. Struers Duramin-40 microhardness tester available at SOM Lab, Delhi Technological University is used for analyzing the microhardness, and the technical specifications of the machine are presented in Table 4.4.

Table 4.4 Specification of Microhardness testing machine (Struers Duramin-40)

Properties	Descriptions
Model	Duramin-40 M1
Stages and Turrets	
XY-stage or anvil size (mm)	90 x 90
XY-stage	Manual
Machine weight	101 kg
Motorized Z-axis	Yes
Anti-collision protection	Yes
Motorized turret	Yes
XY-stage stroke, max (mm)	25 x 25
Turret positions	6
Vertical capacity	172
Throat depth (mm)	170
Loads and Applications	
Brinell Capability	Yes
Knoop Capabiblity	Yes
Vickers Capability	Yes
Load Range (Main Loads)	10 gf – 10 kgf
Camera and Optics	
Stage illumination	Yes
Laser or LED guider	Yes
Evaluation camera resolution	18 MP
Auto illumination	Yes
Interfaces and Connectivity	
Operation	15-inch touch screen with Windows 10 PC.
Bluetooth	Optional
Wifi	Yes
Communication Ports	RS232, VGA, RJ45, WLAN, USB, HDMI

The surface was prepared for microhardness testing by following steps:

- The hardness specimen initially dry polishing was implemented via different grade of emery papers (180, 320, 400, 600, 800, 1000, 1200, 1500, 2000 and 2500)
- Then wet polishing is carried out via velvet cloth using different grades (I, II & III) of alumina powder.

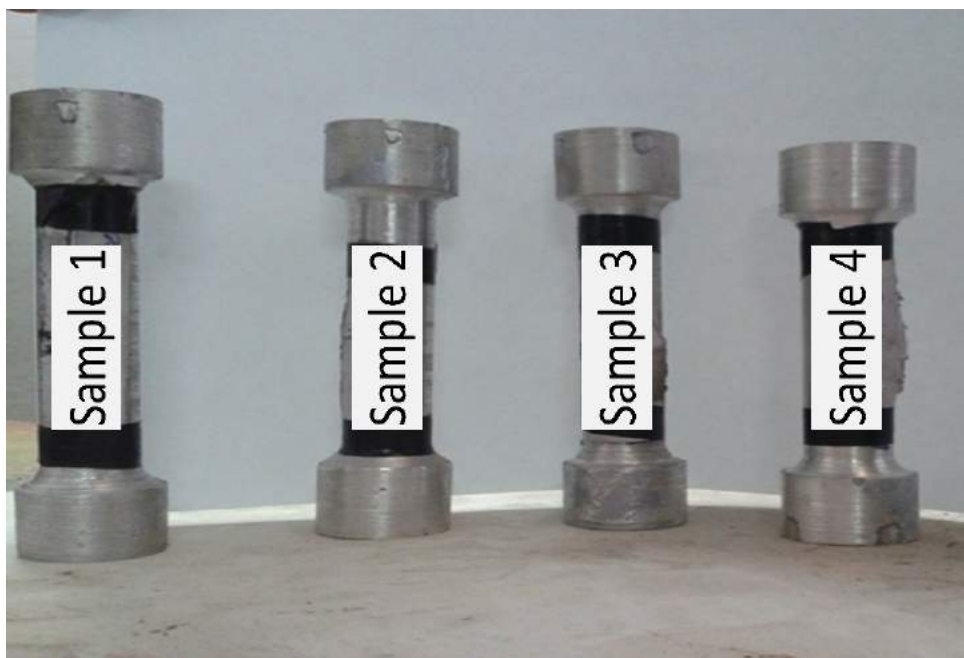
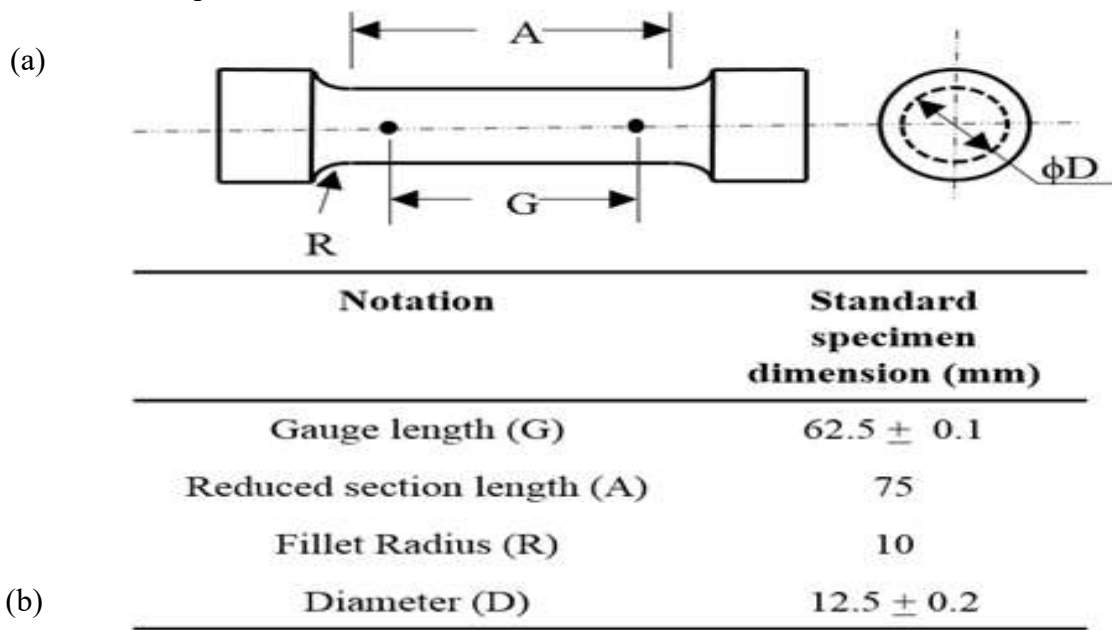


Fig. 4.2: (a) ASTM E8M-04 standard specimen size (b) Composite specimen prepared.

4.6 Tensile Test

The engineering materials must have high tensile strength for their application in various fields. Therefore, it is necessary to attain the values of the tensile strength of a material and it can be measured in an Ultimate Testing Machine (UTM). For composites, tensile strength can be a function of the following factors:

- The volume fraction of the reinforcement
- Properties of reinforcement material
- Distribution of the reinforcement
- Properties of the matrix material
- Type of manufacturing
- Defects in the composites.

Since there are various factors associated with the tensile strength of composites, it is necessary to quantify the value of the tensile strength of these composite materials. Tinius Olsen H50KS

Table 4.5 Tinius Olsen H50KS UTM Specification

Property	Unit	Value
Maximum crosshead travel	mm	1100
Clearance between columns	mm	405
Capacity	kN/Kg	50/5000
Weight	Kg	140
Capacity at maximum speed	kN	25
Jog speed	mm/min	0.001-500
Maximum speed at capacity	mm/min	250
Testing speed range	mm/min	0.001-500
Return speed	mm/min	0.001-500
Dimensions (H x W x D)	mm	1613 x 720 x 500

UTM machine available at SOM Lab, Delhi Technological University was used for the determination of the tensile strength of the composites and the specifications are shown in Table 4.5.

In order to follow ASTM E8M-04 standard, samples must be of the dimensions as shown in Fig. 4.8(a). To conform with the dimensions samples of the shafts were turned on lathe machine and prepared as shown in Fig. 4.8(b). These specimens were clamped between the moving and fixed crosshead of the Ultimate testing machine (UTM). Then the load has been applied by releasing the pressure. The moving crosshead moved in downward direction resulting in a tension in the specimen.

4.7 Density and Porosity

Density measurement of specimens was conducted using gravimetric method/ hydrostatic weighing method as per standard OIML-r111 on a Mettler Toledo weighing balance available at NPL, CSIR, Delhi. At recorded temperature, each specimen was first weighed in air and then weighed in distilled water. Density of distilled water is calculated by an empirical formula given in equation Eq. (1)

$$\rho_1 = 0.99997495 \left[1 - \frac{(t - 3.983035)^2(t + 301.797)}{522528.9 \times (t + 6934881)} \right] \quad (1)$$

Here t: Recorded temperature in °C

Density of each test specimen was obtained by Eq. (2).

$$\rho_t = \frac{(I_{ta} \times \rho_l) - (I_{tl} \times \rho_a)}{(I_{ta} - I_{tl})} \quad (2)$$

Here ρ_t : Density of test specimen at recorded temperature

ρ_l : Density of distilled water at recorded temperature

ρ_a : Density of air at recorded temperature

I_{ta} : Weight of test specimen in air at recorded temperature

I_{tl} : Weight of test specimen in distilled water at recorded temperature

Theoretical densities of synthesized hybrid composites were computed by using mixture rule as explained by Eq. (3).

$$\frac{1}{\rho_c} = \frac{1}{\rho_{fa}} \left(\frac{w_a}{w_c} \right) + \frac{1}{\rho_m} \left(\frac{w_m}{w_c} \right) \quad (2)$$

Here ρ_c and w_c : Density and weight of composite

ρ_a and w_a : Density and weight of Alumina particles

ρ_m and w_m : Density and weight of Al 6061 matrix

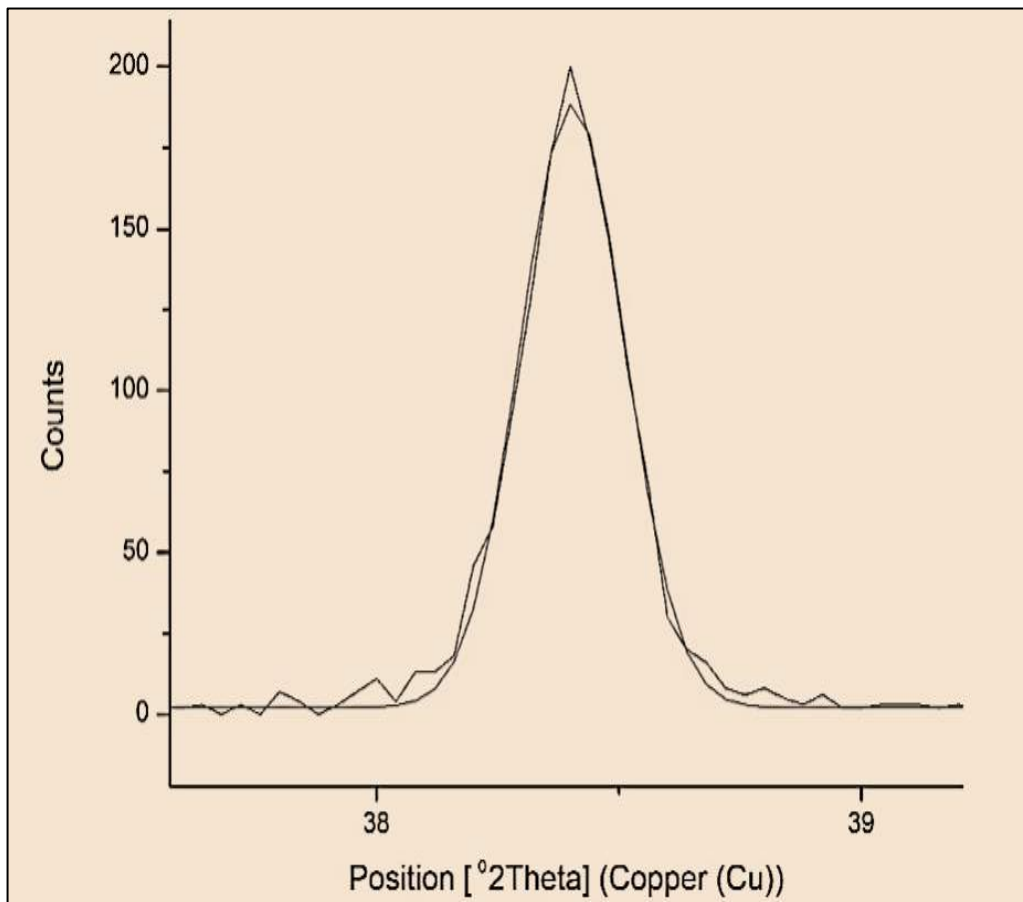


Fig. 4.3: Gaussian fit for peak at [°2 Theta] = 38.4035

Porosity is described as the volume fraction of voids in materials due to independent air bubbles, moisture on reinforcement surfaces, air enveloping reinforcement particles, shrinkage during solidification and water vapours from atmosphere etc. Percentage porosity of developed composites was calculated by expression given in Eq. (4).

$$\% \text{ Porosity} = \left\{ \frac{(\rho_c - \rho_t)}{\rho_c} \right\} \times 100\% \quad (4)$$

Here ρ_c : Theoretical density of composites

ρ_t : Experimental density of composites at recorded temperature ($t^{\circ}\text{C}$)

4.8 Results and Discussions

4.8.1 Microstructure and composition analysis

The optical micrographs with a magnification of 200X were obtained by an inverted light GX41 OLYMPUS microscope. Since particles distribution cannot be confirmed through optical microscopy due to the small size of particles, Scanning Electron Microscopy (SEM) images were analyzed for the confirmation of particle distribution in the aluminium matrix. ZEISS EVO Series Scanning Electron Microscope EVO 50 was used to perform SEM of composite samples. To further confirm the composition and constituents of composites, XRD patterns were analyzed. Full width at half maximum (FWHM) was calculated by Gaussian peak fitting method using Origin software, as shown in Fig. 4.9.

The d spacing was then calculated by using Debye Scherrer equation as stated below in Eq. (1)

as:

$$d = \frac{0.9 \lambda}{\text{FWHM} \cos\theta} \quad (1)$$

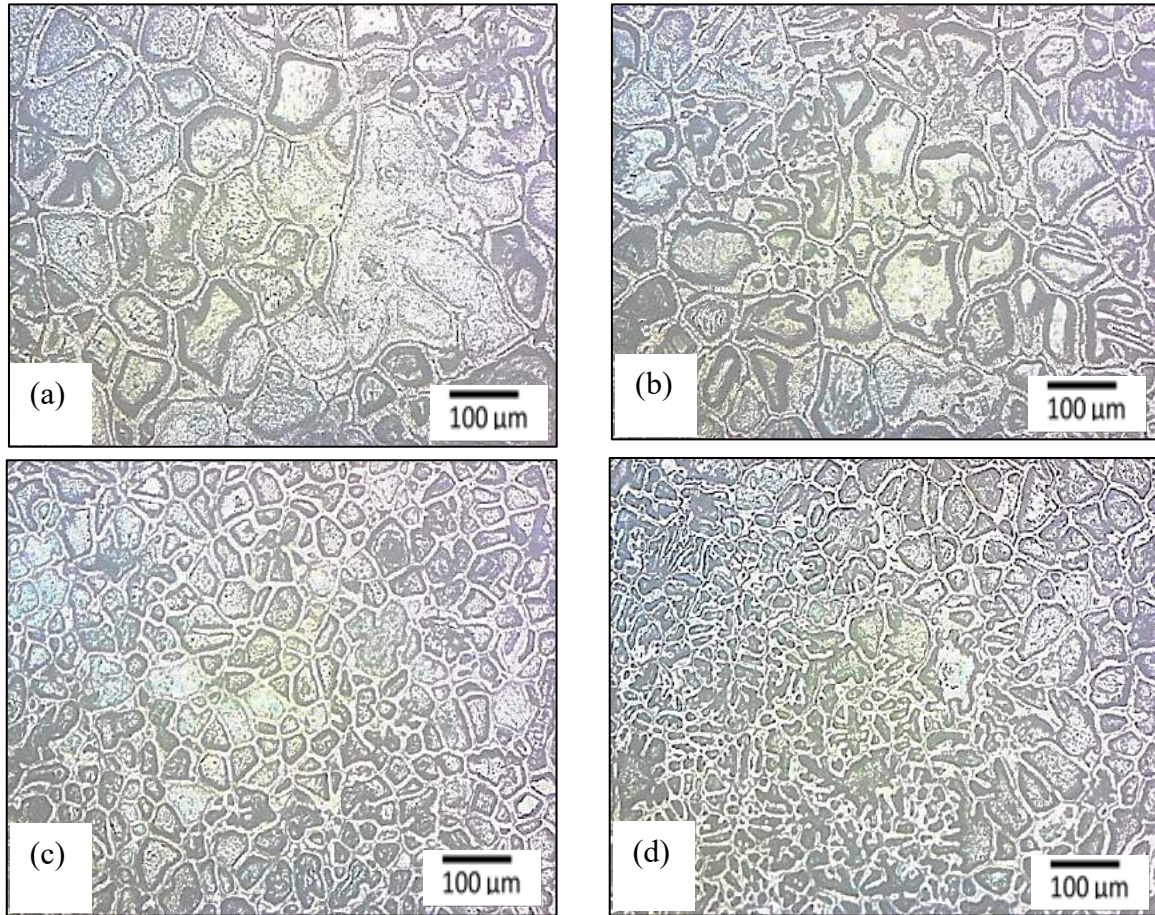


Fig. 4.4: Optical micrograph of (a) Al 6061 (b) Al 6061/6wt.% Al₂O₃ (c) Al 6061/12 wt. % Al₂O₃ (d) Al 6061/18wt.% Al₂O₃.

where d is the d-spacing in Å, λ is Cu wavelength (1.5406 Å), and FWHM is full width at half maximum (into radian), and θ is the position angle.

The optical micrographs of Aluminium 6061 alloy reinforced with 0wt.%, 6wt.%, 12wt.% and 18wt.% of alumina reinforcement are shown in Fig. 4.10. Coarse (micrometric) reinforcing particles induce grain refinement in the Al matrix effectively and subsequently lead to the strengthening of the matrix. As shown in Fig. 4.10, the grain structure of Al 6061 alloy without reinforcement was coarse with large grain size as compared to the composite material.

Addition of reinforcement evidently refined the grain size in composites. This confirms the Orowan strengthening effect of the composites. Even traces of ultrafine grain may be seen in 12 wt.% Al₂O₃/Al 6061 composites.

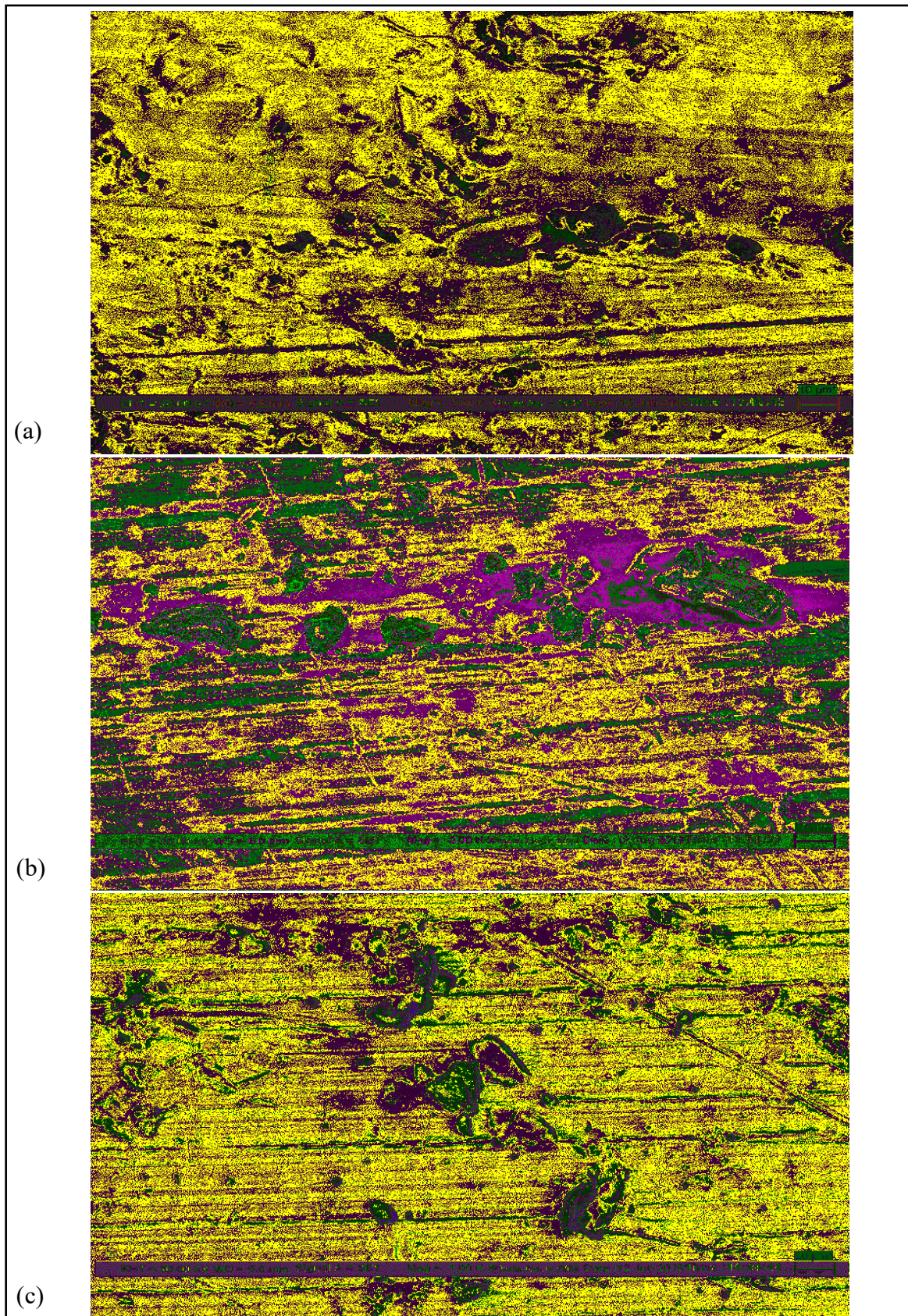


Fig. 4.5: SEM image of (a) Al 6061/6wt.% Al₂O₃ (b) Al 6061/12 wt. % Al₂O₃ (c) Al 6061/18wt.% Al₂O₃.

SEM images of various Al 6061/Al₂O₃ composites are shown in Fig. 4.11. As shown

in Fig. 4.11, alumina particles are embedded in aluminium matrix, and uniform distribution has been obtained for different compositions. The particle size confirms the manufacturer mesh size. The stir casting products have shown uniform and homogeneous distribution of alumina particles in aluminium matrix.

The Al_2O_3 particles in the MMC with more than 18% alumina volume were agglomerated which produced scratches during EDM wire cutting for sample preparation as

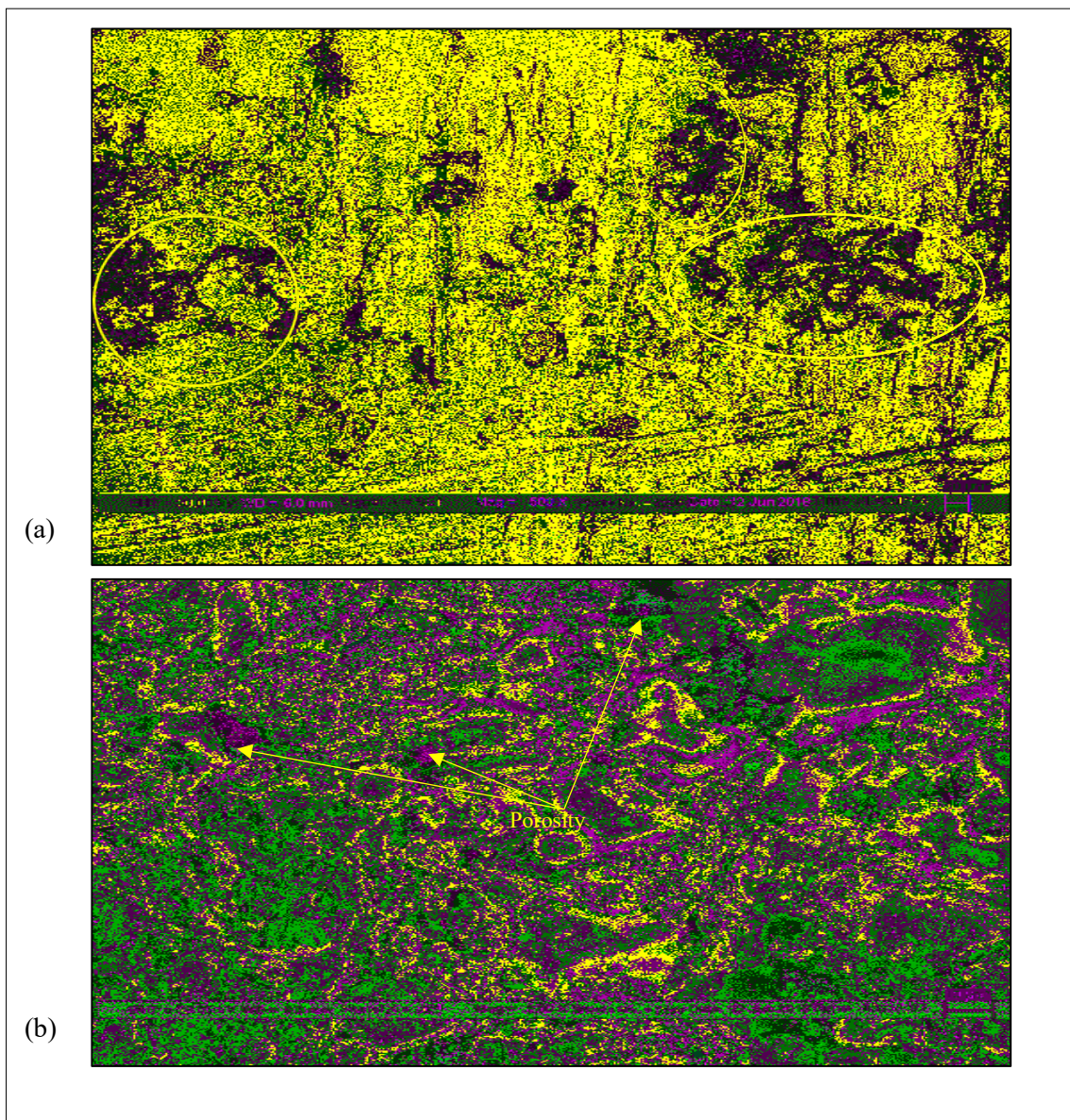


Fig. 4.6: (a) Ruptured and scratched surface due to agglomeration of particle for MMC sample with 24% alumina particle reinforcement at 500X; (b) High resolution image showing porosity induced due to agglomeration at 2000 X.

shown in fig. 4.12(a). In fig. 4.12(b), it may also be noted that porosity is induced in the MMC due to the agglomeration of particles which will further deplete the mechanical properties of the composite. The porosity and the agglomeration of this intensity will subjugate the strengthening effect of composite reinforcement and shall not be taken for further consideration. Therefore, the MMC specimen containing target alumina volume up to 18% was considered for analysis.

The XRD pattern of alumina particle and Al 6061 samples are shown in Fig. 4.13. The Al_2O_3 diffraction pattern depicts peak at various h, k, l planes (012, 104, 110, 113, 024, 116, 214, 300, 220). The peak report comparison has shown 100% relative intensity at position of 43.3630 2 Theta, with d spacing of 2.085 Å (113) and 104 counts. For Al 6061, 100% relative

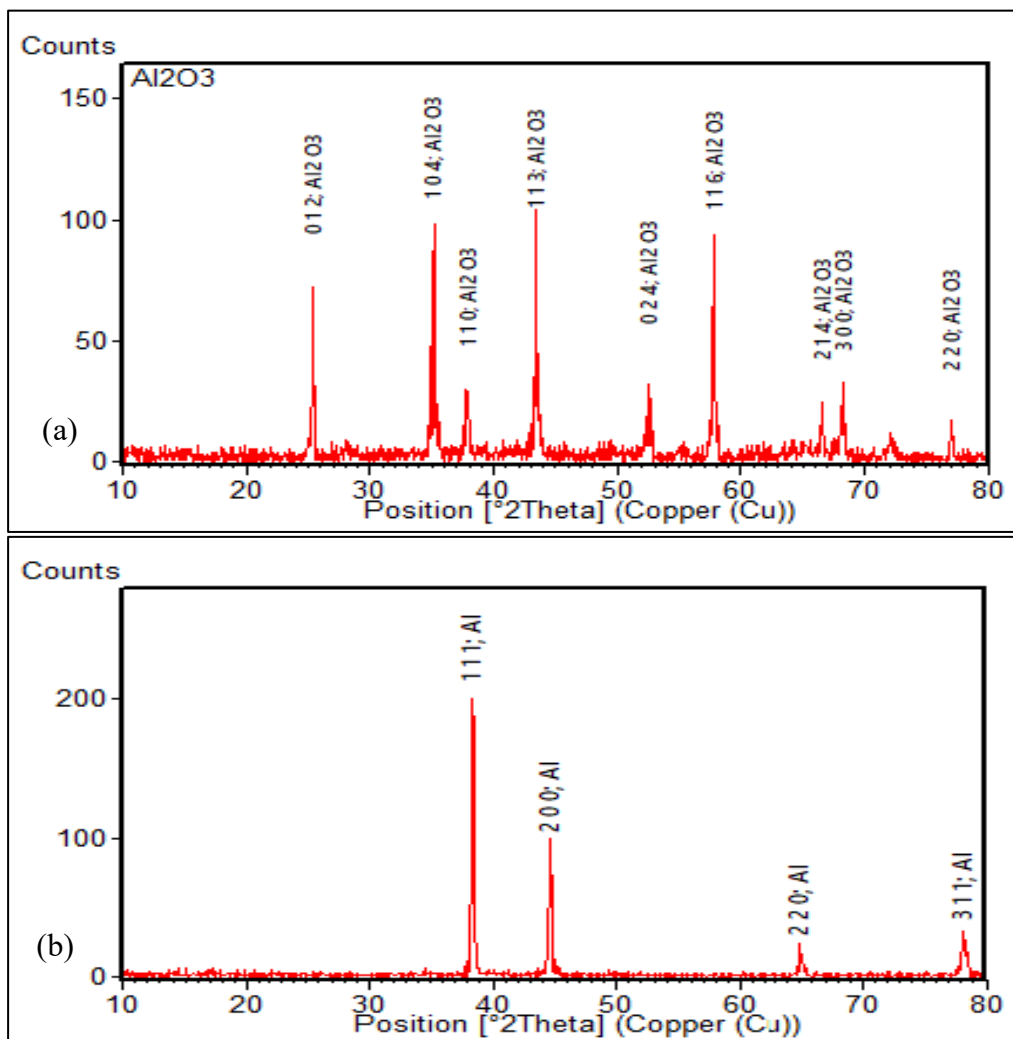


Fig. 4.7: XRD diffraction pattern of (a) Al_2O_3 powder (b) Al 6061 sample

intensity was observed at 38.4035 Pos. [$^{\circ}2\theta$], with counts of 198 and d spacing of 2.314, as shown in Table 4.6.

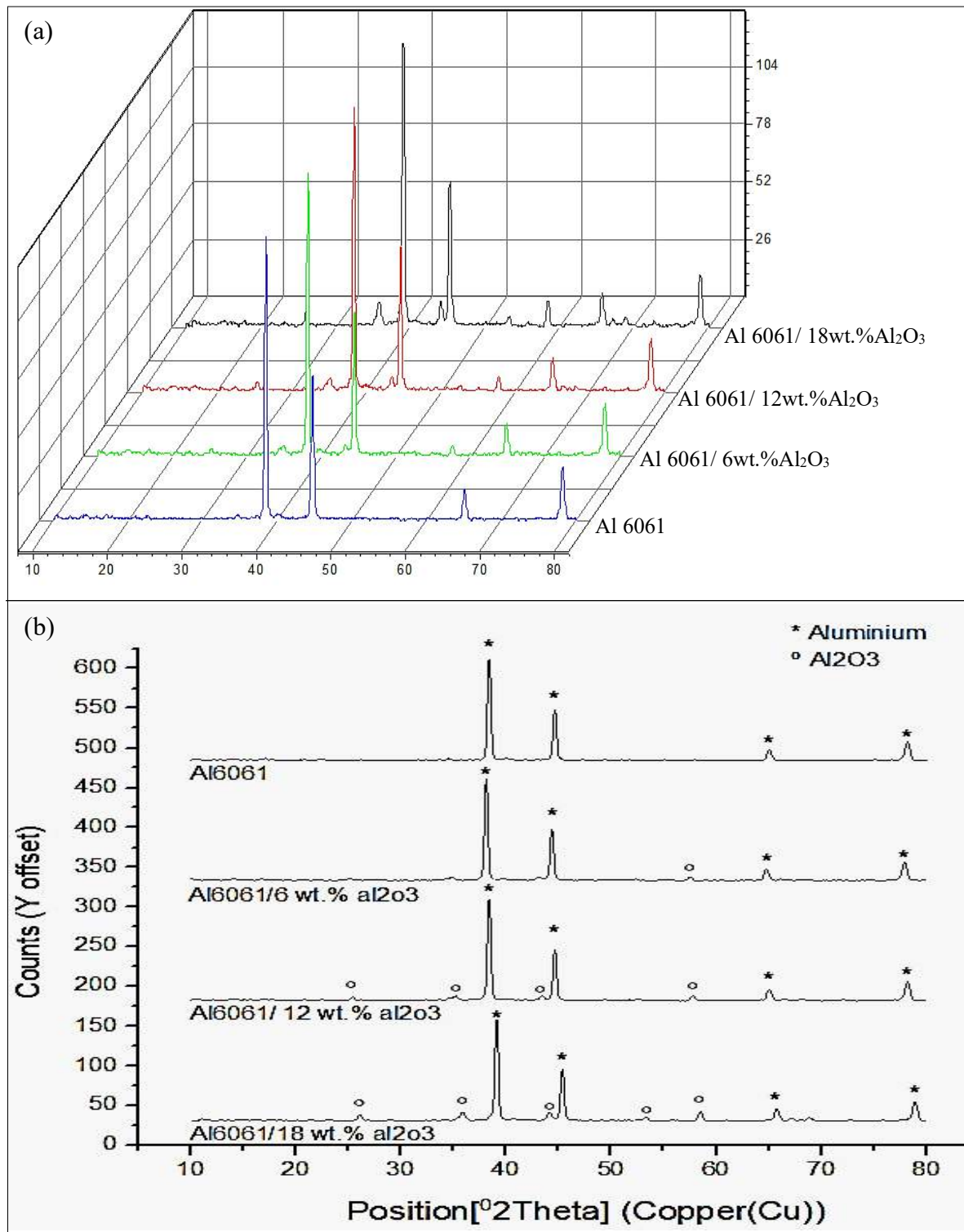


Fig. 4.8: (a) Waterfall model (b) Cascade model of XRD pattern of composites

Table 4.6 Peak report for an Al 6061 alloy

Pos. [2θ .]	Height [cts]	FWHM [radian]	d-spacing [\AA]	Rel. Int. [%]
38.4035	198.30	0.634496	2.314	100.00
44.6671	90.35	0.713122	2.102	45.56
65.0158	16.33	1.071806	1.534	8.24
78.1536	26.60	1.441553	1.239	13.41

The XRD pattern of the composite materials is shown in Fig. 4.13. The XRD depicts the presence of alumina and aluminium for composites. The alumina peaks were visible for a higher concentration of the composites, as shown in Fig. 4.14.

Fig. 4.14 (a) shows a waterfall model and Fig. 4.14 (b) shows the cascade model of the Al 6061 composites with 0wt.%, 6wt.%, 12wt.% and 18wt.% of alumina reinforcement. The presence of components was in conformance with the Powder Diffraction File (PDF) of International Centre for Diffraction Data (JCPDS-ICDD File No. 46-1212 for alumina and JCPDS-ICDD FILE NO. 04-1787 for aluminium).

4.8.2 Residual stress analysis

Residual stress measurements on the test samples were performed on the X-ray residual stress measurement system μ -X360 Ver. 2. 3. 0. 1. using Cr K_{α} radiation which uses Debye Ring $\cos\alpha$ method with Fitting Lorentz approximation method. The surface was chemically etched in a volume proportion of 62:19:19 (phosphoric acid, nitric acid and sulphuric acid) for 5 min at 100°C.

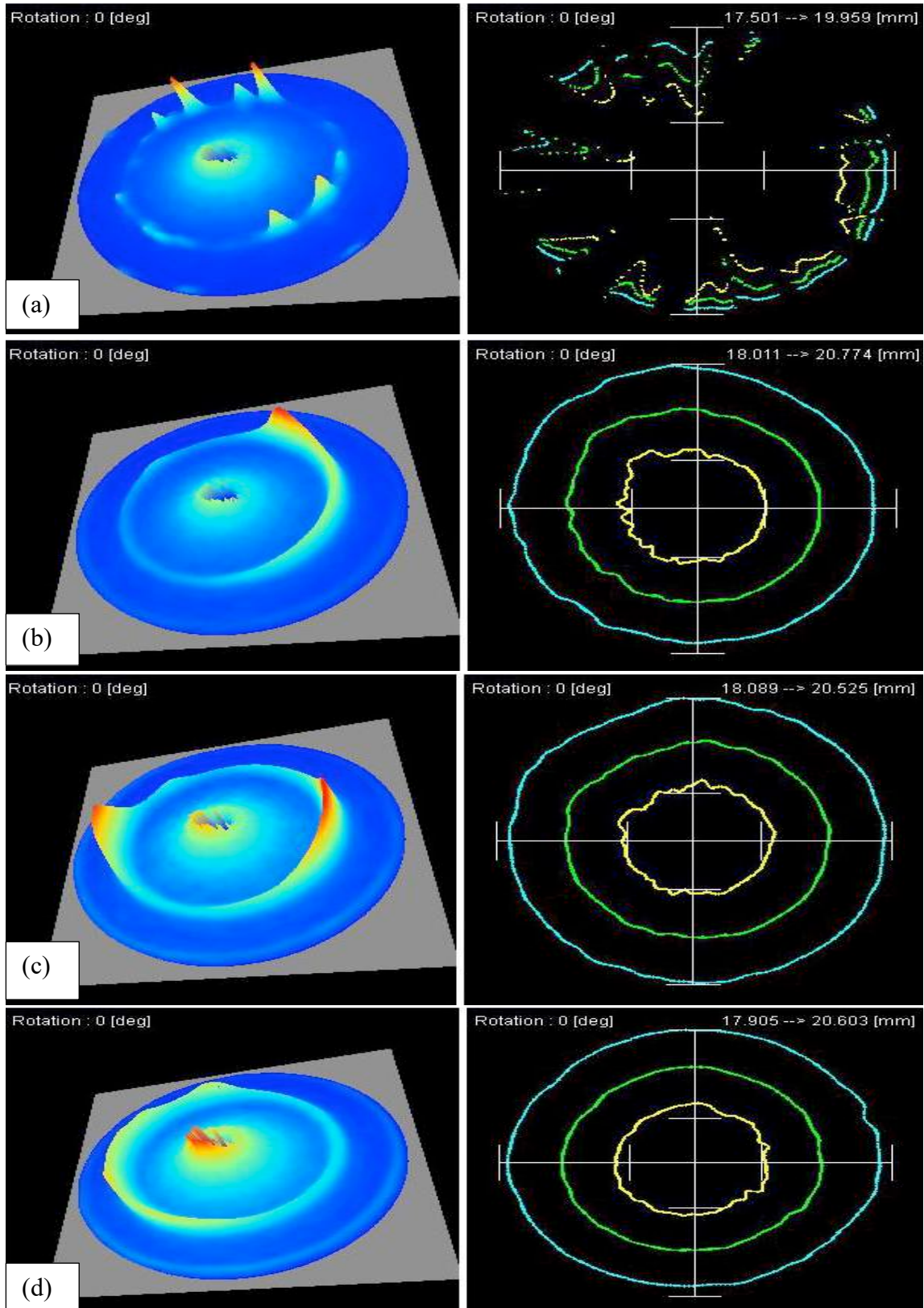


Fig. 4.9: 3D Debye ring and distortion for (a) Al 6061 (b) Al 6061/6wt.% Al₂O₃ (c) Al 6061/12 wt. % Al₂O₃ (d) Al 6061/18wt.% Al₂O₃.

All samples were sent into the analyzer with an X-ray irradiation time of 120 sec, X-

ray tube current 1.00 mA, X-ray tube voltage 30.00 kV, X-ray incident angle 35.0-degree, Cr K_{α} wavelength 2.909 Å.

Three-dimensional diffraction Debye ring profiles and the distortion from each sample are shown in Fig. 4.15. A specific textural pattern within the microstructure resulted in a distorted Debye ring which suggests a coarse grain structure for Al 6061. As shown in Fig. 9, as the reinforcement wt.% increases the Debye ring is more uniform and undistorted, which suggests grain refinement due to the introduction of reinforcements. The nature of residual stress was compressive, and the magnitude of compressive stress increased with wt.% of the reinforcement. The residual stress calculated by using the Debye ring formation is shown in Table 4.7.

Table 4.7 Residual stress for different materials

Material	Residual Stress (MPa)
Al 6061	31
Al 6061/ 6 wt. % Al ₂ O ₃	-72
Al 6061/ 12 wt. % Al ₂ O ₃	-147
Al 6061/ 18 wt. % Al ₂ O ₃	-250

For Al 6061, tensile residual stresses were formed because of non-uniform phase transformations and contraction rates across castings due to different cooling rates at local variable regions. For composites, compressive stresses on the curved surface were induced into the material. The metal matrix composites have two different phases of Aluminum 6061 matrix and alumina reinforcements. These stresses may have been developed because of the mismatch in the thermal coefficient of expansion of reinforcement and matrix.

4.8.3 Microhardness

Struers Duramin-40 is used for analyzing the microhardness of the specimen. The trials were taken for three different samples and at 9 different positions of the respective samples. The outliers were rejected and the average value was considered for the analysis. The average value of the microhardness of the specimens are shown in Table 4.8.

Table 4.8 Microhardness for different materials

Material	Vickers's microhardness (HV 10 kgf)
Al 6061	36
Al 6061/ 6 wt. % Al ₂ O ₃	43
Al 6061/ 12 wt. % Al ₂ O ₃	51
Al 6061/ 18 wt. % Al ₂ O ₃	63

It was observed that the microhardness of the composite was increased by the addition of the alumina reinforcement in the Aluminium 6061 matrix. The hardness of the alumina particles and the refinement of the grain size contributed to the increase in the microhardness of the composites.

4.8.4 Tensile strength

The tensile strength specimens for different composition were tested using Tinius Olsen H50KS UTM machine. The values of tensile strength as observed by tensile test are shown in Table 4.9.

It may be concluded from experimental results as shown in Table 4.8, ultimate tensile strength of elasticity has been increased by increasing the reinforcement volume fraction up to 18% of the composite. However, for 18% Al₂O₃ / Al 6061, tensile strength was reduced as compared to 24% Al₂O₃ / Al 6061 shafts.

Table 4.9 Tensile strength of the specimen

Material	Ultimate Tensile strength (MPa)
Al 6061	142.4
Al 6061/ 6 wt. % Al ₂ O ₃	170.8
Al 6061/ 12 wt. % Al ₂ O ₃	188.8
Al 6061/ 18 wt. % Al ₂ O ₃	198.5
Al 6061/ 24 wt. % Al ₂ O ₃	180.1

The reason may be high level of agglomeration resulting in porosity concentration in the material. This was confirmed earlier through morphological evaluation of the composite materials. The cohesive nature of the alumina particles results in the agglomeration of particles in higher reinforcement volume fraction composites. This reduces strengthening effect of particles in the composites. Also, porosity between the agglomerated particle results in further depletion of these properties.

4.8.5 Density and porosity

The theoretical density is taken as per the actual volume fraction obtained from the image analysis instead of the added weight fraction. Experimentally obtained and theoretically calculated mean values of density for as-cast Al6061 specimen and its composites specimens (mean for three replications) are shown in Table 4.10. It was observed that there was variation in density of composites as compared to the base metal up to 4.2 % due to addition of 18 wt.% of alumina reinforcements.

Table 4.10 Density of the specimen

Material	Theoretical Density (Kg/m³)	Experimental Density (Kg/m³)
Al 6061	2710	2701
Al 6061/ 6 wt. % Al ₂ O ₃	2748	2738
Al 6061/ 12 wt. % Al ₂ O ₃	2798	2788
Al 6061/ 18 wt. % Al ₂ O ₃	2832	2821

Table 4.11 % Porosity of the different materials

Material	Porosity in percentage
Al 6061	0.32
Al 6061/ 6 wt. % Al ₂ O ₃	0.34
Al 6061/ 12 wt. % Al ₂ O ₃	0.35
Al 6061/ 18 wt. % Al ₂ O ₃	0.37

Generally, porosity in composites is increased with infusion of fillers, as particles entering metal matrix trap air and cause voids. To reduce porosity, it is essential to maintain a balance between void sources (features or mechanisms that cause porosity such as moisture layers and trapped air) and void sinks (features or mechanisms that diminish porosity such as bubble mobility and vacuum evacuation) during processing. However, in present experiment utmost care was taken and therefore the porosity has been increased from 0.32% to 0.37% only.

4.9 Summary

This chapter includes evaluation of synthesized composites for different mechanical and physical attributes such as microstructure, composition, residual stresses, microhardness, and tensile strength, in order to conduct a comparative study with unreinforced base metal. The research work can be summarized with the following observations:

- Optical Microscopy revealed a coarse grain structure for Al 6061 alloy. Grain refinement was observed for the composites having high wt.% of reinforcement.
- SEM analysis, along with XRD analysis, confirmed the presence of alumina in the composites.
- Tensile residual stress was observed for Al 6061 surface, whereas compressive residual stress was developed in composites. The magnitude of compressive residual stress was increased due to the introduction of reinforcement into the composites.
- Distorted Debye ring was observed for Al 6061 alloy, which confirms coarse grain and textural pattern. For composites, the uniformity of the Debye increased with the increase of the wt. % of the alumina reinforcements.
- The addition of alumina as reinforcement in the aluminium matrix composite material refines the grain structure.
- Compressive stress on the surface is seen to increase with the addition of alumina particles, which can further restrict surface crack propagation.
- Microhardness was increased due to the increase of the reinforcement in the composite.
- For 24% Al₂O₃ / Al 6061 material, high level of porosity due to agglomeration was observed at microscopic level.
- The effect of agglomeration and porosity lead to the depletion of tensile strength for 24% Al₂O₃ / Al 6061 material.

- Upto 18% Al₂O₃ / Al 6061 material, the porosity increased from 0.32% to 0.37%.

The evaluation and the experimental validation of the effective properties of the metal matrix composite rotor are illustrated in the next chapter.

Computation and Experimental Validation of Effective Properties

5.1 Introduction

5.1.1 Estimation of effective mechanical properties through mean-field homogenization by using parameters extracted through image processing

Cubic samples of 5mm length, 5mm width and 5mm height were processed by EDM wire cutting, and Scanning Electron Microscopy (SEM) micrographs at the magnification of 500X and 1000X were obtained using a Zeiss EVO 50 machine. Morphology of the micrographs depicts uniform distribution of reinforcements in the aluminium matrix. For each composition, three samples were scanned, and the fraction and size of alumina particles were evaluated by image processing and averaged for the computation of effective properties.

The open-source image processing software ImageJ was used to generate binary images of the composites with ellipsoid form, assumed for homogenization of properties. SEM micrographs were converted to binary images by using threshold of 61 foreground pixels and 255 background pixels. This transformed the different luminous pixels into white/black bifurcating with respect to the threshold values. At this value of threshold, particles were easily differentiated from the matrix material. Parameters such as the size of the reinforcement, aspect ratio and volume percentage for the composite were derived from the image analysis, as shown in Fig. 5.1. These parameters were incorporated in the mean-field homogenization of the metal matrix composite material where a Representative Volume Element (RVE) is assumed to be the building block of the macroscopic structure.

RVE is a statistical representation that connects microscopic structure and constituents with the macroscopic properties of composite materials. Therefore, the size of the RVE should be such, that it is aptly smaller than the macroscopic structural dimensions and simultaneously large enough to contain an ample amount of information on the microstructure.

Digimat is a composite modelling platform which has been used for the generation of RVEs with standard size and threshold. It consists of a Digimat-FE tool, which generates realistic RVEs with the finite element method by using the RVE generation algorithm. This algorithm is based on Random sequential adsorption (RSA) technique which randomizes the orientation of the particles. Particles position themselves in random directions sequentially, and each particle blocks nearby locations from being occupied by another particle, therefore

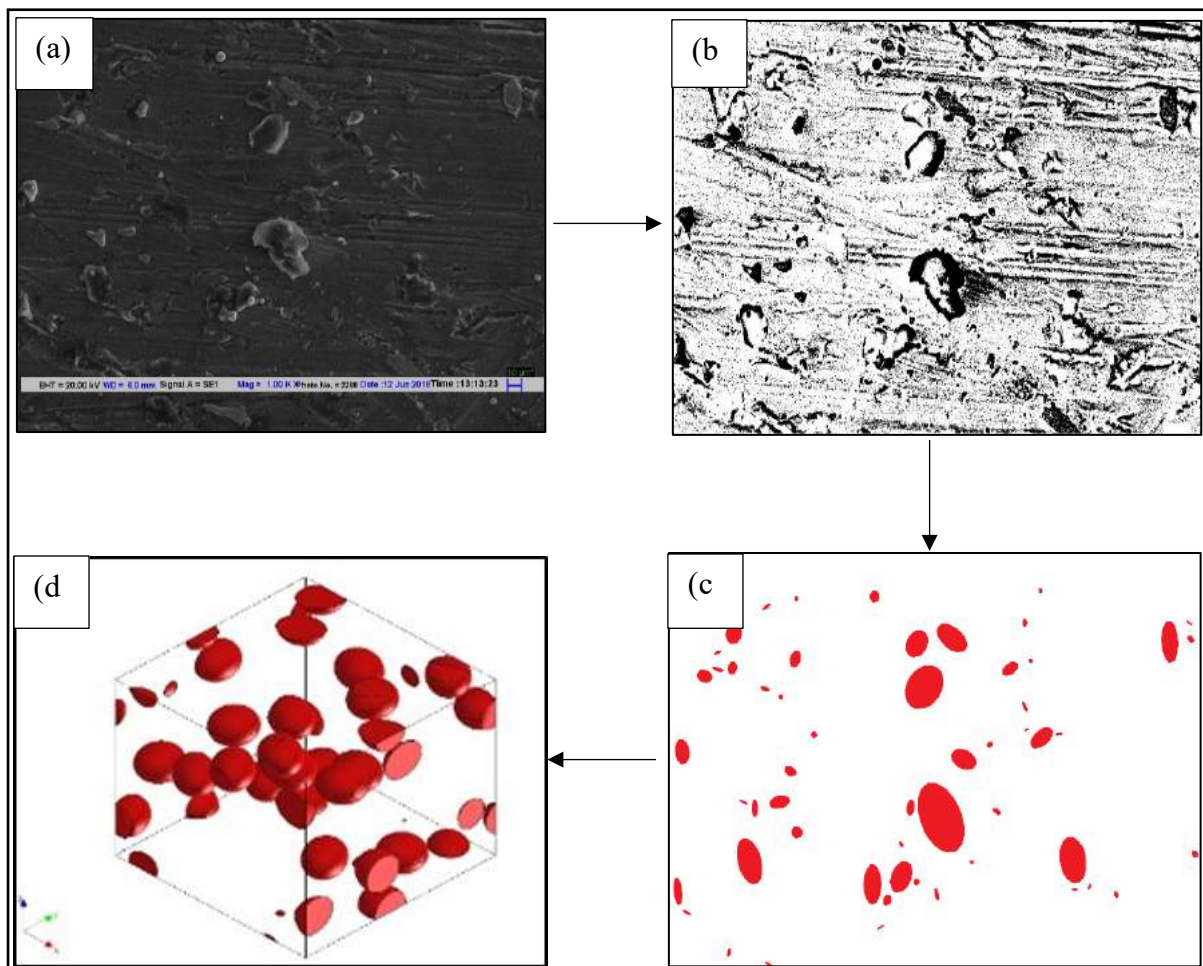


Fig. 5.1: Conversion of an SEM image into an RVE (a) SEM Image of a composite sample (b) Cropped SEM image converted into a binary image (c) Particle analysis of the binary image (d) RVE with mean aspect ratio, size and volume fraction.

avoiding coagulation. This platform has been used for the development of RVEs in many types of researches. RVEs with randomly distributed spherical inclusions, perfectly aligned fibres or random fibre distributions by using a fibre randomization algorithm are generated by using this technique. These RVEs can be exported as standard CAD formats. The effective properties of these RVEs were calculated and have been used for further analysis.

For mean-field homogenization, Mori-Tanaka method has been adopted to determine the effective Young's modulus of the composite material. Therefore, it assumed that the metal matrix composite is comprised of N number of phases. Matrix phase is denoted by subscript m , and there are remaining $N-1$ inclusion phases in the control volume. The volume fractions of the matrix and the i_{th} inclusion are denoted by ϑ_m and ϑ_i . Similarly, stiffnesses of the matrix and the i_{th} inclusion are denoted by K_m and K_i . These stiffness quantities are generally represented as elasticity tensors of fourth-order, which possess specific symmetrical properties. The overall elastic stiffness of the composite is defined in Eq. (5.1).

$$\bar{K}_{av} = \left(\vartheta_m * K_m + \sum_{i=1}^{N-1} \vartheta_i \langle K_i * D_i^{dil} \rangle \right) + \left(\vartheta_m * \mathbf{I} + \sum_{i=1}^{N-1} \vartheta_i \langle D_i^{dil} \rangle \right)^{-1} \quad (5.1)$$

Where \mathbf{I} is the identity tensor and the dilute strain concentration factor D_i^{dil} is generally expressed in Eq. (5.2).

$$D_i^{dil} = [\mathbf{I} + S_i K_m^{-1} (K_i - K_m)]^{-1} \quad (5.2)$$

Here S_i is the Eshelby tensor for the spheroidal inclusion in the infinite matrix

Since the alumina particles are randomly oriented, orientation averaging has to be taken into account. Therefore, the terms in the angle parentheses $\langle \ \rangle$ denote the averaged value of the parameters over all possible orientations. This orientationally averaged tensor is a fourth-order tensor in the 3D space and can be expressed as in Eq. (5.3).

$$\langle T_{klmn} \rangle = \frac{1}{2\pi} \int_0^{2\pi} \int_0^{2\pi} T_{klmn}(\alpha, \beta) \sin\beta \, d\alpha \, d\beta \quad (5.3)$$

where α, β are the generalized angular orientations. For the randomization, the local coordinates should be transformed to the global coordinates. For overall random transformation, the matrix may be expressed as shown in Eq. (5.4).

$$a_{kl} = \begin{bmatrix} \cos \alpha & \cos \beta \sin \alpha & \sin \beta \sin \alpha \\ -\sin \alpha & \cos \beta \cos \alpha & \sin \beta \cos \alpha \\ 0 & -\sin \beta & \cos \beta \end{bmatrix} \quad (5.4)$$

Moreover, the transformation may be written, as shown in Eq. (5.5).

$$T_{klmn}(\alpha, \beta) = a_{ko} a_{lp} a_{mq} a_{nr} T'_{opqr} \quad (5.5)$$

The effective Young's Modulus (E_{efv}) can be now calculated by the general equation (Eq. (5.6)) with shear modulus and bulk modulus.

$$E_{efv} = E_m * \frac{\kappa_{efv} * \mu_{efv} (3\kappa_m + \mu_m)}{3\kappa_{efv} * \kappa_m + \mu_{efv} * \mu_m} \quad (5.6)$$

Effective Shear modulus can be derived using Eq. (5.7).

$$\frac{\kappa_{efv}}{\kappa_m} = \frac{1}{1 + z p} \quad (5.7)$$

Effective Bulk modulus can be derived using Eq. (5.8).

$$\frac{\mu_{efv}}{\mu_m} = \frac{1}{1 + z q} \quad (5.8)$$

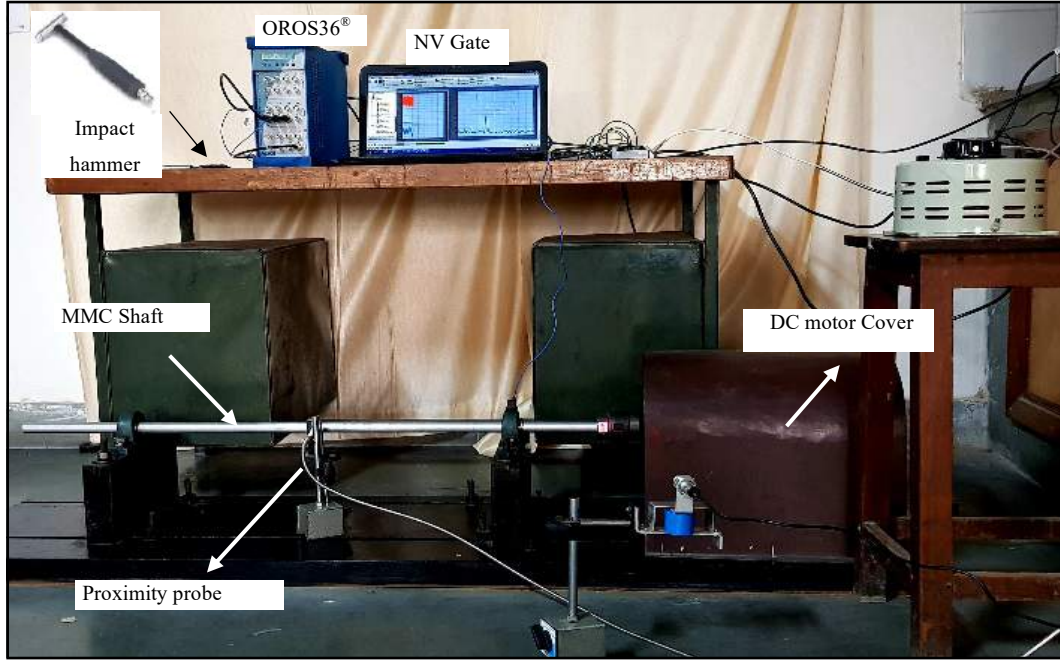


Fig 5.2: Experimental set up for impact hammer

Where E_{efv} is the effective Young's modulus, E_m is Young's modulus of the matrix, κ_{efv} and μ_{efv} are the effective bulk and shear moduli of the composite, z is the volume concentration/fraction, κ_m and μ_m are the bulk and shear modulus of the matrix. Also, p and q are the explicit expressions, and these expressions and details of the expression can be seen for spheroidal inclusions for detailed reference.

Also, effective density can be easily calculated through the rule of the mixture, as shown in Eq. (5.9).

$$\rho_{efv} = \rho_m \vartheta_m + \rho_i \vartheta_i \quad (5.9)$$

Where ρ_{efv} is the effective density, ρ_m and ϑ_m are the density and volume fraction of matrix and ρ_i and ϑ_i are the density and volume fraction of inclusions.

5.1.2 Experimental evaluation of Elastic properties

For the experimental validation of the estimated/predicted properties of the composites, ASTM E1876 impact hammer vibration analysis was employed. The analysis is performed on a

standard experiment setup which conforms the prerequisites for the ASTM E1876 standard, as shown in Fig. 5.2.

The inductive proximity sensor (LJ12A3-4-Z /BY) having a sensitivity of 1000 V/m and a detection range of 4000 μm is used. The test specimens are energized through a force transducer with a plastic tip. Impact Hammer (Model: - PCB-086C03) with sensitivity 2250 $\mu\text{(V)/(N)}$ and range 4440N is used for transient excitation. The response from the transducers is collected and analyzed by using a 32 channel, vibration analyzer OROS36[®]. The channels of these analyzers are handled in real-time: FFT, 1/3rd Octave. The fundamental natural frequencies of the specimen are observed from the peaks of the frequency response function obtained by using NV Gate[®] (version 10.1.1) interface.

The prime objective of the experimentation was to extract the values of natural frequencies for the first two bending (flexural) modes of the shaft. A range of 0-600 Hz was targeted as per the dimensions for experimental analysis to confirm that primarily these modes are excited. For excitation, the plastic tip of suitable hardness was used such that the input spectrum doesn't prominently excite the frequencies beyond the working range. The experimental samples were selected carefully such that the impact force input spectrum excites the required range of frequency at amplitude high enough to avoid noise interceptions. The sampling rate of 2.04 kS/s (kilo samples per second) was chosen, which was much higher than the Nyquist frequency according to the range excited by the input spectrum and the range of observation. This high rate of sampling prevented the problem of leakage and aliasing, and no anti-aliasing filters were required. The motive of the experimentation was also to observe the damping of the material relative to each other. The windowing technique would have altered the peak width and thus, the estimation of damping. Therefore, the time range was taken in

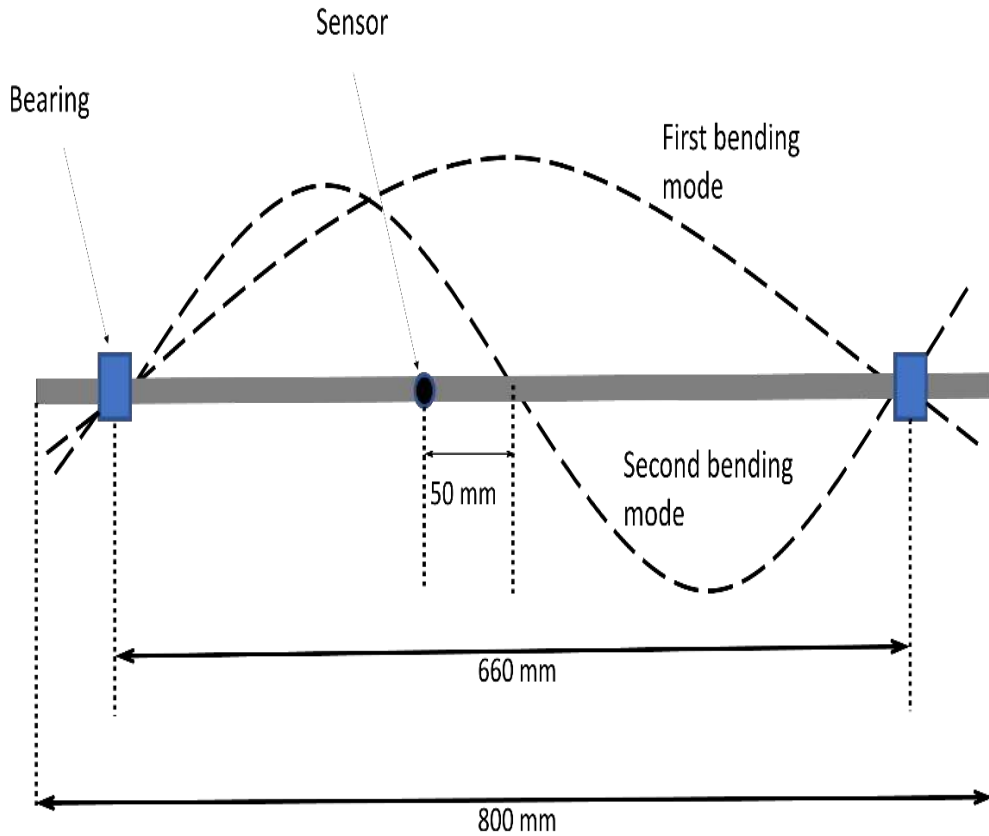


Fig. 5.3: First and second bending mode with sensor positioning.

such a way that windowing was not required for sample selection. The high resolution of the sampling ensured that the natural frequency is confidently determined by Gaussian peak fitting method. The position of the sensor has to be chosen in such a way that it should detect the first and second mode excitation. At the centre of the shaft, the first mode was highly excited, but the second mode was not excited (Since the anti-node of the second mode is at the centre for the simply supported system). Therefore, a non-contact inductive proximity transducer was roved, and a suitable position was chosen where the excitation of first and second peaks was obtained successfully (At a distance of 50 mm from the centre as shown in Fig. 5.3). At this position, the amplitude of first bending natural frequency peak is the highest followed by second bending natural frequency peak.

The Young's modulus expression for the known fundamental flexural natural frequency is shown in Eq. (5.10).

$$E = 1.6067 \left(\frac{l^3}{d^4} \right) (mf_f^2) T_1 \quad (5.10)$$

where E = Young's modulus, l= Length of the specimen, d= diameter of the shaft, m= mass of the shaft, f_f = fundamental flexural frequency of the shaft and T_1 =correction factor for the fundamental flexural mode to account for finite diameter of the rod, and Poisson's ratio.

Since the aspect ratio (l/d) is higher than 20, the simplified form for T_1 can be used as shown in Eq. (5.11).

$$T_1 = \left[1 + 4.939 \left(\frac{d}{l} \right)^2 \right] \quad (5.11)$$

The expression for Dynamic shear modulus for known fundamental torsion resonant frequency of a cylindrical is shown in Eq. (5.12).

$$G = 16mf_t^2 \left(\frac{l}{\pi d^2} \right) \quad (5.12)$$

where G = Dynamic shear modulus, l= Length of the specimen, d= diameter of the shaft, m= mass of the shaft, f_t = fundamental torsional frequency of the shaft.

Correspondingly, Poisson's Ratio can be determined using Eq. (5.13).

$$\mu = \left(\frac{E}{2G} \right) - 1 \quad (5.13)$$

Where μ is the Poisson's ratio

5.2 Results and Discussion

Since there might be inhomogeneous zones within the sample that lead to interference of the results, measures are taken to avoid these uncertainties. Three samples were taken for each material for SEM analysis. The SEM images were randomly taken for different positions within the sample and all six surfaces of the cuboid sample with 1000x magnifications. For each

sample (S1, S2 and S3), maximum, minimum, and mean values of volume fraction, aspect ratio and particle size are taken for various SEM micrographs as shown in Table 5.1.

Table 5.1 Mean volume fraction, aspect ratio and particle size for various SEM images

Shaft Material		Mean volume fraction			Mean aspect ratio			Mean particle size (μm)		
		S1	S2	S3	S1	S2	S3	S1	S2	S3
Al 6061/6 wt.% Al ₂ O ₃	Max	4.0	4.8	4.7	3.1	2.9	3.1	8.7	8.9	8.8
	Min	2.9	3.4	3.1	2.6	2.6	2.7	7.3	7.2	7.1
	Mean	3.4	4.1	3.8	2.9	2.7	3.0	8.0	8.1	8.1
Al 6061/12 wt.% Al ₂ O ₃	Max	8.3	9.4	9.9	3.4	3.2	3.3	8.9	8.8	9.0
	Min	6.9	7.4	7.9	2.8	2.7	2.9	7.3	7.5	7.4
	Mean	7.3	8.1	9.1	3.2	3.0	3.1	8.3	8.2	8.4
Al 6061/18 wt.% Al ₂ O ₃	Max	11.2	10.2	12.1	3.4	3.6	3.5	9.1	8.9	9.0
	Min	8.9	9.4	9.1	2.6	2.7	2.9	7.5	7.1	7.8
	Mean	10.3	10.4	11.3	3.0	3.1	3.2	8.5	8.2	8.5

The aspect ratio and particle size doesn't vary much for different samples and materials. The mean volume fraction increased with the addition of reinforcement from 6 wt. % to 12 wt.% of reinforcement. The variation of the microstructural parameters within the sample were not resulting in interference with the microstructural parameters of different composition. For example, the mean volume fraction ranges from 2.9 to 4.8 for Al 6061/6 wt.% Al₂O₃, 6.9 to 9.9 for Al 6061/12 wt.% Al₂O₃ and 8.9 to 11.2 for Al 6061/18 wt.% Al₂O₃. The data is therefore categorical, and we can classify the results for different composition of materials respectively.

The modulus of elasticity is highest for the largest volume fraction, highest aspect ratio and smallest mean particle size and vice versa. The strengthening is due to the orowan

strengthening effect where the reinforcement hinders the dislocation of the crystalline structure and also because of grain refinement of the microstructure. Therefore, the overall highest Young's modulus can be predicted by taking mean volume fraction as 4.8, aspect ratio as 3.1 and mean particle size as 7.1 μm and vice versa for Al 6061/6 wt.% Al_2O_3 . The overall highest Young's modulus can be predicted by taking mean volume fraction as 9.7, aspect ratio as 3.4 and mean particle size as 9.0 μm and vice versa for Al 6061/12 wt.% Al_2O_3 . The overall highest Young's modulus can be predicted by taking mean volume fraction as 10.66, aspect ratio as 3.1 and mean particle size as 8.3 μm and vice versa for Al 6061/12 wt.% Al_2O_3 . The consolidated results for the estimated microscopic properties through image analysis and mean-field homogenization are shown in Table 5.2.

Table 5.2 Image analysis overall mean results

Material	Mean volume fraction	Mean aspect ratio	Mean particle size (μm)
Al 6061	---	---	---
6 wt. % Al_2O_3/Al 6061	3.8	2.9	8.1
12 wt. % Al_2O_3/Al 6061	8.166	3.1	8.3
18 wt. % Al_2O_3/Al 6061	10.66	3.1	8.3

On the addition of 6 wt.% of alumina, the overall mean volume fraction of 3.8 % is observed by image analysis of SEM images for different samples. The observed volume fraction of alumina in fabricated samples is low as compared to the volume fraction of alumina added during stir casting. The limitation of the stir casting method that all alumina particles are not mixed with the matrix is the reason for this deviation. Although stir casting is flexible enough and large-sized samples used for analysis can be easily manufactured through this method. Similarly, for the addition of 12 wt.% of alumina particles and 18 wt.% of alumina, the mean volume fraction of 8.166 % and 11.66 % is observed. The mean aspect ratio and the average

particle size are also in the conformance with the alumina particles manufacturer specification. The standard value of Young's Modulus, Poisson's ratio and the shear modulus of in-plane and transverse plane for a particular Al6061 aluminium alloy is shown in Table 5.3. The Mean-

Table 5.3 Initial set of standard values for Al 6061

Engineering constants	Initial value
In-Plane Young's modulus (GPa)	70
Out -Plane Young's modulus (GPa)	70
In-Plane Poisson's ratio	0.328
Transverse Poisson's ratio	0.328
In-Plane shear modulus (GPa)	26.35
Transverse shear modulus (GPa)	26.35
Global Density (Kg/m ³)	2710

Table 5.4 Mean-field homogenization results for 6 wt. % Al₂O₃/Al 6061

Engineering constants	Computed Estimation		
	Mean	Max	Min
In-Plane Young's modulus (GPa)	73.73	74.84	72.9
Out -Plane Young's modulus (GPa)	73.61	74.71	72.78
In-Plane Poisson's ratio	0.326	0.325	0.326
Transverse Poisson's ratio	0.326	0.325	0.326
In-Plane shear modulus (GPa)	27.8	28.21	27.48
Transverse shear modulus (GPa)	27.76	28.17	27.44
Global Density (Kg/m ³)	2748	2772	2723

field homogenization results for 6 wt. % Al₂O₃/Al 6061 is shown in Table 5.4. The mean value of In-Plane Young's modulus is 73.73 GPa, Out-Plane Young's modulus is 73.61 GPa.

Table 5.5 Mean-field homogenization results for 12 wt. % Al₂O₃/Al 6061

Engineering constants	Computed Estimation		
	Mean	Max	Min
In-Plane Young's modulus (GPa)	78.66	80.1	77.4
Out -Plane Young's modulus (GPa)	78.32	79.75	77.06
In-Plane Poisson's ratio	0.322	0.321	0.323
Transverse Poisson's ratio	0.322	0.321	0.323
In-Plane shear modulus (GPa)	29.75	30.29	29.27
Transverse shear modulus (GPa)	29.2	29.73	28.73
Global Density (Kg/m ³)	2798	2838	2753

Table 5.6 Mean-field homogenization results for 18 wt. % Al₂O₃/Al 6061

Engineering constants	Computed Estimation		
	Mean	Max	Min
In-Plane Young's modulus (GPa)	82.15	83.7	80.9
Out -Plane Young's modulus (GPa)	82.32	83.63	80.71
In-Plane Poisson's ratio	0.33	0.31	0.313
Transverse Poisson's ratio	0.33	0.31	0.313
In-Plane shear modulus (GPa)	30.883	31.94	30.76
Transverse shear modulus (GPa)	30.94	31.91	30.81
Global Density (Kg/m ³)	2832	2902	2799

The Mean-field homogenization results for 12 wt. % $\text{Al}_2\text{O}_3/\text{Al}$ 6061 is shown in Table 5.5. The mean value of In-Plane Young's modulus is 78.66 GPa, Out-Plane Young's modulus is 78.32 GPa. The Mean-field homogenization results for 18 wt. % $\text{Al}_2\text{O}_3/\text{Al}$ 6061 is shown in Table 5.6. The mean value of In-Plane Young's modulus is 82.715 GPa, Out-Plane Young's modulus is 82.32 GPa.

The estimated mean In-plane Young's modulus is increased by 5.32%, on the addition of 6 wt.% of alumina due to enhanced dislocation density and precipitation hardening. Since the orientation of the particles is randomized, the value of out of plane Young's modulus is approximately the same as values of In-plane Young's modulus. The global density of the composite is also estimated to be increased by the addition of the particles since the density of the alumina particles is more than the aluminium matrix. The mean In-Plane shear modulus is also increased by 5.5% with transverse shear modulus value approximately similar to the In-plane shear modulus. Moreover, the effective In-plane Young's Modulus is estimated to be increased by 12.37% on addition of 12 wt.% of alumina. The highest value of density and shear modulus is observed for the composite with 18 wt. % of alumina reinforcements.

As shown in Table 5.3, 5.4, 5.5 and 5.6, there is no interference in respective values of Young's modulus, Poisson's ratio and shear modulus for different materials. For example, the minimum value of In-plane Young's modulus of 12 wt. % $\text{Al}_2\text{O}_3/\text{Al}$ 6061 is 77.4 GPa, whereas the maximum value of In-plane Young's modulus of 6 wt. % $\text{Al}_2\text{O}_3/\text{Al}$ 6061 is 74.84 GPa. Similarly, the minimum value of In-plane Young's modulus of 18 wt. % $\text{Al}_2\text{O}_3/\text{Al}$ 6061 is 80.9 GPa, whereas the maximum value of In-plane Young's modulus of 12 wt. % $\text{Al}_2\text{O}_3/\text{Al}$ 6061 is 80.1 GPa. So, this data can be classified by the composition of the material.

The strengthening effect of reinforcement is not directionally dependent as in the case of fibre reinforced composites due to the random orientation of particles. By adding 12 wt. % of alumina, In-Plane Young's modulus is increased by 12.37 %, but the global density is increased by 3.2%. It implies that the addition of reinforcement improves the specific modulus

of the material and therefore improves the modal response of the material. Therefore, impact

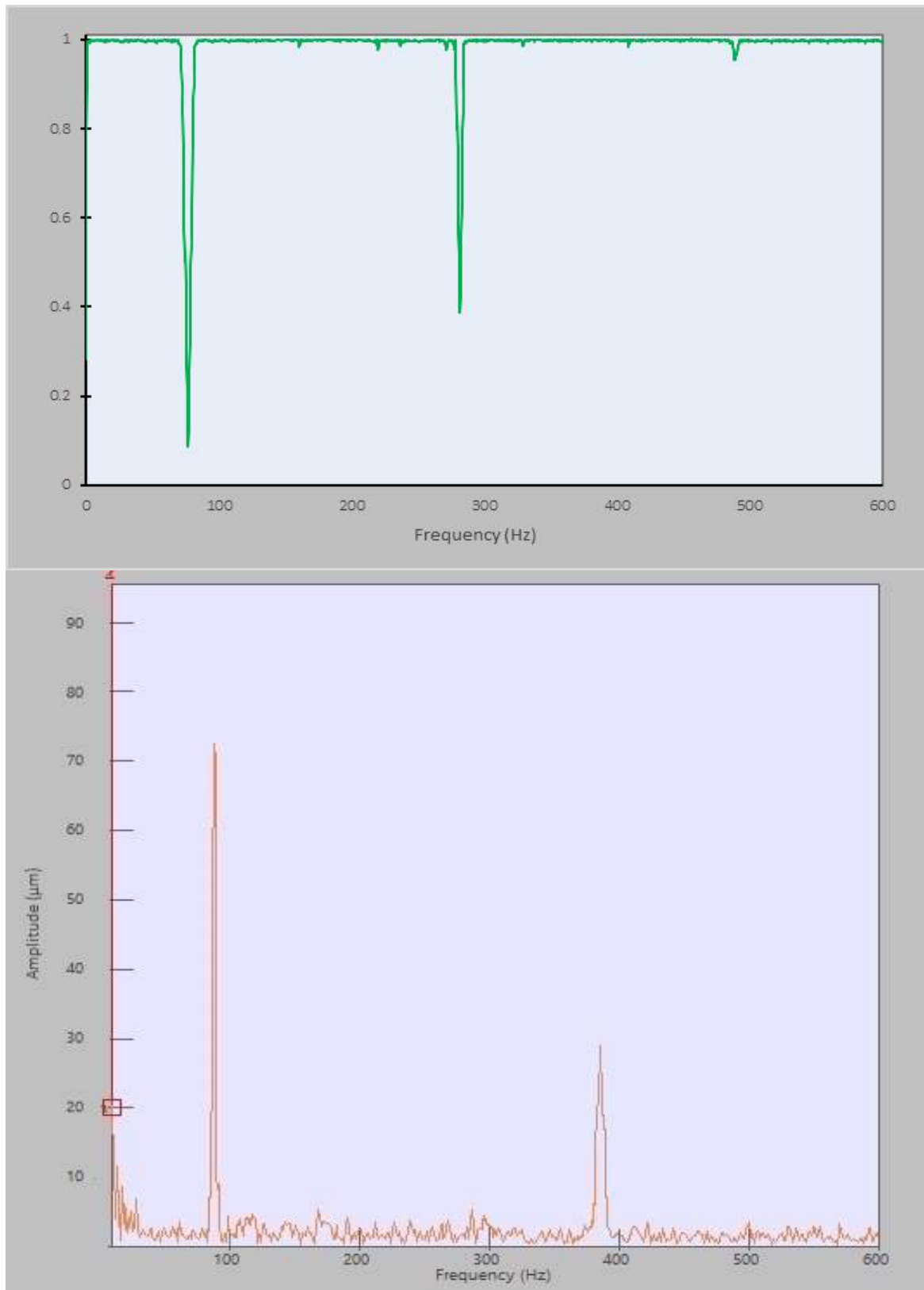


Fig. 5.4: FRF and coherence for Al6061

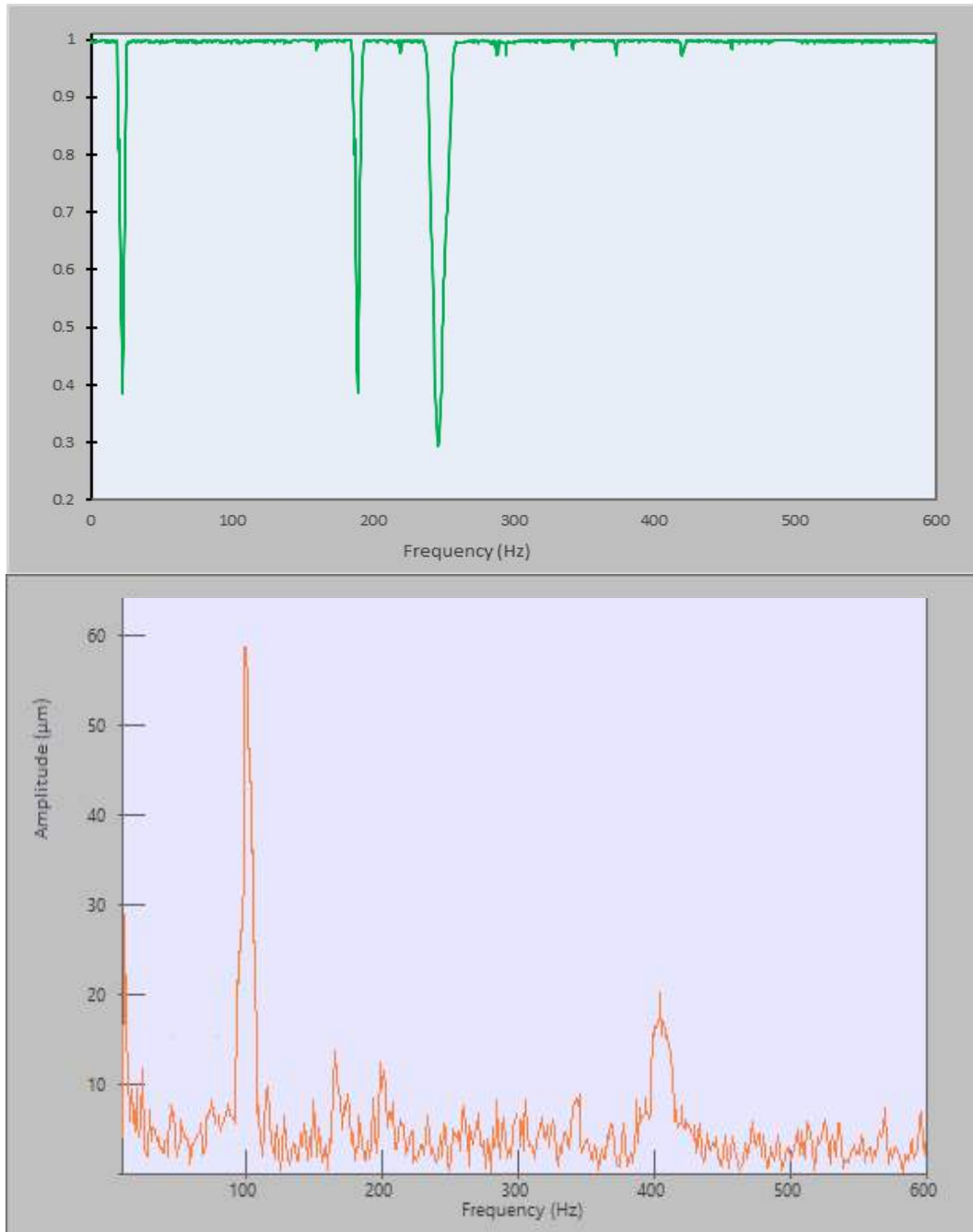


Fig. 5.5: FRF and coherence for Al6061/ 6 wt. % Al₂O₃

hammer test is performed to obtain the properties of composites through modal response.

The frequency response function and the coherence for Al6061, Al6061/6 wt. % Al₂O₃, Al6061/ 12 wt. % and Al₂O₃ Al6061/ 18 wt. % Al₂O₃ composite in the impact hammer test is shown in Fig. 5.4, Fig. 5.5, Fig. 5.6 and Fig. 5.7. The input and output spectrums were coherent for all shafts, with the resonance value dropped at anti-nodes. The high coherence between the

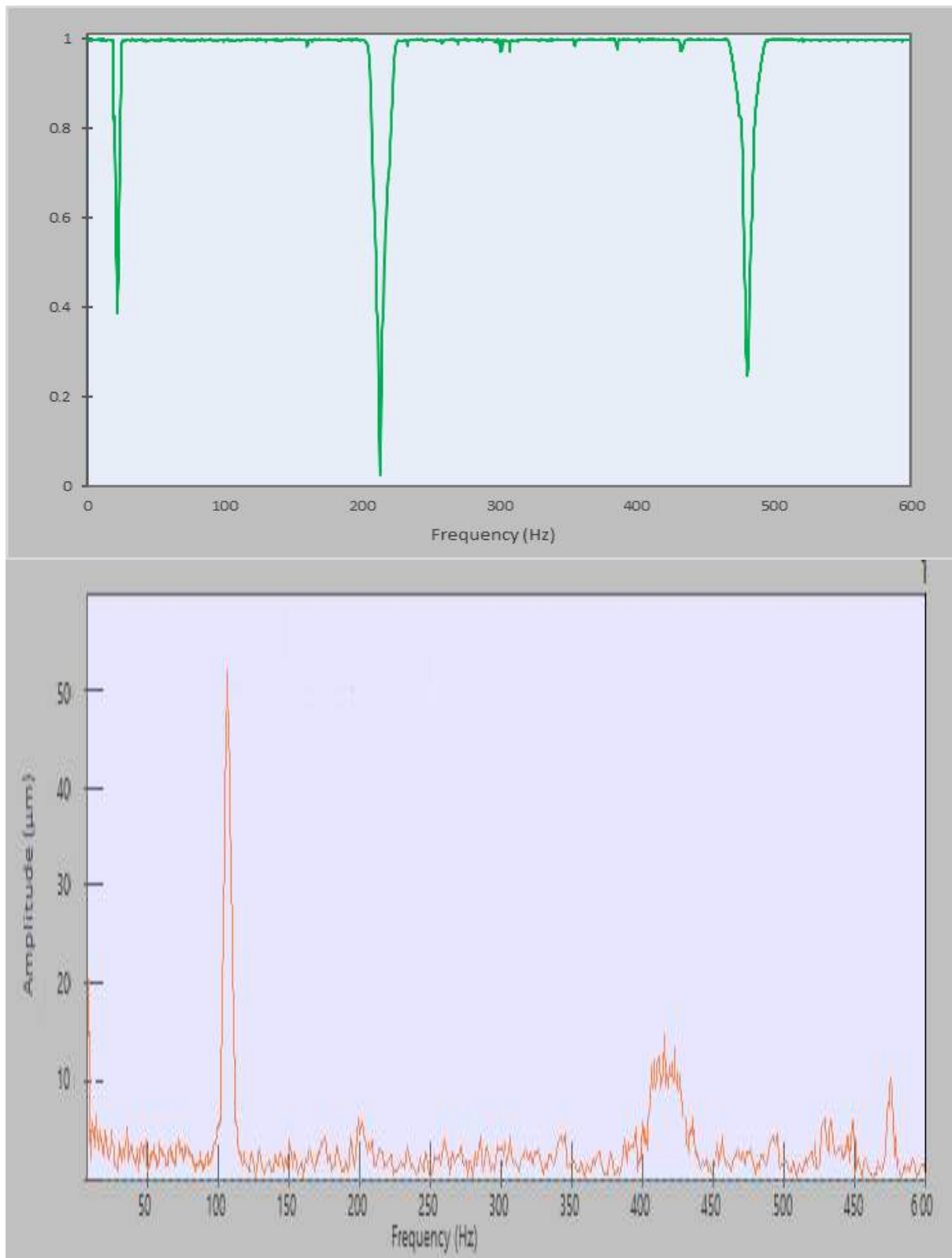


Fig. 5.6: FRF and coherence for Al6061/ 12 wt. % Al_2O_3

input and output spectrum, except at the anti-nodes confirms the replicability of the experiments. The high resolution of the frequency spectrum was obtained because of the high

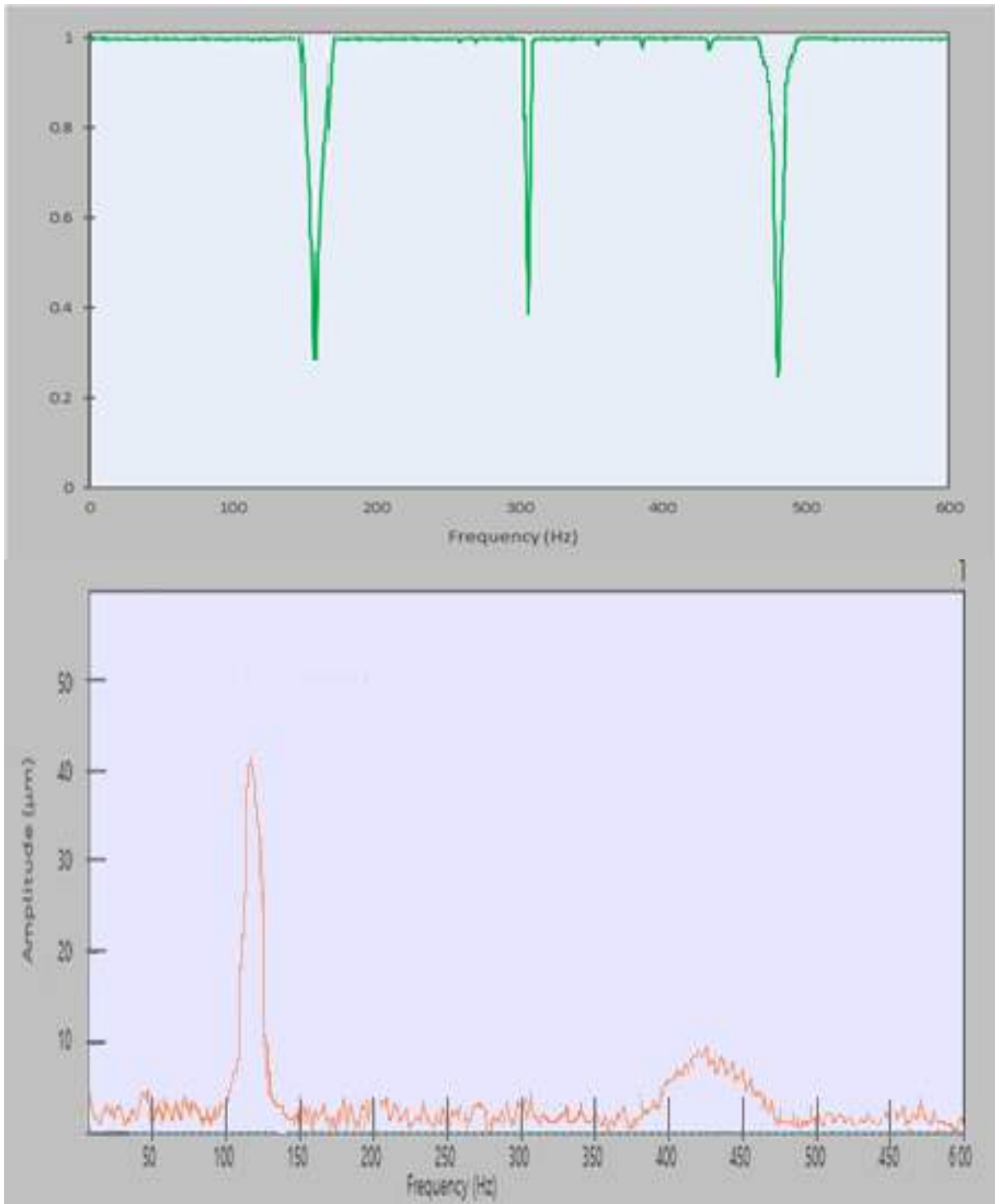


Fig. 5.7: FRF and coherence for Al6061/ 18 wt. % Al_2O_3

sampling rate. The amplitude and the natural frequency were calculated by determining the peak using the Gaussian peak fitting method, and the damping ratio is obtained by the half-power bandwidth method.

Table 5.7 Experimental natural frequency mean, standard deviation and range

Shaft Material	Natural frequency (1 st mode)			Natural frequency (2 nd)		
	Mean	σ	Range	Mean	σ	Range
Al6061	98.62	0.65	97.6- 99.1	388.9	1.92	386.1-391.6
Al 6061/6 wt.% Al₂O₃	101.6	0.72	100.1- 102.8	408.4	2.42	406.3-411.7
Al 6061/12 wt.% Al₂O₃	108.9	1.01	107.1-110.7	420.2	3.02	416.2- 425.1
Al 6061/18 wt.% Al₂O₃	112.9	0.91	110.1-114.7	431.5	2.92	427.5- 432.1

For each shaft with different composition, thirty experiments were taken for the determination of natural frequencies, damping ratio and amplitudes. The mean, standard deviation and range of the natural frequencies for different sets of experimentations are shown in Table 5.7.

The low standard deviation was obtained for the values of natural frequencies for both first and second mode. Also, the range of natural frequency values for different composition

Table 5.8 Experimental damping mean, standard deviation and range

Shaft Material	Damping (first mode)			Damping (second mode)		
	Mean	σ	Range	Mean	σ	Range
Al6061	0.0097	0.0001	0.0095-0.0099	0.021	0.0003	0.0207- 0.026
Al 6061/ 6 wt.% Al₂O₃	0.0123	0.0004	0.0119-0.0129	0.0233	0.0005	0.0225- 0.0242
Al 6061/ 12 wt.% Al₂O₃	0.0146	0.0006	0.0137-0.155	0.026	0.0008	0.0252-0.0262
Al 6061/ 18 wt.% Al₂O₃	0.0172	0.0004	0.0169-0.185	0.030	0.0008	0.0282-0.0322

doesn't interfere with each other. The natural frequency increases significantly with the increase of reinforcement particles in the shafts. This is due to the reason that the addition of alumina particles in the Al6061 matrix leads to a substantial improvement in the bending stiffness as compared to the material density. The natural frequency is proportional to the specific modulus of the material which is the ratio of the Young's modulus (bending stiffness) and density. The mean, standard deviation and range of the damping for different sets of experimentations are shown in Table 5.8.

The higher value of damping was observed for the specimen with higher wt.% of alumina particles in the aluminium matrix. The damping was significantly increased for the second mode of vibration.

It suggests that the damping increases with the increase of alumina particles in the aluminium matrix. This is due to the grain refinement and formation of secondary phases which increases elastic strain energy dissipation in the materials.

Table 5.9 Experimental amplitude mean, standard deviation and range

Shaft Material	Amplitude (first mode) (μm)			Amplitude (second mode) (μm)		
	Mean	σ	Range	Mean	σ	Range
Al6061	69.1	2.11	67.1- 70.9	30.21	2.01	31.2-27.1
Al 6061/6	62.7	2.03	60.7- 64.2	21.62	2.42	22.5-19.1
wt.% Al₂O₃						
Al 6061/12	52.1	2.81	50.2- 54.8	14.29	2.65	12.31-17.01
wt.% Al₂O₃						
Al 6061/18	43.5	2.36	41.2- 49.1	9.11	2.47	8.22-11.01
wt.% Al₂O₃						

The mean, standard deviation and range of the amplitude of vibrations for different sets of experimentations are shown in Table 5.9.

The amplitude reduced significantly with the increase in alumina particles for both the modes. The range and the standard deviation are well within the limit that is required for the data to be categorical about the composition of the material. This is due to the increase in bending stiffness of the shafts because of the reinforcing effect of the alumina particles in the matrix.

These values are utilized to obtain the value of In-plane Young's modulus, shear modulus and Poisson's ratio experimentally, as per ASTM E1876 standard. The comparison of predicted values obtained through mean-field homogenization and the experimental values obtained is shown in Table 5.10.

Table 5.10 Comparison of Predicted and experimental value

Shaft Material		Young's modulus		Shear modulus		IP Poisson's rat.	
		Value	% err.	Value	% err.	Value	% err.
Al 6061	Pred.	70 GPa		26.35 GPa		0.328	
	Exp.	67.98 GPa	-2.88%	25.55 GPa	-2.2%	0.327	-0.3%
6 wt. % Al ₂ O ₃ /Al 6061	Pred.	73.73 GPa		27.82 GPa		0.326	
	Exp.	74.61 GPa	1.19%	29.01 GPa	4.2%	0.323	0.4%
12 wt. % Al ₂ O ₃ /Al 6061	Pred.	78.66 GPa		29.75 GPa		0.322	
	Exp.	81.61 GPa	3.75%	31.21 GPa	4.9%	0.320	0.6%
18 wt. % Al ₂ O ₃ /Al 6061	Pred.	82.15 GPa		30.88 GPa		0.322	
	Exp.	85.76 GPa	4.39%	32.49 GPa	5.3%	0.324	0.61%

The experimental value of In-plane Young's modulus of Al 6061 is observed to be 2.88 % lower than that of initial prediction. This lower value can be attributed to the defects induced

during the casting process of aluminium alloy. However, these defects might have prevailed for the case of 6 wt. % $\text{Al}_2\text{O}_3/\text{Al}$ 6061 also, but the experimental In-plane Young's modulus has increased by 1.19 % as compared to the predicted value. Similarly, experimental In-plane Young's modulus has increased by 3.75 % as compared to the predicted value for the case of 12 wt. % $\text{Al}_2\text{O}_3/\text{Al}$ 6061.

From literature, it is observed that the addition of 6 wt. % micro-sized kaolinite particle in epoxy polymer matrix composite increased the effective elastic modulus from 3100 MPa to 3107.5 MPa. The mean-field homogenization method predicted the value 4.2% higher than the experimental value. Whereas in the present study, the mean-field homogenization predicted the value 1.19% lower than the experimental values. The reason for predicting a lower value by the homogenization process may be that the actual alumina particle volume fraction is higher than the volume fraction estimated by image analysis.

The range of the experimental and the predicted values for the In-plane Young's modulus is shown in Fig. 5.8. For Al 6061, the predicted value is the standard value for Young's modulus, and the experiment values are of the cast material. Therefore, the values are lower due to the introduction of some porosity. For, Al 6061/ 6wt. % Al_2O_3 the experimental range intersects with the predicted value range. For, Al 6061/ 12 wt. % Al_2O_3 and Al 6061/ 18 wt. % Al_2O_3 the experimental range exceeds the predicted value range at a few points. Therefore, it can be concluded that the upper bounds of mean-field solutions should be used for the higher reinforcement compositions. The similar kind of trend is observed for In-plane shear modulus, and the mean-field homogenization analysis does not deviate significantly from the experimental results.

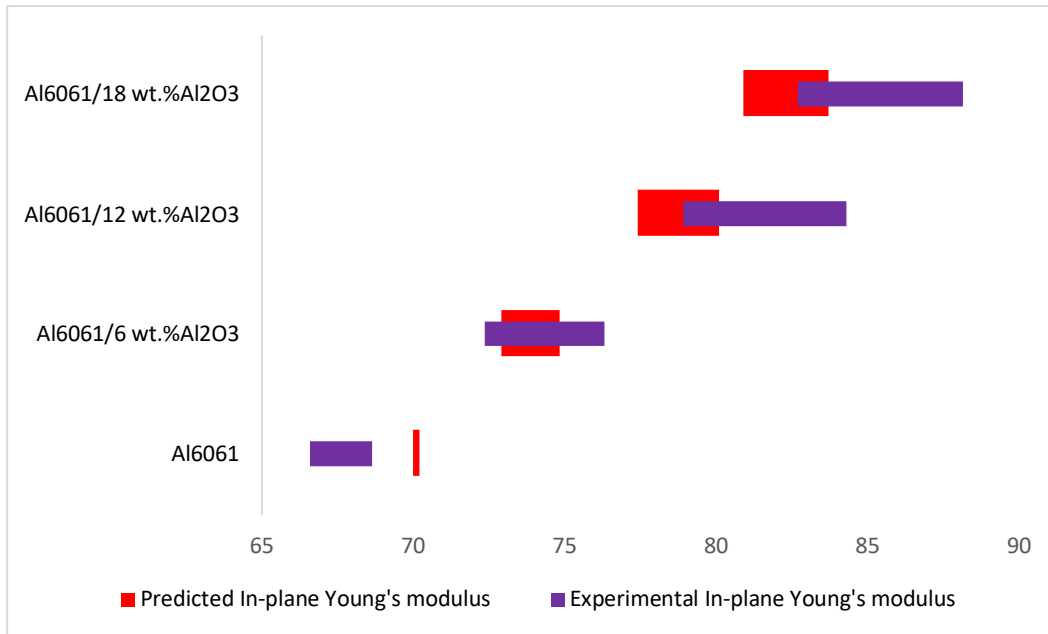


Fig. 5.8: Comparison of range of predicted and experimental value of In-plane

5.3 Summary

The composite specimens have been successfully fabricated by stir casting method as per ASTM E1876 standards. The microstructure of the composites was taken through SEM and particles average size; aspect ratio and fraction were obtained through image analysis method. The effective properties were then evaluated by mean-field homogenization method by using these parameters. These properties were then evaluated experimentally as per ASTM E1876 standards. Following conclusions can be driven from the analysis in this paper:

- The volume fraction of the alumina particles observed by the image analysis method was significantly less as compared to the added volume fraction during fabrication. It suggests that the volume fraction added initially during fabrication should not be used directly for predicting the effective properties.
- The addition of alumina particles results in the strengthening of composite specimens due to enhanced dislocation density and precipitation hardening.

- The difference between the In-Plane and transverse effective properties is negligible since the strengthening effect of reinforcement is not directionally dependent due to the random orientation of particles.
- The addition of alumina particles in the Al6061 matrix leads to a substantial improvement in the bending stiffness as compared to the material density. Due to this reason, the natural frequency for various modes of vibration increased on the addition of particles.
- Damping ratio also increased on the addition of alumina particles due to the grain refinement and formation of secondary phases.
- The estimated error for the case of 6 wt. % $\text{Al}_2\text{O}_3/\text{Al 6061}$ is 1.19%, whereas the estimated error for the case of 12 wt. % $\text{Al}_2\text{O}_3/\text{Al6061}$ is 3.75% for the mean values.
- The range of mean-field values lags behind the experimental values as the material of high reinforcement composition is used. It can be concluded that the upper bound of mean-field homogenization can be used for the material of high reinforcement composition and can be the future scope of work. However, mean-field homogenization predicts a low higher than experimental value while assuming that all alumina particles added for process are mixed into the matrix.
- Also, samples were taken from the end of the shaft for SEM analysis; this might be the low/high composition area of the shaft during casting. This variation can be addressed in future work.
- The variation of the experimental and the predicted values was such that categorization of the values was possible in reference to the composition of the shaft.

The next chapter describes the dynamic analysis of the metal matrix composite rotor through bond graph modelling.

Dynamic Analysis of MMC Rotor

6.1 Bond Graph Modelling

The physical system of a simply supported MMC shaft coupled to a DC motor with a dissipative coupling is shown in Fig. 4. The shaft's material is assumed to be homogeneous and continuous throughout the length. The beam is assumed to be simply supported at the ends.

The effect of torsional vibrations on the shaft response is neglected in this modelling. The shaft of the composite is assumed to be a Rayleigh beam model where beam's rotary inertia is considered in the analysis. As shown in Fig. 6.2. The generalized Newtonian forces are related to the generalized displacements at the ends of the element as:

$$\begin{bmatrix} F_{xl} \\ M_{xl} \\ F_{xr} \\ M_{xr} \end{bmatrix} = [K] \begin{bmatrix} x_l \\ \varphi_l \\ x_r \\ \varphi_r \end{bmatrix} \quad (6.1)$$

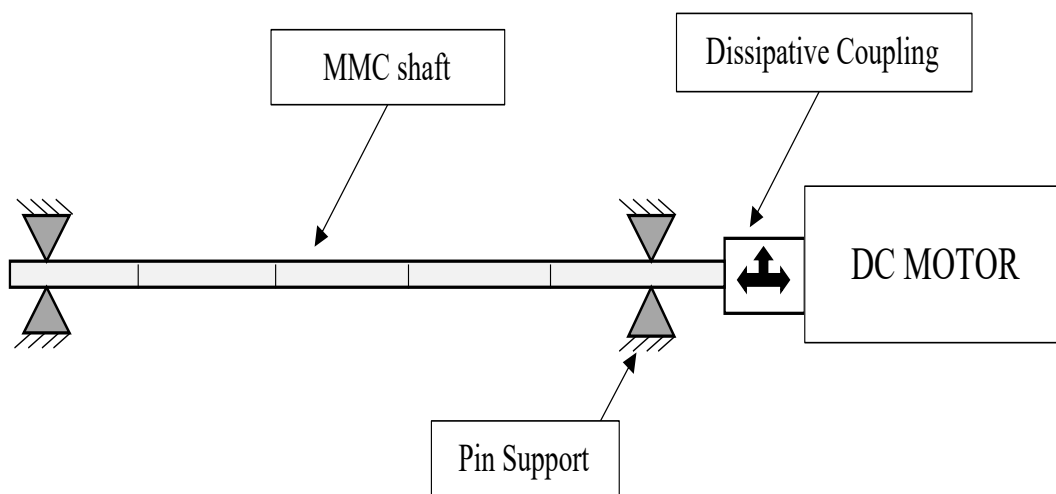


Fig. 6.1: Rotor system with DC motor drive and pin-pin end condition.

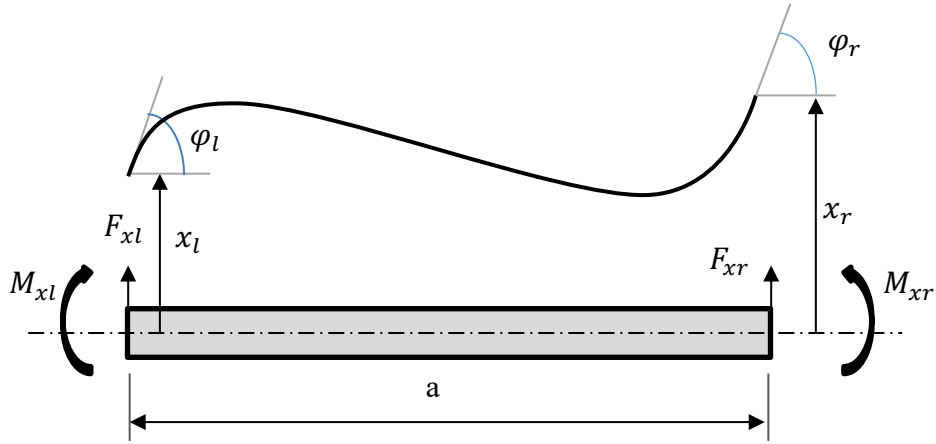


Fig. 6.2: Force and Moment on a Rayleigh beam.

The stiffness matrix may be expressed as:-

$$[K] = \frac{EI}{a^3} \begin{bmatrix} 12 & 6a & -12 & 6a \\ 6a & 4a^2 & -6a & 2a^2 \\ -12 & -6a & 12 & -6a \\ 6a & 2a^2 & -6a & 4a^2 \end{bmatrix} \quad (6.2)$$

Similarly, the relations can be derived for XZ and YZ direction as:

$$\begin{bmatrix} F_{xl} \\ M_{xl} \\ F_{xr} \\ M_{xr} \end{bmatrix} = \frac{EI}{a^3} \begin{bmatrix} 12 & 6a & -12 & 6a \\ 6a & 4a^2 & -6a & 2a^2 \\ -12 & -6a & 12 & -6a \\ 6a & 2a^2 & -6a & 4a^2 \end{bmatrix} \begin{bmatrix} x_l \\ \phi_l \\ x_r \\ \phi_r \end{bmatrix} \quad (6.3)$$

$$\begin{bmatrix} F_{yl} \\ -M_{yl} \\ F_{yr} \\ -M_{yr} \end{bmatrix} = \frac{EI}{a^3} \begin{bmatrix} 12 & 6a & -12 & 6a \\ 6a & 4a^2 & -6a & 2a^2 \\ -12 & -6a & 12 & -6a \\ 6a & 2a^2 & -6a & 4a^2 \end{bmatrix} \begin{bmatrix} y_l \\ -\theta_l \\ y_r \\ -\theta_r \end{bmatrix} \quad (6.4)$$

For bond graph modelling the shaft is reticulated in ten equal parts and the element inertias are lumped at the left and right of each reticulated part. For modelling the stiffness matrix, a four-port compliance fields (C fields) has been denoted as an energy storing element for the different generalized displacements. Since the internal damping force is related to the inertial velocity of the mass center by observing in the rotary frame, the rotary generalized displacements should

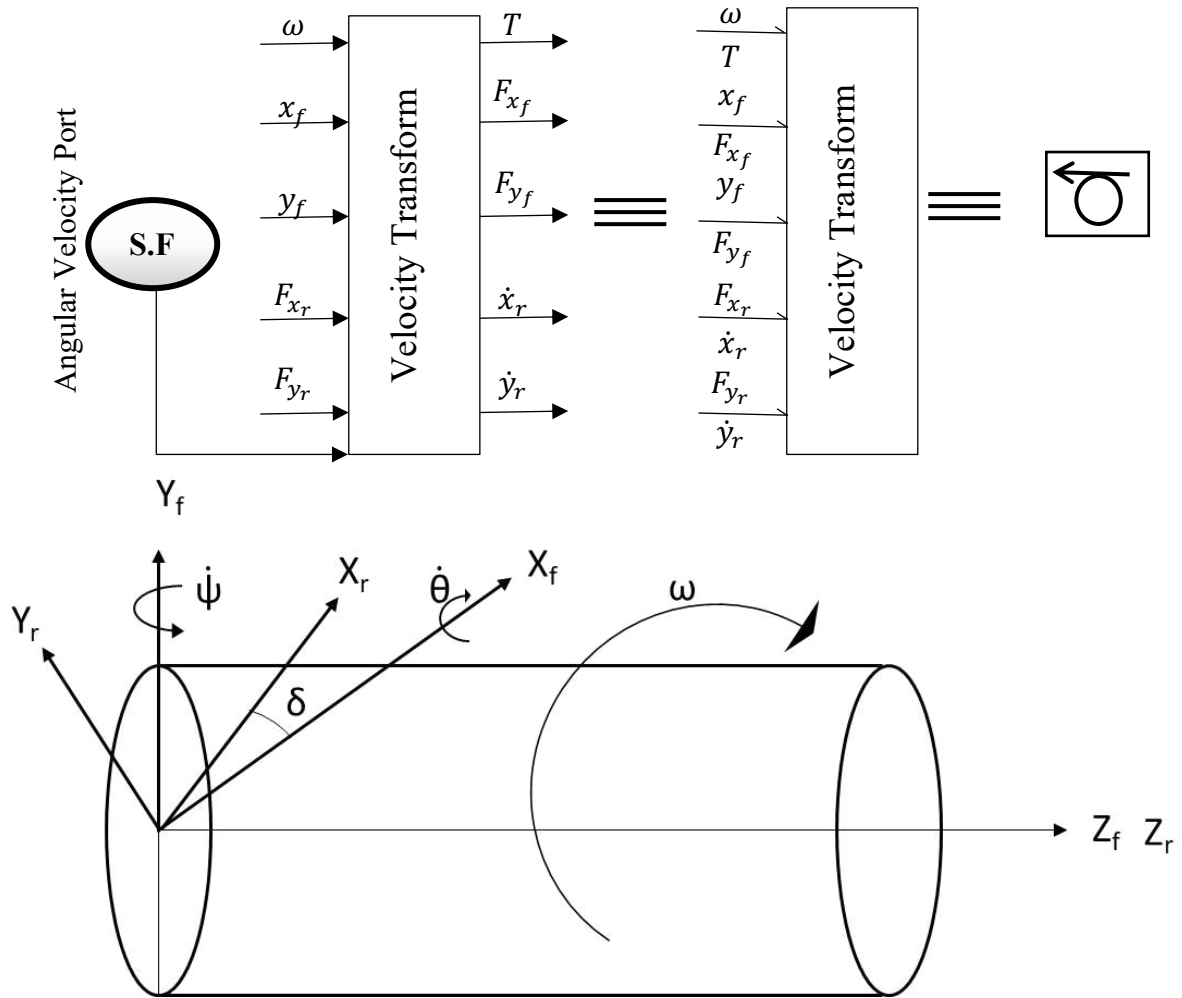


Fig. 6.3: (a) Velocity Transformation capsule (b) Coordinate system diagram

be linked to the internal damping resistance fields (R fields). For that, a transformation sub model has been generated to transform the generalized displacements from fixed to rotary frame velocity in a form of capsule. The capsule has been generated by taking following relation into consideration as shown in Fig. 6.3 (a)

$$\begin{bmatrix} \dot{X}_r \\ \dot{Y}_r \end{bmatrix} = \begin{bmatrix} \cos \partial & \sin \partial \\ -\sin \partial & \cos \partial \end{bmatrix} \begin{bmatrix} \dot{X}_f \\ \dot{Y}_f \end{bmatrix} - \omega \begin{bmatrix} \sin \partial & -\cos \partial \\ \cos \partial & \sin \partial \end{bmatrix} \begin{Bmatrix} X_f \\ Y_f \end{Bmatrix} \quad (6.5)$$

and $\dot{\partial} = \omega$

The Velocity transformation capsule is represented in Fig. 6.3(b).

The spinning shaft capsule for a reticule has been generated as shown in Fig. 6.4. The external damping (R_{ex}) is associated with the fixed X and Y frame. Common flow junctions (1 junctions)

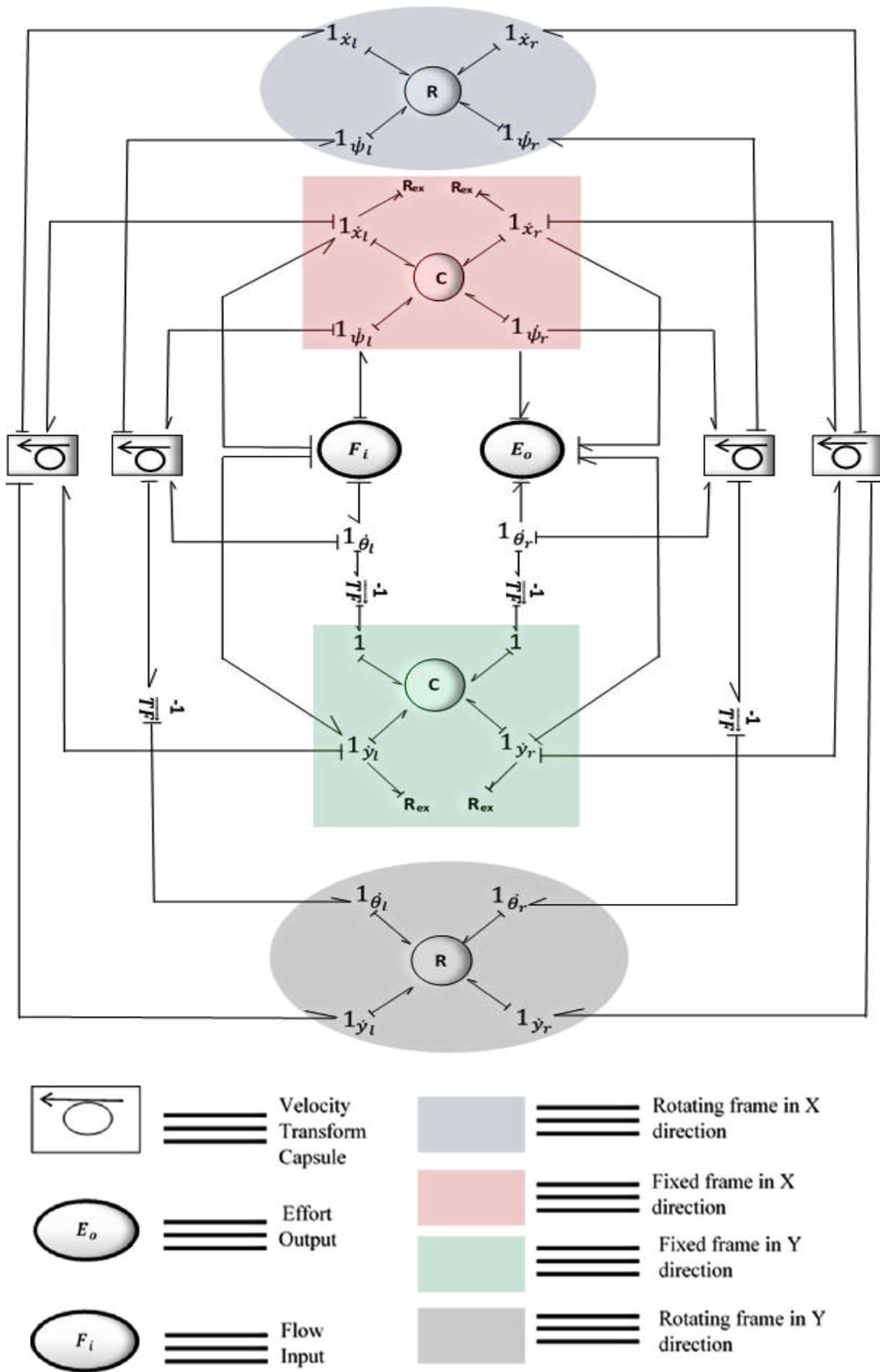


Fig. 6.4: Insight of the spinning shaft mechanism

for generalized displacements in fixed and rotary frames are linked to the corresponding R

fields and C fields. Angular velocity port is introduced in the velocity transform capsule for importing the angular speed into the model. Flow input interface (F_i) is connected to the left side of the fixed generalized velocity junctions ($\dot{x}_l, \dot{y}_l, \dot{\theta}_l, \dot{\phi}_l$). Similarly, effort output interface (E_o) is connected to the right side of the fixed generalized velocity junctions ($\dot{x}_r, \dot{y}_r, \dot{\theta}_r, \dot{\phi}_r$). These interfaces are also connected to the corresponding velocity transform where the fixed generalized velocities are converted to rotary frame velocities and incorporated in the R fields. The coordinates of the mass center of the considered segment of the shaft (x_m, y_m) can be obtained from the coordinates of the geometric center of that segment (x, y) as follows:

$$y_m = y + \cos(\theta + \psi) \quad (6.6)$$

$$\dot{y}_m = \dot{y} - \dot{\psi} \sin(\theta + \psi) = \dot{y} + (-1)k \quad (6.7)$$

where $k = \dot{\psi} \sin(\theta + \psi)$, which is converted by velocity transformation capsule

As there is no proportionality between the rotations between angle of rotation about X-axis and the ends of the shaft due to bending in YZ-planes as used in deriving C-field matrix

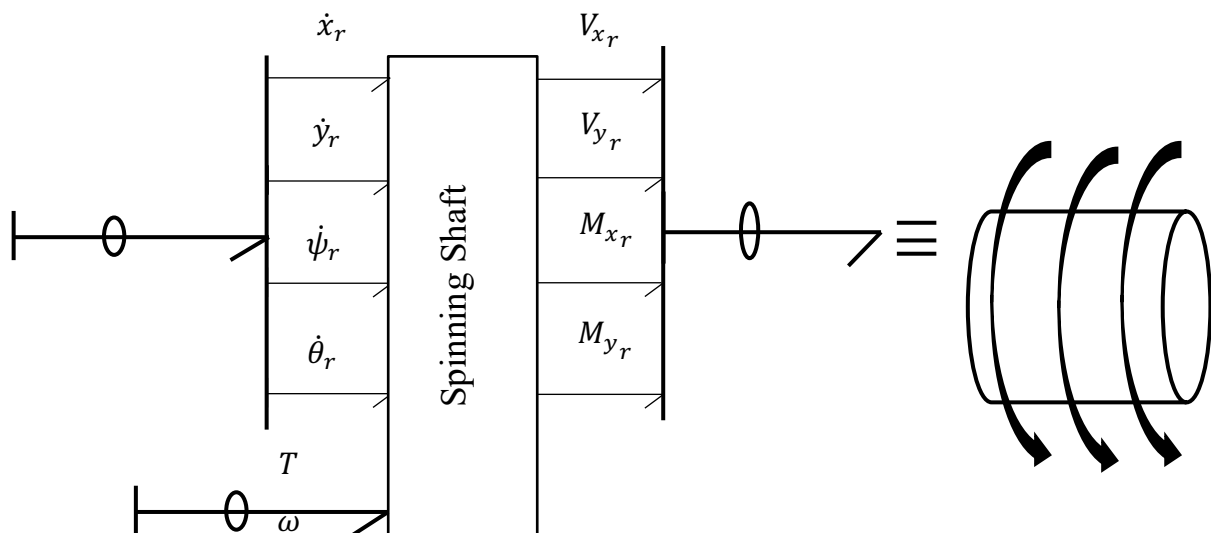


Fig. 6.5: Capsule of the spinning shaft

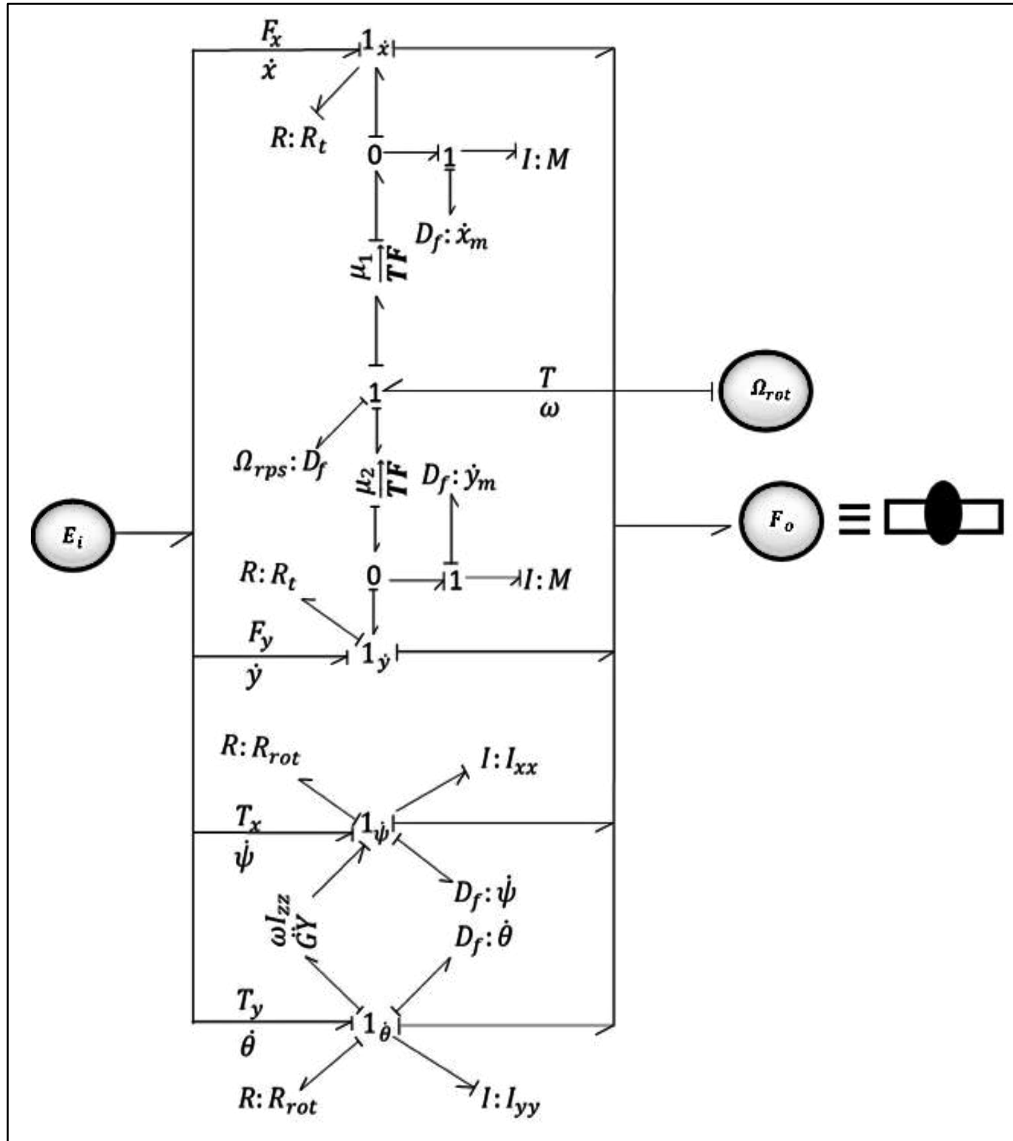


Fig. 6.6: Spinning hub capsule.

,therefore, two-transformer elements (TF) with negative unitary modulus are introduced in the model as shown in Fig. 6.4. This spinning shaft model is cased into a capsule so that it can be used for multiple port analysis as shown in Fig. 6.5.

The lumped masses and rotary inertias at the ends of the reticulated shafts have to be connected by a spinning hub for connection of flow input port to the effort output port of the element. The spinning hub models the inertia of the shaft element. If required, it may also incorporate eccentricity and the angular orientation of hub center of mass. The angular speed

of the spinning hub is also induced separately in the model and the spinning hub model is converted to a capsule as shown in Fig. 6.6. The D_f elements in the model are flow detectors which provide the output variables for plotting whirl orbits, whirl amplitudes, modes shapes etc.

The nodal mass at any intermediate node for a model with n elements is $M = \frac{\pi R^2 a}{n} * \rho$, diametric moment of inertia $I_{xx}, I_{yy} = \frac{\pi R^4 l}{4} * \rho$. The translational damping (R_t) indicates the resistive elements in fixed X- and Y -frames, whereas rotational damping (R_{rot}) represents about the diametrical axis resistive elements in rotating X- and Y -frames. The modulus of the gyration element in the hub model may be expressed as:-

$$\omega_{zz} = \left\{ \frac{\rho \pi}{2} R^4 + I_{phub} \right\} \Omega \quad (6.8)$$

where I_{phub} is the polar moment of inertia of the hub and Ω is excitation frequency of the shaft. The transformer function elements have their moduli as shown in Fig. 6.8 and their values are:

$$\mu_1 = -\varepsilon \sin (\Omega t + \phi) \quad (6.9)$$

$$\mu_2 = \varepsilon \cos (\Omega t + \phi) \quad (6.10)$$

where ε is the eccentricity of the hub and ϕ is the angle of equivalent single unbalanced mass measured from the vertical axis.

To integrate and interface the different sub models of the various parts of the rotor systems, vectorized bond graph has been employed as shown in Fig. 6.7. The shaft is reticulated in 10 different elements with nine spinning hub elements between them. The dissipative coupling between the shaft and drive motor is denoted as R_c and the angular rotation of the shaft is expressed as Ω . The total polar moment of inertia of the shaft can be represented as:

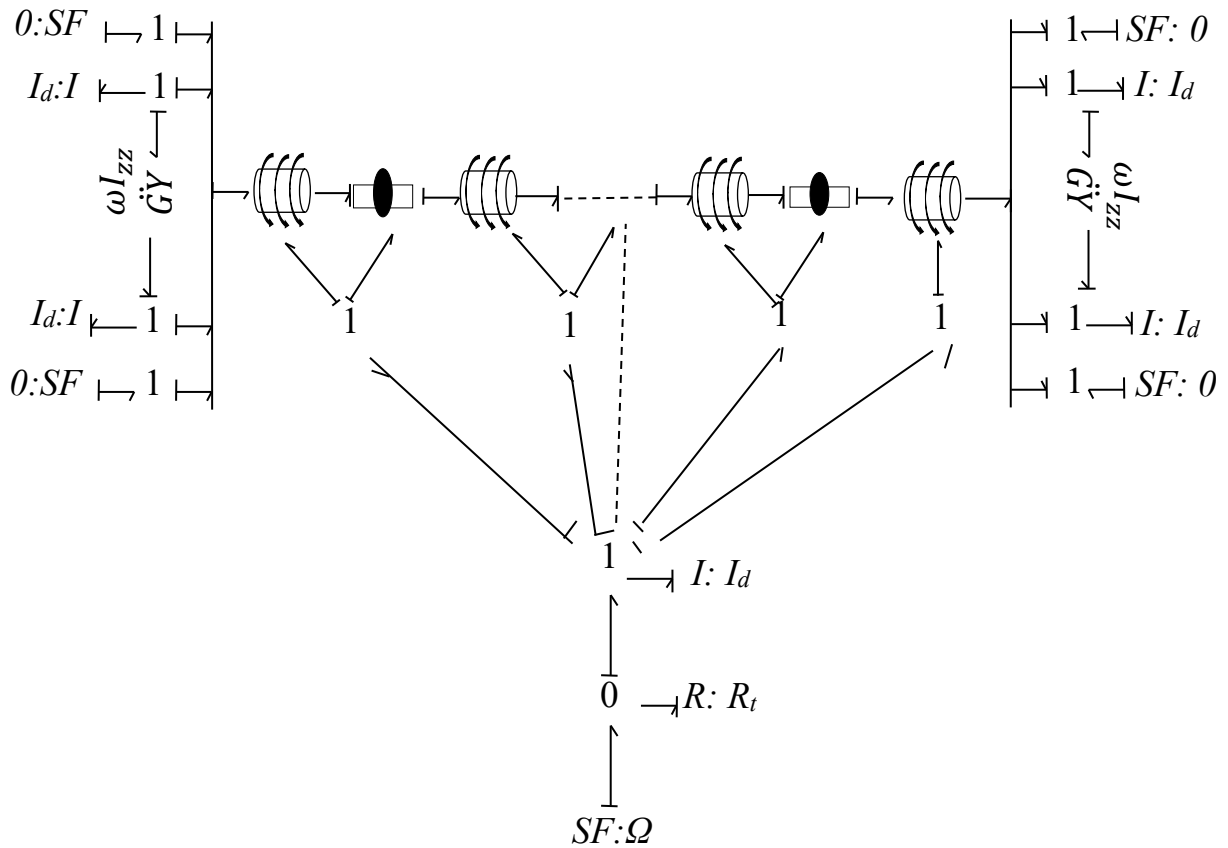


Fig. 6.7: Bond graph model by connecting sub models

$$I_p = \frac{\pi\rho}{8} R^2 * \text{Total length of shaft} \quad (6.11)$$

the end condition are assumed to be pin-pin, where source of flow is zero and inertial element is:

$$I_d = \frac{\pi\rho}{8} L_{elem} R^4 \quad (6.12)$$

where L_{elem} is the length of the reticulate element.

In the present model, the value of polar moment of inertia, moment of inertia, and mass of hub of the hub is considered as zero. The pin-pin end supports are assumed to be isotropic and rigid.

6.2 Simulation

The simulation was performed on a dedicated bond graph software Symbols Shakti Software. using a fourth order Runge-Kutta method. All the object-oriented submodels are connected on bondpad as shown in Fig. 6.7.

Boundary condition for simply supported beam is:

$$\begin{aligned}
 EI \frac{\partial^4 Y(x, t)}{\partial x^4} &= -\rho a \frac{\partial^2 Y(x, t)}{\partial t^2} \\
 Y(0) &= 0 \\
 \left. \frac{\partial^2 Y(x)}{\partial x^2} \right|_{x=0} &= 0 \\
 Y(L) &= 0 \\
 \left. a \frac{\partial^2 Y(x)}{\partial x^2} \right|_{x=L} &= 0
 \end{aligned} \tag{6.13}$$

Dimensions of the shaft, Dissipative coupling coefficient, External damping coefficient of the rotor shaft (μ_a) and number of elements are the parameters whose values are shown in Table 6.1.

Table 6.1 Parameters for simulation.

Parameter	Value
Effective length of the shaft	$L_{\text{beam}} = 660\text{mm}$
Radius of the shaft	$R_o = 11\text{mm}$
Number of reticulated elements	$N_{\text{elem}} = 10$
External damping coefficient of the rotor shaft*	$\mu_a = 3.00e^{-5}, 6.00e^{-4}$ (for modes 1, 2 respectively)

Internal damping coefficient of the rotor shaft*	To be calibrated.
Dissipative coupling coefficient	$R_t = 0.002 \text{ Nms}$

*Damping coefficients are multiplied with EI besides these value.

Parameters that change with the material are Young's modulus, density and internal damping. The values of Young's modulus and density for different materials were calculated through mean field homogenization as provided in previous chapter.

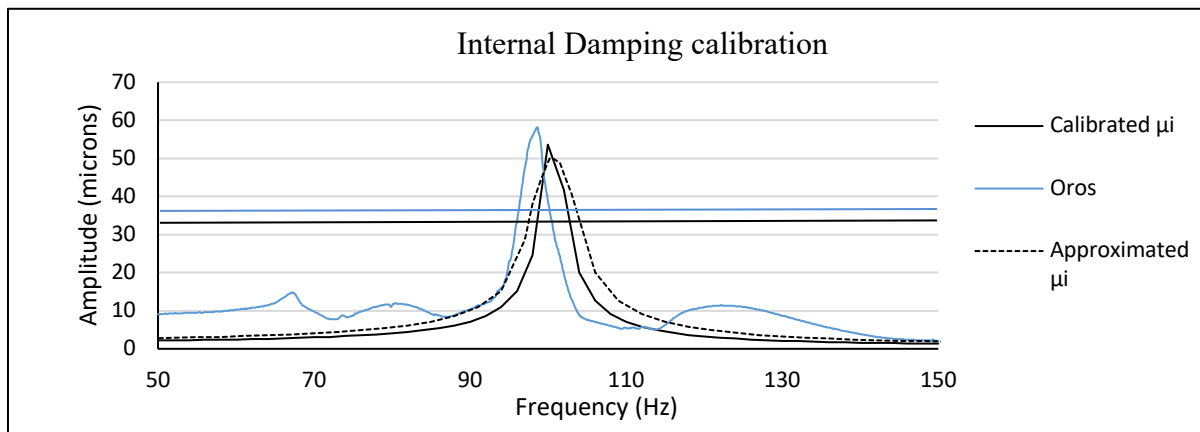


Fig. 6.8: Internal Damping calibration

As reported in various observations and literature, internal damping effects the dynamic behaviour of the rotating shafts. A phenomenon where presence of external and internal damping results in the instability of the shaft above a certain speed, depends on the ratio of the external and internal damping. Also, changing the material of the shaft does not affect the values of external damping significantly. Although, internal damping changes effectively due to the change in the material. So, for simulation calibration of the internal damping coefficient of the shaft has been performed in the present work.

Now, the approximation for the internal damping coefficient (μ_i) has been taken as: -

Approximate value of internal damping coefficient* = $2m\omega_n \xi = 1.3 \times 10^{-3} \text{ Nm/s}$.

*Damping coefficients are multiplied with EI besides these value.

This approximation is based on an assumption of considering the system having single degree of freedom and the source and vectorial position of the damping cannot identified. So,

it is customary to include damping functionally into the bond graph. To incorporate this, the calibrated internal damping is derived by connecting it to the natural response of the rotor.

For calibration of the internal damping coefficient for bond graph, the damping ratio (ξ) calculated experimentally has been mapped with the damping ratio obtained by the bond graph response. Half power bandwidth formulation has been used for both calculations. According to half-power bandwidth formulation, the damping ratio corresponding to these values may be evaluated as

$$\text{Damping factor/ratio}(\xi) = \frac{f_1 - f_2}{2 \times f_{max}} \quad (6.14)$$

Where f_{max} is frequency corresponding to the maximum amplitude value of FRF plots, f_1 and f_2 are the frequencies where the values are square root of the maximum amplitude.

For bond graph analysis, the fft response was extracted by providing a initial displacement of 300 microns and 10 seconds delay. As shown in Fig. 6.8, for Al 6061 there was a huge difference between the damping factors of the experimental and bond graph data. For the other MMC shafts same damping coefficient was taken and the results are shown in Table 6.2.

Table 6.2 Experimental and bond graph Damping ratio for approximate value.

Material	Damping ratio (Experimental)	Damping ratio (Bond graph approximation)	% Error
Al 6061	0.0097	0.0162	67%
6% Al 6061-Al₂O₃	0.0123	0.0162	31%
12 % Al 6061-Al₂O₃	0.0146	0.0162	10.08%
18 % Al 6061-Al₂O₃	0.0172	0.0162	-6.17%

As shown in Table 6.2, the percentage error reduced for composites with higher volume

percentage of reinforcement till 12% Al 6061-Al₂O₃, and the damping ratio was lower than that the experimentally determined damping ratio of the 18% Al 6061-Al₂O₃ composite.

This clearly depicts that the approximated coefficient of internal damping generated the results with indifferent damping ratio (which indicates the internal material damping characteristics) and doesn't consider the composition. So, the internal damping coefficient (μ_i) should be modified in order to get the appropriate result.

Moreover, internal damping coefficient (μ_i) for every MMC compositions will change accordingly. The internal damping is the characteristic of the material property and therefore should be corrected for each material. Since, composites have high imperfections within the structure as compared to the crystalline conventional metals they have a tendency to attain high damping. The higher the reinforcement percentage higher is the amorphous imperfections and higher is the damping in the material. Therefore, it is necessary to calibrate the values of the internal damping so that we can obtain the correct value of the damping ratio.

It is done by mapping the graph of the bond graph response with the experimental response so that for the corresponding value of the internal damping the damping ratio is equal to the experimental value. The calibrated values of the internal damping coefficient (μ_i) is shown in Table 6.3 and the mapped graph plot for all compositions are shown in Fig. 6.9.

Table 6.3 Calibrated internal damping factor for different MMC shaft.

Material	Calibrated μ_i	Damping ratio (Experimental)
Al 6061	6.1×10^{-4}	0.0097
6 % Al 6061-Al ₂ O ₃	6.49×10^{-4}	0.0123
12 % Al 6061-Al ₂ O ₃	6.97×10^{-4}	0.0146
18 % Al 6061-Al ₂ O ₃	7.6×10^{-4}	0.0172

Now the overall response of the static and rotatory response of MMCs shaft can be extracted through Bond graph. Example of Al 6061 shaft displacement response with the calibrated internal damping coefficient (μ_i) are shown in Fig. 6.9.

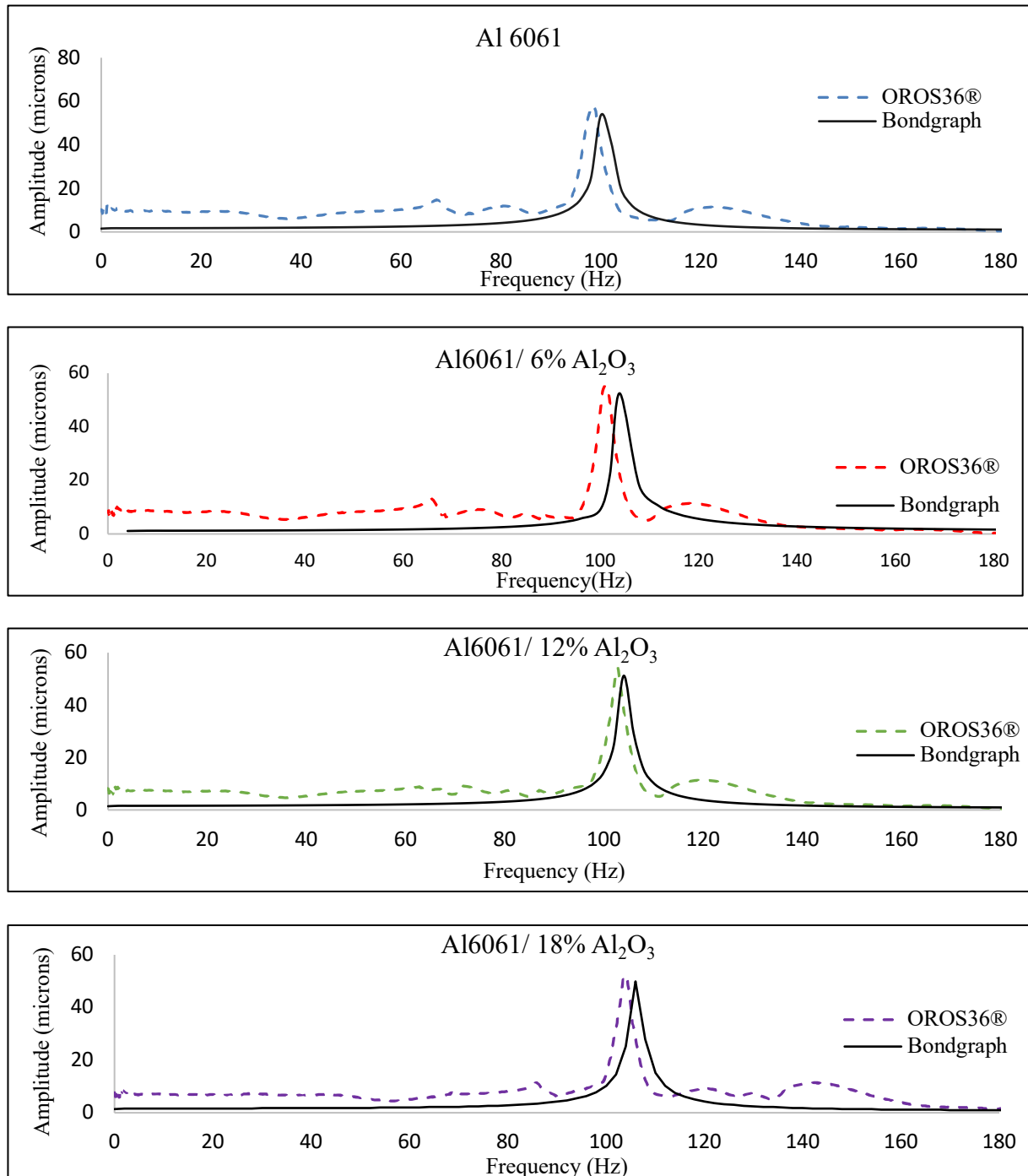


Fig. 6.9. Mapped plots for calibrated internal damping coefficients.

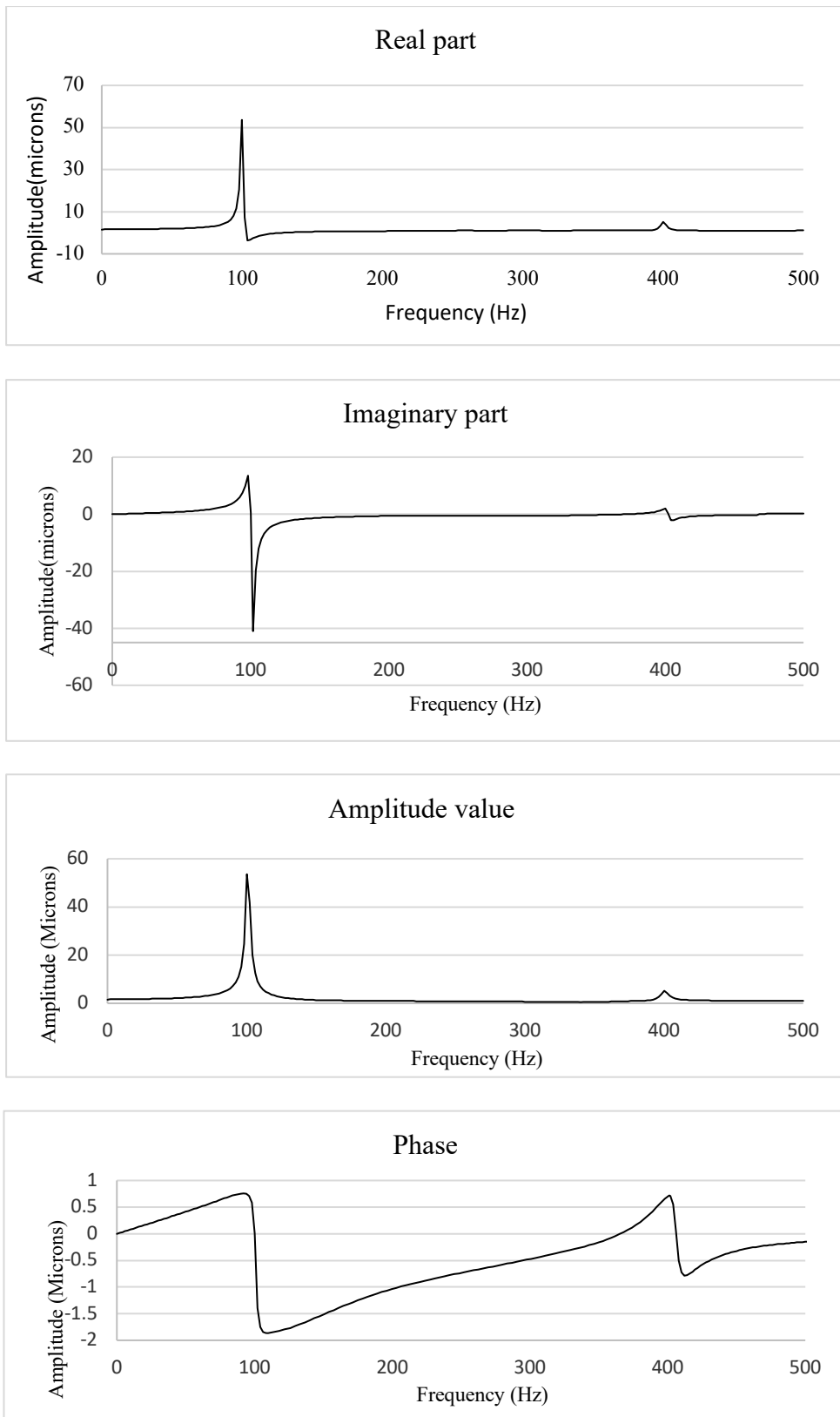


Fig. 6.10: Displacement response for modelling impact hammer response.

Fast Fourier Transform (FFT) response provide the necessary information of the vibration by transforming the time domain data to frequency domain data. From fft an insight into the characteristic response of the shafts of different composite materials are obtained that are also obtained in bond graph analysis.

Fig. 6.10 shows the real and imaginary part, amplitude and phase of the fft response generated by bond graph. The real part is even symmetric and the imaginary part is approximately odd symmetric. The phase change occurs at the frequency of 100Hz and 400 Hz which are in proximity to the Experimental response. The amplitude conforms the resonating effect occurred in the experimental results. Since the values are derived from the first mode of response, the focus is on the first mode of resonance. The bond graph response with initial displacement is shown in Fig. 6.11.

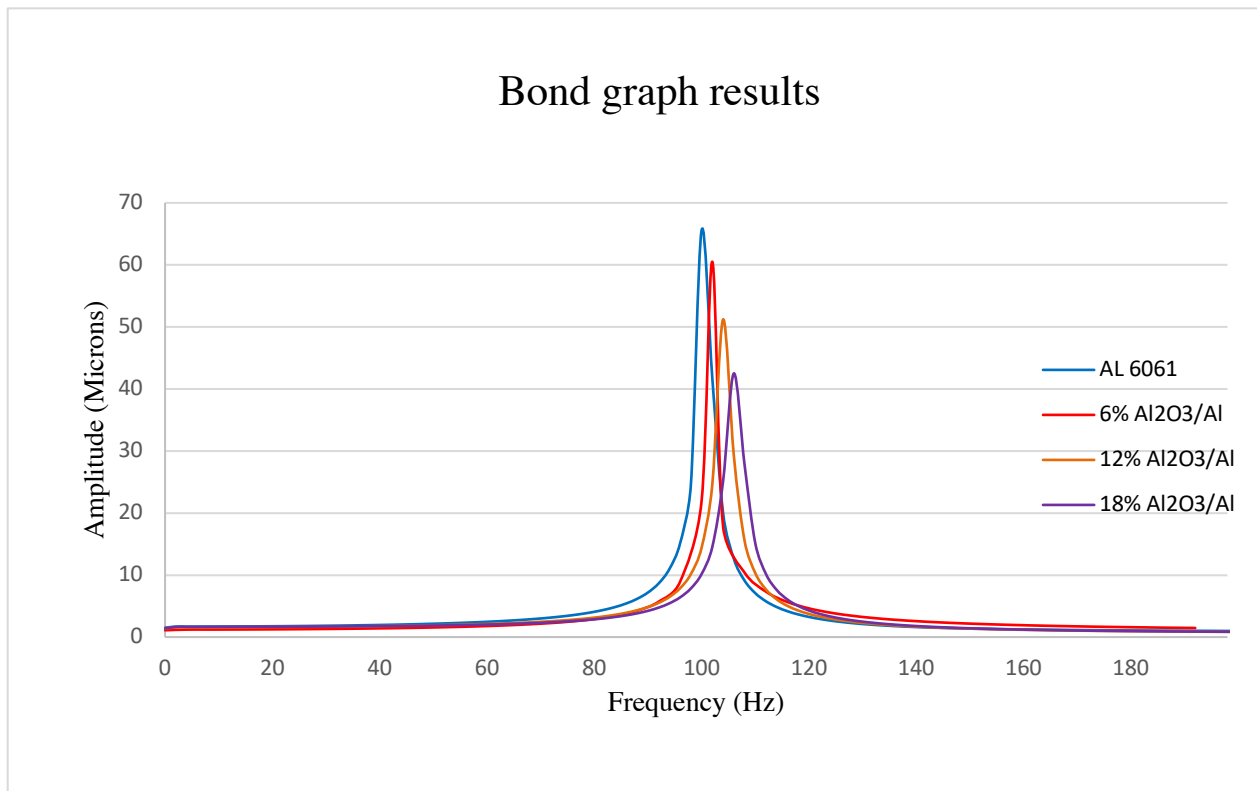


Fig. 6.11: Response for first mode excitation in bond graph

The amplitudes and frequencies of analytical and experimental values are shown in Table 6.4
 Table 6.4 Comparison of result after calibrated internal damping factor for different MMC shaft.

Material	Amplitude (In microns)		Natural frequency (Hz)	
	Experimental	Bond Graph	Experimental	Bond Graph
Al 6061	69.1	65.6	98.62	100 Hz
6 % Al 6061-Al ₂ O ₃	62.7	60.501	101.6	102 Hz
12 % Al 6061-Al ₂ O ₃	52.1	51.2	108.9	110 Hz
18 % Al 6061-Al ₂ O ₃	43.5	42.5	112.9	114 Hz

The trend of amplitude and natural frequencies of the bond graph results was congruent with the experimental results. The amplitudes were reduced for the MMC shafts with higher volume fraction of reinforcements due to the increase in the Young's modulus and stiffness of the shaft. The natural frequency increased for the higher for the MMC shafts with higher volume fraction of reinforcements due to the increase in the specific modulus of the MMCs. It was observed that by the addition of reinforcement upto 18 wt.%, the amplitude can be reduced from 69.1 microns to 43.5 microns. Through simulation it was observed that the amplitude was reduced from 65.6 to 42.5 microns. Although, there are minor differences in the experimental and bond graph values of amplitude and natural frequencies. The value of the amplitudes of the bond graph analysis are less as compared to the experimental values. In addition to that the frequency in the bond graph results are higher than the experimental results. The reason for this may be the porosity induced in the MMC due to the agglomeration of particles and stir casting effect.

The results reveal that better dynamic properties can be attained by increasing the reinforcement percentage into the metal matrix. For further analysis of rotating MMC shafts, the bond graph analysis has been extended to first and second mode of vibrations. The dynamic response for the shafts are characterized by a phenomenon where the spinning speed

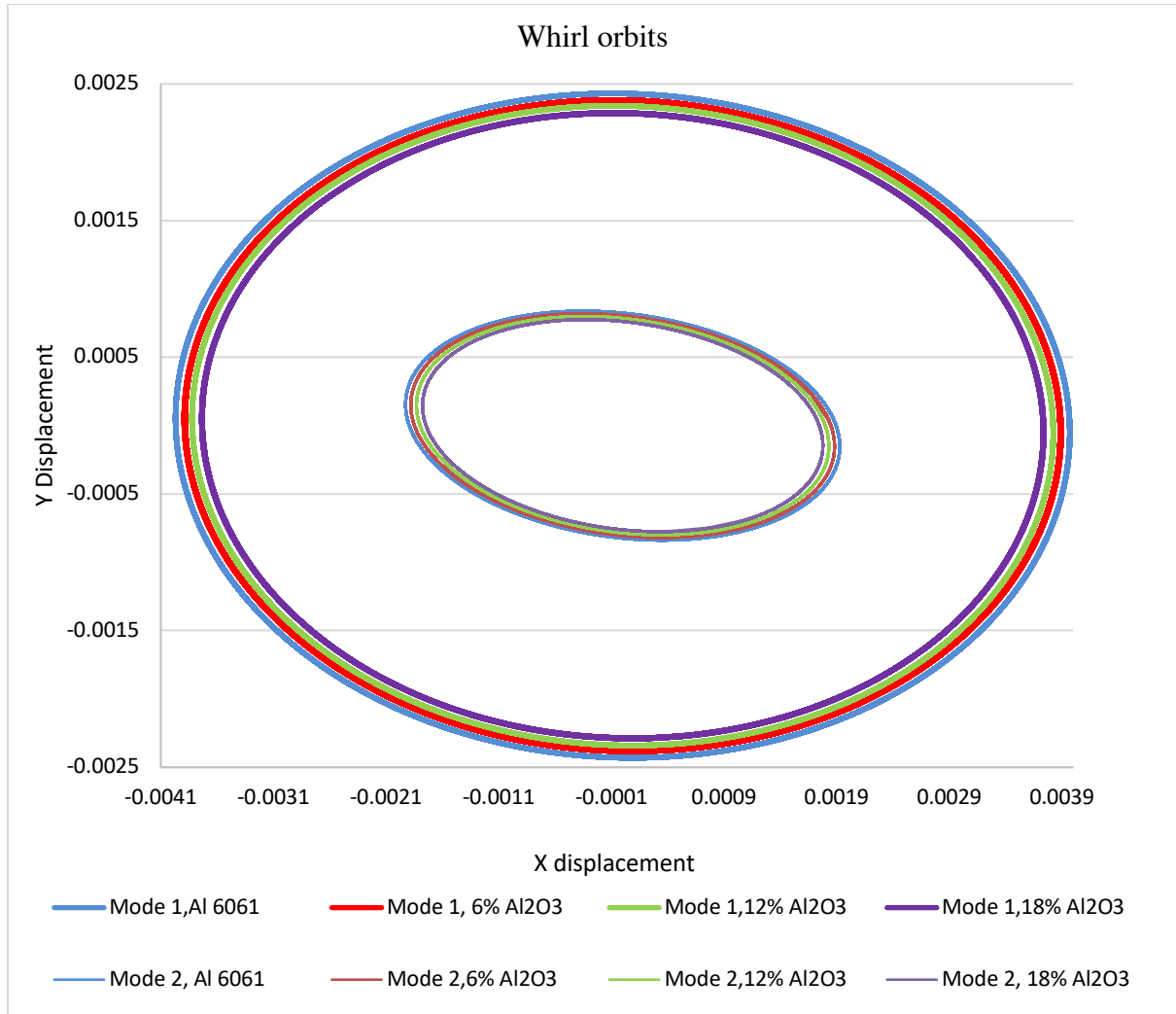


Fig. 6.12: Whirl orbits or the response of the MMC shafts in first and second mode.

of the shaft is entrained to a certain limit. Beyond this, the power induced in the system increases the amplitudes of the transverse vibrations. Moreover, whirl speed of shaft is dependent on the natural frequency and the ratio of the damping coefficients as :-

$$\dot{\theta}_t \leq \Omega_n \left(1 + \frac{\mu_a}{\gamma_n} \right) \quad (6.15)$$

Where $\dot{\theta}_t$ is the shaft entrainment speed, Ω_n is the natural frequency, $\gamma_n = \mu_i \left(\frac{n}{\pi l} \right)^4$, μ_a and μ_i are the coefficient of internal and external damping, n is the mode number and l is the length of the shaft and corresponding amplitude as

$$A_n = \sqrt{\frac{R_c(\Omega - \dot{\theta}_t)}{\gamma_n \Omega_n}} \quad (6.16)$$

A_n is the n th mode amplitude and R_c is the dissipative coupling resistance.

For bond graph simulation the excitation speed has been taken as twice the first natural frequency for mode 1, and twice the second natural frequency for mode 2. The shaft entrainment for both the cases were near the natural frequencies congruent to the Eq. (6.15). The whirl orbit for the response of the MMC shafts in first and second mode are shown in the Fig. 6.12.

The amplitudes of the whirl orbits reduced for composites with higher volume fraction of reinforcement. This may be due to the fact that the internal damping coefficient of the shaft increased and the amplitude is inversely proportional to it. Moreover, natural frequency increases with increased reinforcement percentage resulting in lower difference between the excitation and the entrained frequency. Although entrainment speed is related to internal damping coefficient and may have affected the amplitude response, the shaft is not long enough that this factor may dictate the shaft entrainment. The amplitudes of the second mode were reduced but the trend of reduction in amplitudes with addition of reinforcement remained likely for the same reason.

6.3 Summary

The simulation of the dynamics of the MMC shafts was performed through bond graph analysis. The effective properties such as Young's modulus and density were derived from the mean-field homogenization technique.

- Internal damping coefficient was an important parameter that affects the dynamics of the rotor systems.

- The generalized approximation of the coefficient of internal damping lead to the error in the damping ratio response from the experimental data.
- So, the internal damping coefficient was calibrated for further dynamic analysis. The unit displacement (obtained through simulation) and impact hammer responses (obtained by experiment) were in proximity to each other.
- Further, the dynamic response for MMC rotating shafts was simulated by taking the effective parameters through calibrated and mean field homogenized values.
- The shaft speed entrained were near to the corresponding modal natural frequencies.
- The internal damping and high stiffness due to the addition of the reinforcement in the composite results in the lower amplitude of the orbitals for composites with higher percentage of reinforcement.
- The orbital response shows that the amplitude of the shafts were reduced for MMCs with higher alumina percentage.

The next chapter shall attempt to enlist conclusion and future scope of present experimental investigation.

Conclusion and Scope for Future Work

7.1 Conclusion

7.1.1 Material and method

- Metal matrix composites with aluminium 6061 and alumina as reinforcement have been used for rotor applications.
- The stir casting method was adopted as it is one of the most cost-effective and flexible methods of the development of metal matrix composites.

7.1.2 Development of metal matrix composites

- The parameters for the stir casting set up were optimized by quantitative analysis of the SEM images.
- The experimental response values of D_{index} and area fraction were significantly fitted and formed a quadratic equation.
- The ANOVA analysis confirms the significance of the model, with a 99.99 % confidence level.
- Stirring RPM and stirring time were more significant as compared to the furnace temperature and preheat temperature for D_{index} and area fraction.
- A significant improvement was obtained for responses at optimized parameters due to the formation of semi solid-state of melt. This state results in both better homogeneity and incorporation of particles in the melt.

- EDS maps replicate the binary image with some error due to misinterpretation of pores to particles during binary conversions.

7.1.3 Characterization of metal matrix composite

- The metal matrix composites with a step addition of 6 wt. % were used for the characterization viz. Al6061, Al 6061/ 6 wt. % Al_2O_3 , Al 6061/ 12 wt. % Al_2O_3 , Al 6061/ 18 wt. % Al_2O_3 and Al 6061/ 24 wt. % Al_2O_3
- Grain refinement was observed for the composites having high wt.% of reinforcement through optical microscopy.
- Microhardness was increased due to the increase of the reinforcement in the composite.
- SEM analysis, along with XRD analysis, confirmed the presence of alumina in the composites.
- For 24% Al_2O_3 / Al 6061 material, a high level of porosity due to agglomeration was observed at the microscopic level.
- The effect of agglomeration and porosity leads to the depletion of tensile strength for 24% Al_2O_3 / Al 6061 material.

7.1.4 Computation and experimental validation of effective properties

- The addition of alumina particles results in the strengthening of composite specimens due to enhanced dislocation density and precipitation hardening.
- The volume fraction of the alumina particles observed by the image analysis method was significantly less as compared to the added volume fraction during fabrication. It suggests that the volume fraction added initially during fabrication should not be used directly for predicting the effective properties.

- The difference between the In-Plane and transverse effective properties is negligible since the strengthening effect of reinforcement is not directionally dependent due to the random orientation of particles.
- The addition of alumina particles in the Al6061 matrix leads to a substantial improvement in the bending stiffness as compared to the material density. Due to this reason, the natural frequency for various modes of vibration increased with the addition of particles.
- The damping ratio also increased on the addition of alumina particles due to the grain refinement and formation of secondary phases.
- The range of mean-field values lags behind the experimental values as the material of high reinforcement composition is used. It can be concluded that the upper bound of mean-field homogenization can be used for the material of high reinforcement composition and can be the future scope of work. However, mean-field homogenization predicts a low higher than experimental value while assuming that all alumina particles added for the process are mixed into the matrix.

7.1.5 Dynamic analysis of MMC rotor

- Bond graph modelling was used to simulate the dynamic response of the metal matrix composite rotors
- The generalized approximation of the coefficient of internal damping leads to the error in the damping ratio response from the experimental data.
- The calibrated internal damping was used, and the results were congruent to the experimental results.
- The shaft speed entrained were near to the corresponding modal natural frequencies.

- The internal damping and high stiffness due to the addition of the reinforcement in the composite results in the lower amplitude of the orbitals for composites with a higher percentage of reinforcement.
- The orbital response shows that the amplitude of the shafts was reduced for MMCs with higher alumina percentage.

7.2 Future Scope

- Hybrid composites using multiple reinforcements can be explored in future.
- Specific techniques of noise reduction in EDS maps can be utilized so that the porosity effect can also be considered during quantitative analysis.
- Samples were taken from the end of the shaft for SEM analysis; this might be the low/high composition area of the shaft during casting. This variation can be addressed in future work.
- Investigation on how the reinforcement of a matrix material can hamper the development and increase of cracks in MMC rotors and can increase the mean time to failure.

REFERENCES

- [1] World Economic Forum (WEF), Global manufacturing index January 2018.
- [2] Global Manufacturing Competitiveness Index, 2016.
- [3] Clyne, T. W., & Hull, D. (2019). *An Introduction to Composite Materials*. doi: 10.1017/9781139050586
- [4] Naslain, R. R., & Pomeroy, M. (2016). *Ceramic Matrix Composites: Matrices and Processing*. Reference Module in Materials Science and Materials Engineering. doi:10.1016/b978-0-12-803581-8.02317-1
- [5] Dai, D., & Fan, M. (2014). Wood fibres as reinforcements in natural fibre composites: structure, properties, processing and applications. *Natural Fibre Composites*, 3–65. doi:10.1533/9780857099228.1.3
- [6] Ehrlich, H., Janussen, D., Simon, P., Bazhenov, V. V., Shapkin, N. P., Erler, C., Vournakis, J. N. (2008). Nanostructural Organization of Naturally Occurring Composites—Part II: Silica-Chitin-Based Biocomposites. *Journal of Nanomaterials*, 2008, 1–8. doi:10.1155/2008/670235
- [7] Taylor, D. (2007). *Composites. The Theory of Critical Distances*, 141–161. doi:10.1016/b978-008044478-9/50009-0
- [8] Yashas Gowda, T. G., Sanjay, M. R., Subrahmanya Bhat, K., Madhu, P., Senthamarai kannan, P., & Yogesha, B. (2018). Polymer matrix-natural fiber composites: An overview. *Cogent Engineering*, 5(1), 1446667. doi:10.1080/23311916.2018.1446667
- [9] Lauge Fuglsang Nielsen. (2005). Elastic properties of two-phase materials. *Materials Science and Engineering*, 52(1), 39–62. doi:10.1016/0025-5416(82)90068-4
- [10] Chawla, K. K. (2019). *Matrix Materials*. *Composite Materials*, 75–105. doi:10.1007/978-3-030-28983-6_3
- [11] Barbero, E. J. (2017). *Introduction to Composite Materials Design*. doi:10.1201/9781439894132 CRCpress.
- [12] Kumlutas, D. (2003). Thermal conductivity of particle filled polyethylene composite materials. *Composites Science and Technology*, 63(1), 113–117. doi:10.1016/s0266-3538(02)00194-x
- [13] Dixit, S., Goel, R., Dubey, A., Shivhare, P. R., & Bhalavi, T. (2017). Natural Fibre Reinforced Polymer Composite Materials - A Review. *Polymers from Renewable Resources*, 8(2), 71–78. doi:10.1177/204124791700800203
- [14] Kumar D.T., Prasad K.V., & Rao R.P.S. (2016). Tensile and Impact properties of jute/glass and jute/carbon fiber reinforced polypropylene, 4(3), 35–9. *Journal of Polymer & Composites*

- [15] Gan, Y., Solomon, D., & Reinbolt, M. (2010). Friction Stir Processing of Particle Reinforced Composite Materials. *Materials*, 3(1), 329–350. doi:10.3390/ma3010329
- [16] Gopalakrishnan, S., & Murugan, N. (2012). Production and wear characterisation of AA 6061 matrix titanium carbide particulate reinforced composite by enhanced stir casting method. *Composites Part B: Engineering*, 43(2), 302–308. doi:10.1016/j.compositesb.2011.08.049
- [17] Kakani S. and Kakani A. (2004), “Material science”; New Delhi, New age international publishers, 593-613.
- [18] Mallick, P. K. (2010). Preface. *Materials, Design and Manufacturing for Lightweight Vehicles*, xi–xii. doi:10.1016/b978-1-84569-463-0.50014-6
- [19] David, W.R. & William E.L. (2018). *Modern ceramic engineering: properties, processing, and use in design*. 4th ed. Taylor & Francis Group; <http://dx.doi.org/10.1201/9780429488245>.
- [20] Benzait, Z., & Trabzon, L. (2018). A review of recent research on materials used in polymer–matrix composites for body armor application. *Journal of Composite Materials*, 52(23), 3241–3263. doi:10.1177/0021998318764002
- [21] Koczak, M. J., Khatri, S. C., Allison, J. E., & Bader, M. G. (2013). Metal-Matrix Composites for Ground Vehicle, Aerospace, and Industrial Applications. *Fundamentals of Metal-Matrix Composites*, 297–326. doi:10.1016/b978-0-08-052371-2.50020-1
- [22] Rohatgi, P. (1991). Cast aluminum-matrix composites for automotive applications. *JOM*, 43(4), 10–15. doi:10.1007/bf03220538
- [23] Prasad, S. V., & Asthana, R. (2004). Aluminum Metal–Matrix Composites for Automotive Applications: Tribological Considerations. *Tribology Letters*, 17(3), 445–453. doi:10.1023/b:tril.0000044492.91991.f3
- [24] Clementson, A. (1994). *An Introduction to Metal Matrix Composites* T. W. Clyne and P. J. Withers. Cambridge University Press, The Pitt Building, Trumpington Street, Cambridge CB2 1RP. 509pp. Illustrated. *The Aeronautical Journal*, 98(973), 106. doi:10.1017/s0001924000050120
- [25] Hunt, W.H. & Miracle, D.B. (2001). Automotive applications of metal matrix composites, *ASM handbook*, Donaldson SL, editors, Composites,21. Materials Park: ASM International, 1029–1032.
- [26] Kaczmar, J. W., Pietrzak, K., & Włosiński, W. (2000). The production and application of metal matrix composite materials. *Journal of Materials Processing Technology*, 106(1-3), 58–67. doi:10.1016/s0924-0136(00)00639-7
- [27] Babu, P. E. J., Pillai, U. T. S., Pai, B. C., & Savithri, S. (2004). Application of the generalized method of cells principle to particulate-reinforced metal matrix composites. *Metallurgical and Materials Transactions B*, 35(6), 1029–1039. doi:10.1007/s11663-004-0059-8.
- [28] Zinberg, H. & Symmonds, M.F. (1970). The development of an advanced composite tail rotor driveshaft, 26th Annual National Forum of American Helicopter Society, Washington, D.C.

- [29] Bauchau, O. A. (1981). Optimal Design of High Speed Rotating Graphite/Epoxy Shafts. *Journal of Composite Materials*, 17(2), 170–181. doi:10.1177/002199838301700205
- [30] Zorzi, E. S. & Giordano, J. C. (1985). Composite shaft rotor dynamic evaluation , ASME Design Engineering Conference on Mechanical Vibrations and Noise, 85-DET-114, 1–8,
- [31] Gubran, H.B.H. (2000). Dynamic stress analysis and optimization studies on fibre-reinforced Composite shafts, Ph.D. thesis, Mechanical engineering department, Indian Institute of Technology (IIT) Delhi, India.
- [32] Sino, R., Chatelet, E., Montagnier, O., & Jacquet-Richardet, G. (2006). Dynamic Instability Analysis of Internally Damped Rotors. Volume 5: Turbo Expo 2007. doi:10.1115/gt2007-27073
- [33] Miracle, D. (2005). Metal matrix composites – From science to technological significance. *Composites Science and Technology*, 65(15-16), 2526–2540. doi:10.1016/j.compscitech.2005.05.027
- [34] Nturanabo, F., Masu, L., & Baptist Kirabira, J. (2019). Novel Applications of Aluminium Metal Matrix Composites. *Aluminium Alloys and Composites*. doi:10.5772/intechopen.86225
- [35] Ekinci, V. S., Bağcı, C., & Arik, H. (2014). Effect of Al₂O₃ content and Milling Time on Microstructure and Mechanical Properties of Aluminum Metal Matrix Composites. *Experimental Techniques*, 38(2), 66–73. doi:10.1111/j.1747-1567.2011.00790.x
- [36] Sarina, B., Tang, K., Kvithyld, A., Engh, T., & Tangstad, M. (2012). Wetting of pure aluminium on graphite, SiC and Al₂O₃ in aluminium filtration. *Transactions of Nonferrous Metals Society of China*, 22(8), 1930–1938. doi:10.1016/s1003-6326(11)61410-6
- [37] Va, B. , Nagaralb, M., Auradib, V. and Koric, S. (2014). Preparation of 6061Al- Al₂O₃ MMC's by Stir Casting and Evaluation of Mechanical and Wear Properties , *Procedia Materials Science* 6 1658 – 1667.
- [38] Mazaherya, Abdizadeha, H. & Baharvandi R. (2009). Development of high-performance A356/nano- Al₂O₃ composites *Materials Science and Engineering A* 518, 61–64.
- [39] Kanga Y. & Chan S.(2004). Tensile properties of nanometric Al₂O₃ particulate-reinforced aluminum matrix composites, *Materials Chemistry and Physics*, 85, 2(3), 438–443.
- [40] Khorshid, M., Jahromi, S., & Moshksar, M. (2010). Mechanical properties of tri-modal Al matrix composites reinforced by nano- and submicron-sized Al₂O₃ particulates developed by wet attrition milling and hot extrusion, *Materials & Design* Volume 31, 8, Pages 3880–3884.
- [41] Mazen, A. & Ahmed, A. (1998). Mechanical Behaviour of Al- Al₂O₃ MMC Manufactured by PM Techniques Part I—Scheme I Processing Parameters *ASM International*, 7(3) June pp. 393-401.
- [42] Park, B. & Crosky, G. (2001). Material characterization and mechanical properties of Al₂O₃ -Al metal matrix composites, *Journal of Materials Science*, 36, 2417 – 2426.
- [43] Daoud, A., El-Bitar, T., and Abd El-Azim A. (2003). Tensile and Wear Properties of Rolled Al₅Mg- Al₂O₃ or SiC Particulate Composites, *ASM International* Volume 12(4) pp. 390-397.17.

- [44] Saiza, E., Tomsiaa, A. & Sukanuma, K. (2003). Wetting and strength issues at Al/ α -alumina interfaces, *Journal of the European Ceramic Society*, 23, 2787–2796.
- [45] Aqida, S., Ghazali, M., Hashim, J. (2004). Effects of porosity on mechanical properties of metal matrix composite: An Overview, *Universiti Teknologi Malaysia* 40(A) Jun. ,17–32.
- [46] Meguid, A. & Sun, Y., (2004) On the tensile and shear strength of nano-reinforced composite interfaces, *Materials and Design*, 25, 289–296.
- [47] Lu, H., Hu, J., Chen, C., Sun, H., Hu, X. & Yang, D. (2005) Characterization of Al₂O₃ – Al nano-composite powder prepared by a wet chemical method, Published by Elsevier Ltd and Techna Group Ceramics International ,31,481–485.
- [48] Razavi, Hesabi, Z., Hafizpour, H., Simchi, A. (2007). An investigation on the compressibility of aluminium/nano-alumina composite powder prepared by blending and mechanical milling, *Materials Science and Engineering A*, 454, 89–98.
- [49] Durai, T., Das, K. & Das S. (2007). Wear behaviour of nano structured Al (Zn)/ Al₂O₃ and Al (Zn)–4Cu/Al₂O₃ composite materials synthesized by mechanical and thermal process, *Materials Science and Engineering A*, 471, 88–94.
- [50] Zhang, F. C., Luo, H. H., Wang, T. S., Roberts, S. G., & Todd, R. I. (2008). Influence factors on wear resistance of two alumina matrix composites. *Wear*, 265(1-2), 27–33. doi:10.1016/j.wear.2007.08.011
- [51] Mula, S., Padhi, P., Panigrahi, S. C., Pabi, S. K., & Ghosh, S. (2009). On structure and mechanical properties of ultrasonically cast Al–2% Al₂O₃ nanocomposite. *Materials Research Bulletin*, 44(5), 1154–1160. doi:10.1016/j.materresbull.2008.09.040
- [52] Mazahery, A., Abdizadeh, H., & Baharvandi, H. R. (2009). Development of high-performance A356/nano- Al₂O₃ composites. *Materials Science and Engineering: A*, 518(1-2), 61–64. doi:10.1016/j.msea.2009.04.014
- [53] Reddy, C & Zitoun, E. (2010). Tensile behaviour of 6063/ Al₂O₃ particulate metal matrix composites fabricated by investment casting process, *International Journal of Applied Engineering Research*, Dindigul, 1(3), 542-552.
- [54] Mazahery, A., & Ostadshabani, M. (2011). Investigation on mechanical properties of nano-Al₂O₃-reinforced aluminum matrix composites. *Journal of Composite Materials*, 45(24), 2579–2586. doi:10.1177/0021998311401111
- [55] Ezatpour, H. R., Torabi-Parizi, M., & Sajjadi, S. A. (2013). Microstructure and mechanical properties of extruded Al/Al₂O₃ composites fabricated by stir-casting process. *Transactions of Nonferrous Metals Society of China*, 23(5), 1262–1268. doi:10.1016/s1003-6326(13)62591-1
- [56] Soltani, S., Azari Khosroshahi, R., Taherzadeh Mousavian, R., Jiang, Z.-Y., Fadavi Boostani, A., & Brabazon, D. (2017). Stir casting process for manufacture of Al–SiC composites. *Rare Metals*, 36(7), 581–590. doi:10.1007/s12598-015-0565-7
- [57] Pazhouhanfar, Y., & Eghbali, B. (2018). Microstructural characterization and mechanical properties of TiB₂ reinforced Al6061 matrix composites produced using stir casting process. *Materials Science and Engineering: A*, 710, 172–180. doi:10.1016/j.msea.2017.10.087

- [58] Chauhan, M. H., Irfan, M., & Chauhan, M. A. (2017). Variation of mechanical properties (tensile strength & microstructure) of Al6061/(Al₂O₃ and fly-ash), hybrid metal matrix composite produced by stir casting. *International Research Journal of Engineering and Technology*, 4 (7), 2407-2414.
- [59] Ahmed, O. & Mohamed, O. (2019). Synthesis and Characterization of Al6061 / Al₂O₃ Metal Matrix Nanocomposites Fabricated by Stir-casting, PhD Thesis, Beni Suef University, Egypt.
- [60] Pitchayapillai, G., Seenikannan, P., Raja, K., & Chandrasekaran, K. (2016). Al6061 Hybrid Metal Matrix Composite Reinforced with Alumina and Molybdenum Disulphide. *Advances in Materials Science and Engineering*, 2016, 1–9. doi:10.1155/2016/6127624
- [61] Haslam, M. D., & Raeymaekers, B. (2013). A composite index to quantify dispersion of carbon nanotubes in polymer-based composite materials. *Composites Part B: Engineering*, 55(1), 16–21. <https://doi.org/10.1016/j.compositesb.2013.05.038>
- [62] Yazdanbakhsh, A., Grasley, Z., Tyson, B., & Abu Al-Rub, R. K. (2011). Dispersion quantification of inclusions in composites. *Composites Part A: Applied Science and Manufacturing*, 42(1), 75–83. <https://doi.org/10.1016/j.compositesa.2010.10.005>
- [63] Slipenyuk A, Kuprin V, Milman Y, Spowart JE, Miracle DB. (2004). The effect of matrix to reinforcement particle size ratio (PSR) on the microstructure and mechanical properties of P/M processed AlCuMn/SiCp MMC. *Mater Sci Eng, A*; 381(1–2):165–70.
- [64] Jahedi, M., Paydar, M. H., & Knezevic, M. (2015). Enhanced microstructural homogeneity in metal-matrix composites developed under high-pressure-double-torsion. *Materials Characterization*, 104, 92–100. <https://doi.org/10.1016/j.matchar.2015.04.012>
- [65] Luo, Z. P. & Koo, J. H. (2008). Quantitative study of the dispersion degree in carbon nanofiber/polymer and carbon nanotube/polymer nanocomposites. *Materials Letters*, 62(20), 3493–3496. <https://doi.org/10.1016/j.matlet.2008.03.010>
- [66] Yakaboylu, G. A., & Sabolsky, E. M. (2017). Determination of a homogeneity factor for composite materials by a microstructural image analysis method. *Journal of Microscopy*, 266(3), 263–272. <https://doi.org/10.1111/jmi.12536>
- [67] Ferreira, S. L. C., Bruns, R. E., Ferreira, H. S., Matos, G. D., David, J. M., Brandão, G. C., dos Santos, W. N. L. (2007). Box-Behnken design: An alternative for the optimization of analytical methods. *Analytica Chimica Acta*, 597(2), 179–186. <https://doi.org/10.1016/j.aca.2007.07.011>
- [68] Gopalakrishnan, S., & Murugan, N. (2012). Production and wear characterisation of AA 6061 matrix titanium carbide particulate reinforced composite by enhanced stir casting method. *Composites Part B: Engineering*, 43(2), 302–308. <https://doi.org/10.1016/j.compositesb.2011.08.049>
- [69] Kumar, V., & Sharma, V. (2019). Effects of SiC, Al₂O₃, and ZrO₂ particles on the LBMed characteristics of Al/SiC, Al/Al₂O₃, and Al/ZrO₂ MMCs prepared by stir casting process, *Particulate Science and Technology*, 37:6, 766-776, DOI: 10.1080/02726351.2018.1445152
- [70] Ravi, B., Naik, B. B., & Prakash, J. U. (2015). Characterization of Aluminium Matrix Composites (AA6061/B4C) Fabricated by Stir Casting Technique. *Materials Today: Proceedings*, 2(4-5), 2984–2990. doi:10.1016/j.matpr.2015.07.282

- [71] Pradhan, S. K., Chatterjee, S., Mallick, A. B., & Das, D. (2016). A simple stir casting technique for the preparation of in situ Fe-aluminides reinforced Al-matrix composites. *Perspectives in Science*, 8, 529–532. doi:10.1016/j.pisc.2016.06.011
- [72] Tanaka, K. (2019). The $\cos\alpha$ method for X-ray residual stress measurement using two-dimensional detector. *Mechanical Engineering Reviews*, 6(1), 18-00378.
- [73] Noyan, I. C., & Cohen, J. B. (1987). Residual stress – measurement by diffraction and interpretation. Springer Series on Materials Research and Engineering, edited by B. Ilshner and N. J. Grant. Springer-Verlag, New York-Berlin-Heidelberg-London-Paris-Tokyo 1987, 276 Seiten, 160 Bilder, 31 Tabellen, DM 138. –, ISBN 3-540-96378-2. *Crystal Research and Technology*, 24(2), K37–K37. doi:10.1002/crat.2170240228
- [74] Akiniwa, Y., & Kimura, H. (2008). Determination of Residual Stress Distribution in Severe Surface Deformed Steel by Shot Peening. *Materials Science Forum*, 571-572, 15–20. doi:10.4028/www.scientific.net/msf.571-572.15
- [75] Wang, J.-S., Hsieh, C.-C., Lai, H.-H., Kuo, C.-W., Wu, P. T.-Y., & Wu, W. (2015). The relationships between residual stress relaxation and texture development in AZ31 Mg alloys via the vibratory stress relief technique. *Materials Characterization*, 99, 248–253. doi:10.1016/j.matchar.2014.09.019
- [76] Wang, B., & Qu, S. (2018). Comparison of residual stress before and after shot peening on the surface of a Ti-6Al-4V titanium alloy by μ -X360n equipment. In *IOP Conference Series: Materials Science and Engineering* (Vol. 397, No. 1, p. 012112). IOP Publishing.
- [77] Chatterjee, S., Ghosh Sur, S., Bandyopadhyay, S., & Basumallick, A. (2015). Effect of microstructure and residual stresses on nano-tribological and tensile properties of Al₂O₃- and SiC-reinforced 6061-Al metal matrix composites. *Journal of Composite Materials*, 50(19), 2687–2698. doi:10.1177/0021998315611481
- [78] Eshelby, J.D. (1957). The determination of the elastic field of an ellipsoidal inclusion, and related problems. *Proceedings of the Royal Society of London. Series A. Mathematical and Physical Sciences*, 241(1226), 376–396. doi:10.1098/rspa.1957.0133
- [79] Christensen, R. M., & Waals, F. M. (1972). Effective Stiffness of Randomly Oriented Fibre Composites. *Journal of Composite Materials*, 6(3), 518–535. doi:10.1177/002199837200600307
- [80] Mori, T., & Tanaka, K. (1973). Average stress in matrix and average elastic energy of materials with misfitting inclusions. *Acta Metallurgica*, 21(5), 571–574. doi:10.1016/0001-6160(73)90064-3
- [81] Benveniste, Y. (1987). A new approach to the application of Mori-Tanaka's theory in composite materials. *Mechanics of materials*, 6(2), 147-157.
- [82] Abaimov, S. G., Trofimov, A., Sergeichev, I. V., & Akhatov, I. S. (2019). Multi-step homogenization in the Mori-Tanaka-Benveniste theory. *Composite Structures*, 223, 110801. doi:10.1016/j.compstruct.2019.03.073
- [83] Imani, S. M., Goudarzi, A. M., Rabiee, S. M., & Dardel, M. (2018). The modified Mori-Tanaka scheme for the prediction of the effective elastic properties of highly porous ceramics. *Ceramics International*, 44(14), 16489–16497. doi:10.1016/j.ceramint.2018.06.066

- [84] Gubran, H. & Gupta K. (2014). Design Optimization of Automotive Propeller Shafts, *Journal of Vibration Engineering and technologies*, 2(1), 35-45
- [85] Elomari, S., Boukhili, R., Skibo, M. D., & Masounave, J. (1995). Dynamic mechanical analysis of prestrained Al₂O₃/Al metal-matrix composite. *Journal of Materials Science*, 30(12), 3037–3044. doi:10.1007/bf01209214
- [86] Zhang, J., Perez, R. J., & Lavernia, E. J. (1993). Documentation of damping capacity of metallic, ceramic and metal-matrix composite materials. *Journal of Materials Science*, 28(9), 2395–2404. doi:10.1007/bf01151671
- [87] Ozmen Eruslu, S., & Aydogdu, M. (2007). Vibration Analysis of Inclusion Reinforced Composite Square Plates under Various Boundary Conditions. *Journal of Reinforced Plastics and Composites*, 28(8), 995–1012. doi:10.1177/0731684407087741
- [88] Luan, X., Sha, Y., Zhao, R., Jia, Q., Zhao, F., & Luo, L. (2015). Vibration Modal Analysis of Continuous Fiber Reinforced Metal Matrix Composites Low Pressure Turbine Shaft. *Proceedings of the 2015 International Power, Electronics and Materials Engineering Conference*. doi:10.2991/ipemec-15.2015.184
- [89] Chang, C.Y., Chang, M.Y., & Huang, J. H. (2004). Vibration analysis of rotating composite shafts containing randomly oriented reinforcements. *Composite Structures*, 63(1), 21–32. doi:10.1016/s0263-8223(03)00121-1
- [90] Beaman, J. J. & Paynter H. M. (1993) *Modelling of Physical Systems*, unpublished, 3, 69-71.
- [91] Campos, J., Crawford, M., & Longoria, R. (2005). Rotordynamic modeling using bond graphs: modeling the Jeffcott rotor. *IEEE Transactions on Magnetics*, 41(1), 274–280. doi:10.1109/tmag.2004.838924
- [92] Hubbard, M. (1979). Whirl Dynamics of Pendulous Flywheels Using Bond Graphs. *Journal of the Franklin Institute*, 308(4), 405–421. doi:10.1016/0016-0032(79)90067-x
- [93] Rastogi, V., Mukherjee, A., & Dasgupta, A. (2011). Dynamic modeling of rotor shaft with internal damping driven through a dissipative coupling. *International Journal of Modeling, Simulation, and Scientific Computing*, 02(01), 105–129. doi:10.1142/s1793962311000396
- [94] Borutzky, W. (2010), *Bond Graph Methodology – Development and Analysis of Multidisciplinary Dynamic System Models.*, Springer, London, ISBN: 978-1-84882-881-0, DOI:10.1007/978-1-84882-882-7.
- [95] Karthikeyan, M., Bisoi, A., Samantaray, A. K., & Bhattacharyya, R. (2015). Sommerfeld effect characterization in rotors with non-ideal drive from ideal drive response and power balance. *Mechanism and Machine Theory*, 91, 269–288. doi:10.1016/j.mechmachtheory.2015.04.016
- [96] Banerjee, J. R., & Su, H. (2006). Dynamic stiffness formulation and free vibration analysis of a spinning composite beam. *Computers & Structures*, 84(19-20), 1208–1214. doi:10.1016/j.compstruc.2006.01.023
- [97] Sino, R., Baranger, T. N., Chatelet, E., & Jacquet, G. (2008). Dynamic analysis of a rotating composite shaft. *Composites Science and Technology*, 68(2), 337–345. doi:10.1016/j.compscitech.2007.06.019

- [98] Kafi, H. R., & Hosseini, S. A. A. (2019). Dynamic analysis of nonlinear rotating composite shafts excited by non-ideal energy source. *ZAMM - Journal of Applied Mathematics and Mechanics / Zeitschrift Für Angewandte Mathematik Und Mechanik*, 99(5), e201800279. doi:10.1002/zamm.201800279
- [99] Bajpai, R. P., Chandrasekhar, U., & Arankalle, A. R. (Eds.). (2014). *Innovative Design, Analysis and Development Practices in Aerospace and Automotive Engineering. Lecture Notes in Mechanical Engineering*. doi:10.1007/978-81-322-1871-5
- [100] Vipin A. J., Kumar, H., & Desai, V. (2019). Dynamic analysis and optimization of SiC reinforced Al6082 and Al7075 MMCs. *Materials Research Express*, 6(5), 056528. doi:10.1088/2053-1591/ab038e
- [101] Yılmaz, O.; Buytoz, S.(2001) Abrasive wear of Al₂O₃-Reinforced Aluminium-Based MMCs. *Compos. Sci. Technol.*, 61, 2381–2392.
- [102] Kok, M. (2005) Production and Mechanical Properties of Al₂O₃ Particle-Reinforced 2024 Aluminium Alloy Composites. *J. Mater. Process. Technol.*, 161, 381–387.
- [103] Suthar, J., and Patel, K. M. (2018). Processing issues, machining, and applications of aluminium metal matrix composites. *Mater. Manuf. Process.*, 33(5), 499–527. <https://doi.org/10.1080/10426914.2017.1401713>.
- [104] Standard Test Method for Dynamic Young's Modulus, Shear Modulus, and Poisson's Ratio by Impulse Excitation of Vibration. ASTM E1876, ASTM International, United States, 1–17.
- [105] Praveen, A. P., Rajamohan, V., and Mathew, A. T. (2019). Material and Mechanical Characterization of Multi-Functional Carbon Nanotube Reinforced Hybrid Composite Materials. *Experimental Techniques*, 43(3), 301–314. <https://doi.org/10.1007/s40799-019-00316-0>
- [106] Daramola, O. O., Olajide, J. L., Adediran, A. A., Adewuyi, B. O., Ayodele, T. T., Desai, D. A., & Sadiku, E. R. (2020). Multiscale analysis and experimental validation of the effective elastic modulus of epoxy-dioctahedral phyllosilicate clay composite. *Heliyon*, 6(6), e04008. doi:10.1016/j.heliyon.2020.e04008
- [107] Samantaray, A.K., Dasgupta, S.S., and Bhattacharyya, R. (2010) Bond Graph Modeling of an Internally Damped Nonideal Flexible Spinning Shaft. *J. Dyn. Sys., Meas., Control* 132(6): 061502

LIST OF PUBLICATIONS

International Journals

- I. A. Sharma, V. Rastogi, A. K. Agrawal. (2020) Microstructural, Dynamic and Residual Stress Analysis of Metal Matrix Composite Shafts. Transactions of the Indian Institute of Metals 73:12, pages 2995- 3005.(SCIE INDEXED, Springer, IF= 1.205)
- II. A. Sharma, V. Rastogi, A.K. Agrawal. (2020) Estimation and Experimental Validation of Mean-Field Homogenised Effective Properties of Composite. Experimental Techniques 3. (SCIE INDEXED, Springer, IF= 1.058)
- III. A. Sharma, V. Rastogi, and A. K. Agrawal, “Multi-Parametric Optimisation by Quantitative Assessment of Distribution Index and Area Fraction of Composite,” Practical Metallography, vol. 57, no. 9, pp. 588–613, Sep. 2020. SCIE INDEXED, Hanser Library, IF= 0.315)
- IV. A. Sharma, A.K. Agrawal, V. Rastogi, A. Gupta, “Multi-scale dynamic analysis of metal matrix composite shafts through morphological evaluations”, Proceedings of the Institution of Mechanical Engineers, Part E: Journal of Process Mechanical Engineering. September 2021. (SCIE INDEXED, Springer, IF= 1.61)

Paper presented in International Conference

- I. A. Sharma, V. Rastogi, and A. K. Agrawal, Overview on Dynamics of Metal Matrix Composite Rotors, 1st International Conference on New Frontiers in Engineering, Science & Technology

- II. A. Sharma, V. Rastogi, and A. K. Agrawal, “Micro mechanical modelling through morphological evaluation of long metal matrix composite shafts”, “ICTRDARIP-2020”